PARTICULATE MORPHOLOGY AND DEFORMATION CHARACTERISTICS IN MODULATION ASSISTED MACHINING

by

Indrani Biswas

A Dissertation

Submitted to the Faculty of Purdue University

In Partial Fulfillment of the Requirements for the degree of

Doctor of Philosophy

School of Materials Engineering

West Lafayette, Indiana

May 2021

THE PURDUE UNIVERSITY GRADUATE SCHOOL
STATEMENT OF COMMITTEE APPROVAL

Dr. Kevin Trumble, Chair
School of Materials Engineering

Dr. Srinivasan Chandrasekar
School of Industrial Engineering

Dr. Michael Titus
School of Materials Engineering

Dr. James Mann
Department of Mechanical Engineering,
University of West Florida

Approved by:
Dr. David Bahr

To my family

ACKNOWLEDGMENTS

I have been extremely fortunate to have received the support and guidance of many people during my time as a graduate student at Purdue. I sincerely appreciate the help and express gratitude to all. First and foremost, I would like to thank my advisor, Prof. Kevin Trumble, for making me a part of the group and providing guidance on experimental techniques, reviewing literature, and scientific writing. I am always inspired by his enthusiasm to teach and to learn something new each day. I would also like to express sincere gratitude to my collaborator, Prof. James Mann, for his continued support and encouragement. A humble acknowledgment goes out to all my committee members: Prof. Srinivasan Chandrasekar, Prof. Michael Titus, Prof. Mann, and Prof. Trumble for their insightful comments and feedback. I would like to acknowledge my funding source, NSF Foundation, division of materials research, and division of civil, mechanical, and manufacturing innovation, for providing the necessary aid over the course of five years. I thank all my professors at Purdue, especially, Prof. Paul Mort, Prof. Rodney Trice, Prof. Jeffrey Youngblood, Prof. Mike Titus, and Prof. Haiyan Wang, for engaging in interactions about experimental design and instrumental capabilities, and graciously allowing the use of their equipment for my experiments. I am also grateful to the current and ex MSE staff, Stacey, Rosemary, Vicki, Donna, Aury, Robyn, Cathy, and Lisa, for their unfailing and timely assistance to every administrative need. Lastly, I express sincere thanks to Jameson, Talukder, Shannon, Jenni, Darren, Tim, and Marc for providing training on the laboratory instruments and for making the labs a safe place to work.

A special thank you to my lab mates, Stiven and Mohammed, for our many enlightening discussions. Thank you to Debapriya, Mojib, Anirudh, and Zhongxia for your valuable contributions to my research.

A big thank you to all my amazing friends: Arindam, Srishti, Sanchari, Prabudhya, Sayantan da, Somrita di, Amartya, Satarupa di, Sreya, Sid bro, Aritra da, Debadrita, and many others, for the wonderful memories that we shared together. Far away from home, life would not have been the same without the potlucks and the meaningless conversations with you all. Special thanks to my friends for life, Swarnali, Prethula, Tuhin, Baneswar, Poulami, Sabarni, Aditi, Amritansh, and Rakesh for being there for me, even though we are miles apart. I consider myself lucky to have such a wonderful support system through my friends.

Lastly, I would like to thank my family, my mother (Maa), my father (Baba), and my brother (Dada). Your constant support and belief in me, kept me motivated throughout the journey and encouraged me to perform better. I am also grateful to Masi, my cousins, and other family members and friends who have supported me along the way.

Indrani Biswas, West Lafayette, April 2021

TABLE OF CONTENTS

LIST OF TABLES

LIST OF FIGURES

LIST OF SYMBOLS

d	Workpiece outer diameter
s_o	Feed per revolution in turning
DOC	Depth of cut
t	Time
v_o	Cutting velocity
α	Nominal tool rake angle
ζ	Tool flank angle
ϕ	Shear plane orientation angle
ψ	Direction of maximum elongation of grains
F_s, N_s	Force parallel and perpendicular to shear plane
F_p, F_q	Force in horizontal and vertical directions
u	specific cutting energy
γ	Shear strain
$\dot{\gamma}$	Shear strain rate
r	Cutting ratio
f_w	Rotational frequency
T	Time period of workpiece rotation
f_m	Modulation frequency
A	Amplitude of modulation
λ	Wavelength of modulation
ω	Angular velocity of modulation
φ	Phase difference between consecutive tool passes
h	Instantaneous uncut chip thickness
h_o, h_c	Undeformed and deformed chip thickness
w	Chip width
l_o, l_c	Undeformed and deformed chip length
$l_{cpredicted}$	Predicted deformed chip length
e_u	Rolling strain assuming uniaxial compression

e_p	Rolling strain assuming plane-strain compression
S_a	Arithmetic mean surface roughness
I	Intensity of diffracted x-rays
θ	Diffraction angle
H, L	Height and length of pillars in linear cutting
V	Workpiece velocity in linear cutting
u_a	Specific energy of powder production in atomization
H_m	Latent heat
T_m	Melting temperature
C_p	Specific heat capacity of the chip
V_{prod}	Volumetric particle production rate in MAM

ABBREVIATIONS

MAM	Modulation-assisted machining
CC	Continuous chip
OM	Optical microscopy
OD	Outer diameter
VHN	Vickers hardness number
DIC	Differential image correlation
PIV	Particle image velocimetry
PZT	Lead zirconate titanate
RPM	Rotations per minute
SEM	Scanning electrom microscopy
TEM	Transmission electrom microscopy
FIB	Focussed ion beam
XRD	X-ray diffraction
EDM	Electro-discharge machichining
MQL	Minimum quantity lubrication
CMOS	Complementary Metal Oxide Semiconductor

ABSTRACT

Studies of mechanics and deformation in metal cutting operations have been largely limited to steady-state processes assuming constant forces and shear strain of cutting. However, 'transient' or varying deformation conditions are frequently encountered in manufacturing processes, when one or more processing parameters vary during the progress of the cut. Such conditions impose a lower overall strain on the resulting chip and affect the cutting forces and energies. In this study, the transient deformation characteristics are studied through the analysis of chip attributes (hardness and shape change) in a periodic cutting technique, Modulation Assisted Machining (MAM). In MAM, a sinusoidal modulation is superimposed on the tool feed, resulting in periodic engagement between the tool and workpiece. Deformation is confined to a specific volume of material and is also transient due to varying local conditions, manifesting an inhomogeneous and lower shear strain compared to steady-state cutting. A wide variety of deformation conditions from near steady-state to completely transient was achieved through the control of modulation frequency, which determines the contact length in each cutting cycle. Particles produced at lower frequencies exhibit increased hardness, consistent with the deformation more approaching steady state. Micro-indentation tests performed on each particle tracked the local variations in hardness along the length of cut, which agreed well with the non-uniform shape change observed on the cross-section of the particles. Microstructural examination of the chips made with and without modulation helped further describe the different deformation modes acting under periodic and continuous cutting conditions. MAM is also a valuable technique for metal powder processing. Individual chip particles are produced during each modulation cycle with controllable shape and size, and composition identical to that of the workpiece. Advantages of the process include a significant reduction in the specific energy of production, zero compositional variance and a tight distribution of particle sizes compared to atomization. Implications of scaling up the process for large-scale production and the possible applications of the metal particles made with MAM are highlighted.

1. INTRODUCTION

Material removal is an integral step in the manufacturing and shaping of metal parts. Cutting processes are frequently utilized in both large commercial sectors like railway, automotive, and aerospace industries and in the production of small-scale components with ultra-fine precision for the consumer electronics sector [1]. There are numerous methods for material removal like turning, milling, boring, etc., each suitable for specific applications. They all involve a sharp cutting tool and a workpiece that is to be cut. Upon engaging with the workpiece, the cutting tool imparts a large plastic deformation in the form of shear onto the workpiece and displaces some amount of material ahead of the tool face. The deformed material forms a long and coiled *continuous chip* which eventually fractures and detaches from the main workpiece [2].

The formation of a continuous chip during machining maintains intimate contact between the freshly cut workpiece surface and the cutting tool. This makes the machining zone inaccessible to cutting fluids, limiting its flow only to the edges of the contact [3]. The severity and the long duration of the contact lead to elevated temperatures in the cutting field which affects the material microstructure and accelerates thermo-chemical wear in the tool reducing tool life [4]–[6]. Longer chips hinder smooth chip evacuation affecting the removal rates for deeper cuts [2]. High loads and large specific energies are often encountered in continuous cutting processes as a result of the concurrent large plastic deformation. Several modifications to the existing cutting processes have been done to reduce if not eliminate these problems. Chip-breaker grooves have been designed to break the continuous chip into pieces and achieve superior chip removal [7]. Cryogenic cooling or a combination of cryogenic flood-based cooling and MQL has shown improvements in enhancing the tool life [8]. A possible way to reduce the severity of the tool-chip contact and hence the material deformation during cutting is by imposing a controlled modulation onto the tool, thereby, periodically disrupting the tool-chip contact.

Modulation-assisted machining *(MAM)* is a modified turning process where a sinusoidal oscillation is superimposed on the feed direction of the machining process and the feed rate is modulated. For specific amplitude and frequency of modulation, cutting is disrupted by periodic engagement between the cutting tool and workpiece. Individual chip "particles" with controllable shapes and sizes are formed during each modulation cycle. Other vibration-assisted machining processes have been developed and implemented for cutting brittle metals or to achieve complex geometries [9], [10]. In these processes, intermittent tool engagement has been shown to greatly improve machinability [11], [12] and reduce tool wear [13]. However, the effect of the imposed modulation/vibration on material deformation during cutting is still unknown. In continuous cutting without modulation, the feed rate (undeformed chip thickness), tool rake angle, and material response are constant, resulting in a large shear strain, γ, typically around 1-10 [2], [14] and steady-state deformation conditions. This deformation is manifested in the shear strain which can be determined directly via the measured thickness of the deformed chip compared to the known undeformed chip thickness (process feed rate). However, under modulating conditions, the cutting parameters vary during the duration of the cut (i.e., along the length of tool-workpiece engagement) as shown in figure 1.1a. In addition to that, due to the very short duration of each modulation or cutting cycle, the deformation state cannot reach a steady-state resulting in "incipient chip formation" [15], [16] (figure 1.1b) and a lower and inhomogeneous strain in the chip volume. The nature or extent of this incipient deformation is governed by the time duration (equivalently length) over which the chip is formed. Thus, the deformation (strain and shape change) occurs in the transient or non-steady-state.

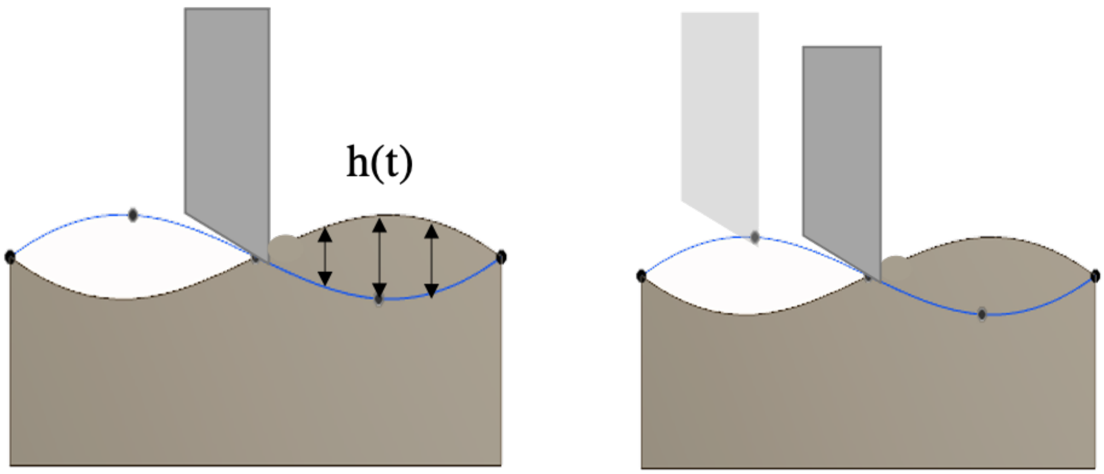

(a) (b)

Figure 1.1. Origin of inhomogeneous transient deformation in MAM (a) due to the changing chip thickness with time (b) due to frequent engagement and disengagement, which results in incipient chip formation.

The mechanics of metal cutting have been studied in detail with assumptions of steady-state conditions[2], however, this transient aspect of chip formation has not received adequate attention to date. A few studies have recognized and proven the presence of transient deformation in processes with incipient chip formation during the onset of cutting [17] and with frequent changes in parameters like undeformed thickness [18]. It would be of value to better understand, quantitatively, the transient nature of this plastic deformation process, especially in the context of inferring the role of process parameters, be it in similar transient-chip formation processes like wear or other manufacturing processes, based on analysis of particle and chip attributes. Machining chips carry the signature of the nature of the underlying material removal process and thus, an analysis of their physical, mechanical, microstructure, and chemical attributes can provide important insights into the phenomena and mechanisms that are operative in the removal process.

Problem Statement:

Prior studies have indicated that in MAM, the propensity of incipient chip formation is greater for higher modulation frequencies since the length of the cut is shorter [15], [16].

For lower frequencies or longer lengths of chips, the cutting force measured directly by dynamometry gradually increased with the length of the cut and became steady for most of the duration of the workpiece-tool engagement. For very short chips, however, after the onset of cutting, the force increased, reached a maximum value, and then dropped down to zero, indicating detachment with the workpiece. This suggests that while in low modulation frequencies, the deformation may reach a steady state analogous to continuous cutting, it does not for higher modulation frequencies. Overall, the energy dissipation for cutting with modulation was lower than that for continuous chip formation. The hypothesis is that these variations in cutting forces arise from the inherent difference in the deformation modes for cutting with and without modulation, which in turn affect the chip properties. The role of process parameters in determining the incipient behavior, and the corresponding consequence on the particle morphology (dimensions, cross-sectional shape, and surface roughness) is of key interest and emphasized in the thesis. The level and distribution of deformation in the chips are also characterized via direct microstructural observations and measurement of micro-hardness.

Interrupted cutting in MAM produces discrete chips or *particles* morphologically similar to metal powders. The size and shape of these particles can be precisely controlled by the alteration of process parameters like the frequency and amplitude of modulation, cutting speed, etc., and the deformation characteristics. Metal powders for engineering applications are required to meet stringent specifications for dimension, shape, composition and density [19], [20]. Commercial powder processing techniques like atomization often produce powders with variance in composition and density, and a large size distribution requiring subsequent classification steps to produce an acceptable feedstock [21]. As a result, a large volume of powders is rejected from each batch as oversize/undersize. This greatly decreases the process efficiency, thereby, increasing the specific energy of production. MAM particles are produced under discrete processing conditions making them essentially identical with composition and density matching that of the bulk workpiece. The process kinematics and the particle dimensions are correlated and compared with experimentally measured values. Morphological changes in particle cross-section are tracked as a function of the modulation and cutting parameters. Process metrics like surface quality, energy efficiency, and production rate are also reported.

The thesis characterizes the transient state deformation in MAM by examining the particle morphology, hardness and microstructure. By varying the frequency and amplitude of the oscillations, the time (and length) duration over which the deformation is imposed on a particle is varied in a controlled way. This enables a wide range of transient, large-strain deformation conditions, from very incipient to steady-state, to be realized in the particle. The deformation attributes of these particles, implications for MAM as a manufacturing process and possible applications for the MAM particles are discussed.

Structure of the thesis:

A brief introduction to the problem statement was provided in chapter 1. In chapter 2, a background on the steady-state orthogonal cutting mechanics and metal deformation during machining, is established. The optimum modulation conditions that lead to discrete chip formation are laid out. Previous observations of incipient deformation in orthogonal metal cutting, milling, and modulation-assisted machining are described. Chapter 3 elaborates on the cutting process set up and introduces the workpiece materials and the characterization tools used in the study. The operating procedure of the instruments and the sample preparation methods are also elucidated. In chapter 4, the various morphologies obtained from different materials at different processing conditions are presented and compared with the predicted particle morphology. Chapter 5 discusses the effect of incipient chip formation on chip deformation and microstructure. The limitations of the MAM system for studying chip shape change due to deformation, are presented and motivation was drawn for performing linear orthogonal cutting tests with a special specimen designed to interrupt cutting at periodic intervals. The experimental details of cutting with the linear slide and the results are included in chapter 6. In chapter 7, an application of MAM as a particle production technique is extended and the corresponding advantages and limitations are outlined.

2. LITERATURE REVIEW

A brief description of steady-state cutting mechanics is provided including expressions for cutting forces, strain and energy. The deformation modes prevalent in orthogonal machining are also described. Specific numerical relationships between process parameters are derived to achieve discrete chip formation and their physical basis is explained. The occurrence of transient and incipient deformation in modulated cutting systems and other cutting techniques like milling is acknowledged and the available literature in describing the phenomenon is discussed.

2.1 Orthogonal cutting mechanics

Most of the experiments done in the thesis are performed via turning. The turning configuration utilizes a rotating cylindrical workpiece and a single-point tool that engages with the workpiece from the side and removes material from the circumference parallel to the axis of rotation. The variables in the process are:

1. v_o, cutting speed, determined by the rotations per second, (f_w of the workpiece.
2. s_o, feed rate, given by the distance the tool moves along the cylinder axis during one rotation.
3. DOC, depth of cut, engagement of the tool-workpiece along the cylinder radius.

The depth of cut is usually greater than five times the feed giving rise to plane strain deformation conditions during machining. It is assumed that the chip flow is always perpendicular to the cutting direction leading to orthogonal cutting conditions. Analysis of a simple case of orthogonal cutting can reasonably approximate the applicable forces for most cutting operations and has been discussed here. Steady-state cutting is assumed to occur over a region of concentrated shear called the primary deformation zone (the blue region in figure 2.1b), often described as a single mathematical plane called the shear plane (shear plane model). The orthogonal cutting model is based on a few assumptions such as:

1. A perfectly sharp tool
2. The shear zone is a single plane

3. Cutting occurs under plane strain conditions; thus, there is no side flow of the chip
4. The undeformed chip thickness is constant
5. Stresses along the shear plane are constant

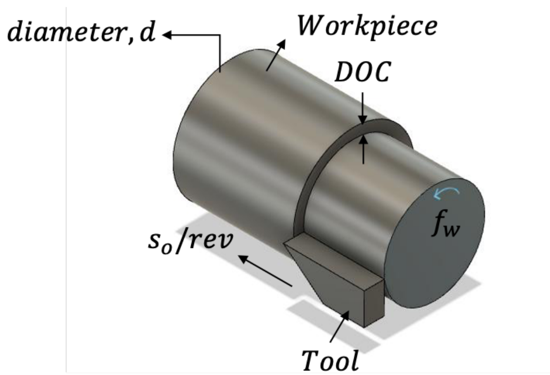

(a) turning configuration

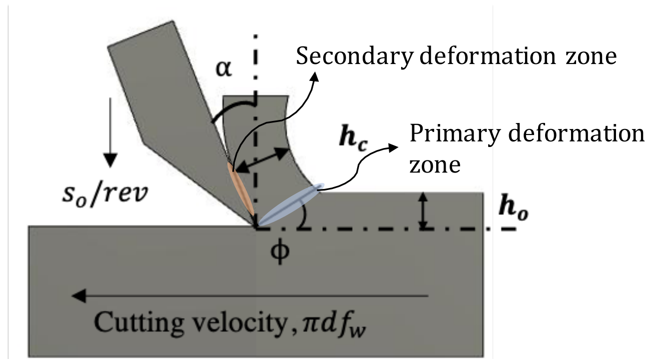

(b) orthogonal cutting configuration

Figure 2.1. Cutting configurations in (a) turning (b) turning represented in 2-D.

A sharp, wedge-shaped tool is brought into contact with the workpiece at a preset depth, h_o (corresponding to the feed rate, s_o in turning configuration), and width (w) (= DOC). The tool moves in a direction perpendicular to its cutting edge, removing the material as a chip. The plane of the chip that slides against the tool face is called the rake face. The principal parameters of the process are shown in figure 2.1: α denotes the tool rake angle, ϕ denotes the shear plane orientation, h_o and h_c are the undeformed and deformed chip thicknesses respectively, r is the chip thickness ratio h_c/h_o, w is the chip width, and v_o = circumferential velocity of the workpiece = $\pi d f_w$, is the machining speed (deformation rate). Large plastic strains in the order of 1-10 are typically imposed in the primary deformation zone during the material removal process [2], [22]. A secondary deformation zone of large deformation prevails over a small region adjoining the tool-chip contact along the tool rake face (the orange region in figure 2.1b); the energy dissipation associated with this secondary deformation is commonly identified with the frictional dissipation occurring at this interface.

The two primary forces acting on the workpiece are:

1. The force between the tool rake face and the chip, R

2. The force between the workpiece and the chip, R'

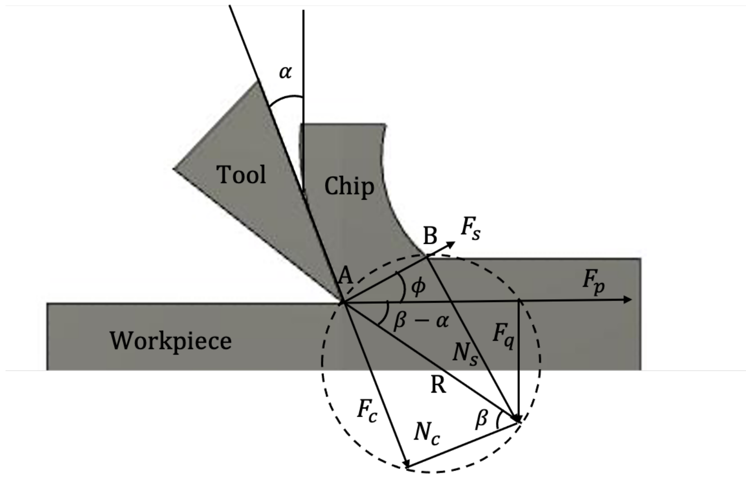

Figure 2.2. Schematic of cutting forces. Adapted from [2].

The forces are further resolved into components along and perpendicular to the shear plane as, F_s and N_s and similarly, parallel and orthogonal to the tool face, as F_c and N_c. The shear stress on the shear plane can thus, be determined as,

$$\tau = F_s/A_s \tag{2.1}$$

Where, A_s is the area of the shear plane given by,

$$A_s = \frac{wh_o}{\sin\,\phi} \tag{2.2}$$

Metal cutting does not involve a change in density, thus, the volume of material removed from the workpiece is equal to the volume of chip produced, i.e.,

$$h_o w_o l_o = h_c w_c l_c \tag{2.3}$$

For plane strain conditions, the width of the chip remains unchanged, thus,

$$\frac{h_c}{h_o} = \frac{l_o}{l_c} \tag{2.4}$$

This ratio is defined as the cutting ratio, r, and can be expressed in terms of the cutting geometry as,

$$r = \frac{AB\ \cos(\phi - \alpha)}{AB\ \sin\ \phi} \tag{2.5}$$

The shear strain in the configuration is given by,

$$\gamma = \tan(\phi - \alpha) + cot\,\alpha \tag{2.6}$$

Reducing the above equation, it can be shown that,

$$\gamma = \frac{\cos\ \alpha}{\sin\ \phi\ \cos(\phi - \alpha)} \tag{2.7}$$

For a zero degree rake tool, $\alpha = 0$, thus,

$$r = \cot\ \phi \tag{2.8}$$

Equation 2.1 can also be written as,

$$\gamma = \frac{\sin^2\ \phi + \cos^2\ \phi}{\sin\ \phi\ \cos\ \phi} = \frac{\sin^2\ \phi}{\sin\ \phi\ \cos\ \phi} + \frac{\cos^2\ \phi}{\sin\ \phi\ \cos\ \phi} = \frac{\sin\ \phi}{\cos\ \phi} + \frac{\cos\ \phi}{\sin\ \phi}$$

Therefore,

$$\gamma = \tan\ \phi + \cot\ \phi = r + 1/r \tag{2.9}$$

The forces R and R' can also be resolved in the vertical and horizontal directions to give F_q and F_p, from which, the energy of cutting per unit time can be calculated as,

$$U = F_p V_o, \tag{2.10}$$

where V_o is the tool velocity. The energy per unit volume of material cut is given by,

$$u = \frac{U}{V_o w h_o} = \frac{F_p}{w h_o} \tag{2.11}$$

The quantity, specific energy of cutting is a measure of the cutting resistance of a material and is thus helpful for describing the machinability. The specific energy varies slightly with the rake angle, (1% increase per decrease in the rake angle) but significantly with the undeformed chip thickness,

$$U \propto \frac{1}{h_o^{0.2}} \tag{2.12}$$

The consequences of the specific energy variation with these process parameters play an essential role in periodic cutting systems like MAM, where, the undeformed thickness and the rake angle change during cutting, and will be discussed later in the thesis.

2.2 Flow line orientation and secondary shear zone

There have been numerous studies on microstructures of a partially formed chip to examine the material flow during cutting, that have led to a few observations:

1. Flow lines are formed on the chip that indicates shear as the primary deformation mechanism.
2. There is no material flow perpendicular to the chip flow direction.
3. A line separates the deformed and the undeformed regions, i.e., shear occurs across a very narrow region or essentially a plane.
4. The orientation of the flow lines is different from the shear plane orientation.
5. The chip maintains intimate contact with the tool and slides against it while flowing-secondary deformation.

A general relationship was given by Townend, [23] that estimates the difference in the shear plane's orientation (ϕ) and the direction of maximum elongation of the grains or the direction of flow lines (ψ), as defined in figure 2.3.

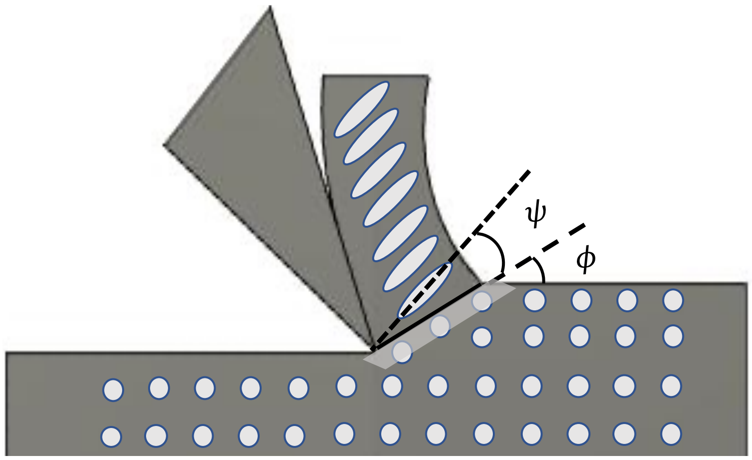

Figure 2.3. Schematic showing the shear plane orientation, ϕ and the direction of maximum elongation of the grains, ψ. The primary deformation zone is shaded to show the change in orientation of the grains. Adapted from [24].

$$2 \cot 2\psi = \cot \phi + \tan (\phi - \alpha) \tag{2.13}$$

However, experimentally it has been shown that this equation over-estimates the value of ψ. This is due to the presence of secondary shear. When the frictional stress at the tool-chip interface is higher than the shear flow stress of the chip material, a secondary flow occurs within the chip volume adjacent to the tool rake face. This causes the flow lines to re-orient along the shear plane as the chip flows up against the tool face.

2.3 Modulation-Assisted Machining

Modulation assisted machining can be realized in a few different ways; by imposing modulation in the direction of the cutting velocity, known as velocity-modulation (figure 2.4), or by imposing it in the direction of undeformed chip thickness, known as feed-modulation, or, with a combination of both [25].

2.3.1 Velocity-modulation

Plane-strain machining with sinusoidal velocity-modulation is shown in the left of figure 2.4. The cutting speed is varied during each modulation cycle while the undeformed chip thickness is kept constant. When the modulation velocity exceeds the mean (steady) cutting velocity, the instantaneous relative velocity of the tool with respect to the workpiece is reversed, and the tool-chip contact is disrupted. Thus, cutting is interrupted when, $\omega A > v_o$, where ω is the angular modulation frequency and 2A is the peak-to-peak amplitude and is shown in figure 2.4. Furthermore, due to the periodic disruption, there is a significant improvement in the fluid penetration in the tool-chip contact region. This has been shown to significantly reduce the friction relative to conventional machining and lower the cutting forces [25], [26].

But this modulation approach, the disruption condition of $\omega A > v_o$ is difficult to achieve in practice. It requires the use of ultrasonic frequencies and very low machining speeds (< 0.5 m/s), which are difficult to impose in processes such as drilling and boring due to system constraints. It also does not break the continuous chip into discrete chips which often leads to problems similar to those in conventional cutting stated in chapter 1.

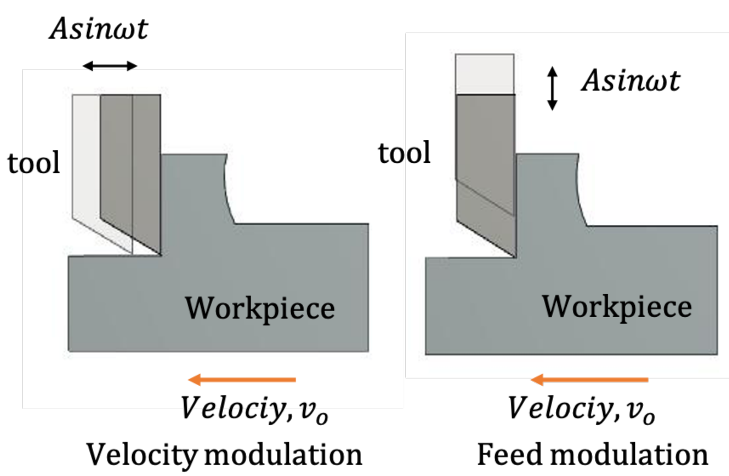

Figure 2.4. Types of modulation-assisted machining. Adapted from [15].

2.3.2 Feed-modulation (MAM)

A low-frequency, feed-modulation (figure 2.4) provides discrete chip formation and the tool-chip contact disruption can be realized at conventional machining speeds ($v_o > 0.5m/s$). A sinusoidal form of modulation, $A\sin(2\pi f_m t)$, is superimposed parallel to tool feed rate, (s_o), such that instantaneous tool feed varies with time (t) [27],

$$s(t) = s_o + A\sin\,2\pi f_m t \tag{2.14}$$

The key parameters of MAM are the modulation frequency (f_m) and the amplitude (A). In turning, a workpiece of diameter, d, rotates at a frequency, f_w, and material is removed by feeding the tool at a rate of s_o per revolution in a direction parallel to the axis of rotation (figure 2.1a). Here, s_o corresponds to the undeformed chip thickness, h_o. If T is the time period of rotation of workpiece ($T = 1/f_w$), the undeformed chip thickness at a particular point on the cylinder surface will be given by the difference in tool feed at times t and t+T, i.e.,

$$h(t) = s(t+T) - s(t) \tag{2.15}$$

When the frequency and amplitude of modulation are such that h(t) becomes less than or equal to zero during each cycle of modulation, the tool is no longer in continuous contact with the workpiece resulting in the formation of 'discrete chips'. The number of chips or particles produced is equal to the number of complete modulation cycles, which is f_m per second or f_m/f_w per rotation of the workpiece (corresponding to one pass of the tool). This type of modulation machining henceforth referred to as MAM, is the configuration of interest for this thesis.

In a turning configuration the workpiece rotation results in a cutting velocity of $\pi d f_m$. During each complete rotation of the workpiece, the tool can be visualized to move linearly from x = 0 to x = $\pi \cdot d$ with the subsequent pass beginning again at x = 0. If a sinusoidal feed-modulation is now superimposed, the position of the tool during the n^{th} cycle can be described as:

$$y_n(x) = (n-1)s_o + (h_o x)/\pi d + A \sin(2\pi x/\lambda + (n-1)\varphi) \tag{2.16}$$

where,λ = wavelength of modulation cycle = $\pi d f_w / f_m$ and φ = phase angle between consecutive passes ($\pi[f_m/f_w - [f_m/f_w]]$). Simulated tool paths are shown in figure 2.5.

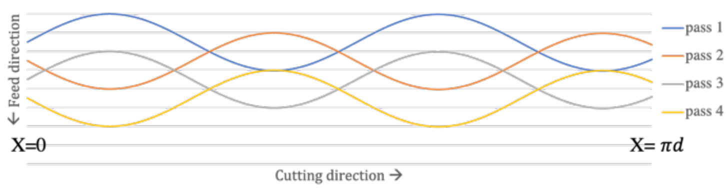

Figure 2.5. Tool path simulation showing that the consecutive passes are out-of-phase with each other.

The cutting process can be visualized in 2-D by unfolding the cylindrical workpiece onto a plane surface (figure 2.6). The shape of the workpiece material above the blue line (n^{th} tool pass) defines the geometry of the undeformed chip. Note that the removed chip has a different shape owing to the deformation of the process. The figure also shows the change in the rake angle from the start till the end of the cutting cycle. This also imparts a variable strain along the length of the cut, and is, therefore, another source of transient deformation in MAM.

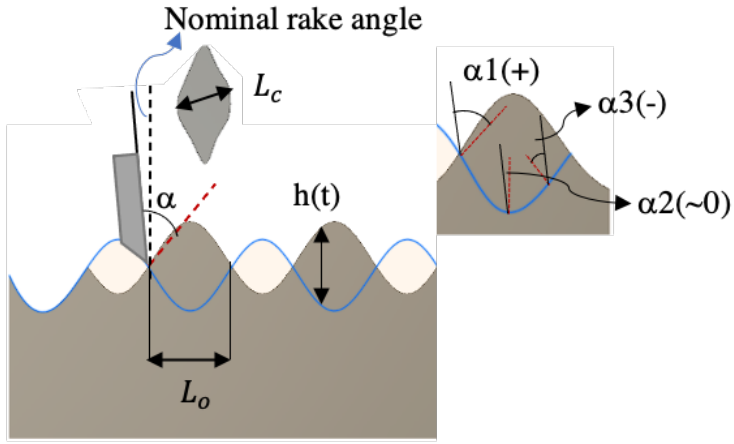

Figure 2.6. Schematic of MAM process showing feed modulation of the tool, the uncut and deformed chip shape and the variation of rake angle along the length of cut.

The undeformed chip thickness can be expressed as,

$$h(x) = y_n(x) - max(y_{\mathrm{i}}(x)), \qquad where, \mathrm{i} = 1, 2, 3...n - 1 \tag{2.17}$$

which takes into account the cumulative effect of the cutting paths before the n^{th} pass in determining the surface profile of the workpiece. It may be shown by incorporating equations 2.16 and 2.14 that A/s_0 is a function of f_m/f_w and is plotted in the figure below [28].

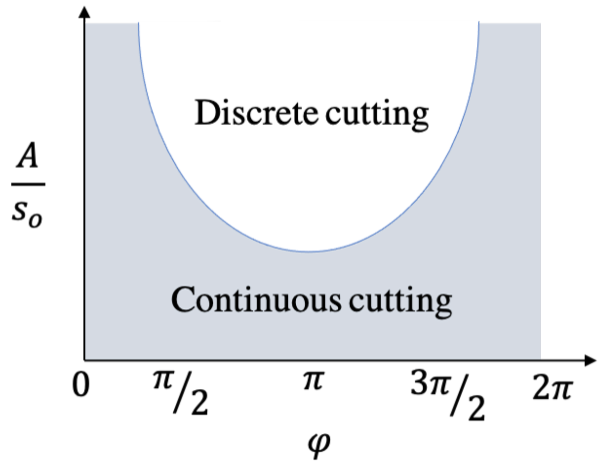

(a) A/h_0 vs. φ

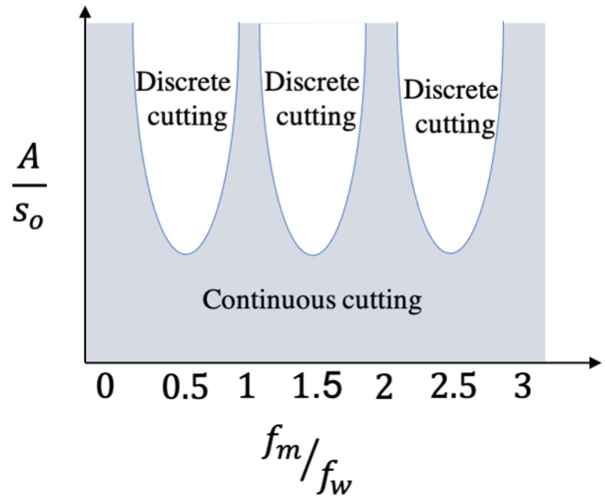

(b) A/h_0 vs. f_m/f_m

Figure 2.7. Cutting regimes as defined by the process parameters. Adapted from [28].

The U-shaped curve shown in the figure 2.7 forms the boundary between two cutting regimes: continuous cutting and discrete cutting (i.e., h(t) < 0). For modulation conditions outside the U-curve (shaded area), the tool is engaged with the workpiece at all times and the cutting is continuous, despite the superimposed oscillation on the tool. For conditions inside the curve, discrete chip formation is achieved with the disruption of the tool-chip contact in each cycle of modulation. The boundary values represent the minimum modulation amplitude required to cause discontinuous cutting (h(t) = 0) at the corresponding values of f_m/f_w. The global minimum or the smallest value of A for discrete chip formation is given by: $2A = s_o$ and occurs when $\varphi = \boldsymbol{\pi}$; this value of φ corresponds to:

$$f_m/f_w = (2n+1)/2 \qquad where, n = 1, 2, 3, 4, ... \tag{2.18}$$

Thus, the modulation conditions, $f_m/f_w = (2n+1)/2$ and $2A = s_o$ are both required for perfect or optimal modulation. At the asymptotic ends of the U-curves, i.e., at $f_m/f_w = n$, consecutive cutting passes are parallel or in-phase (0° phase difference), therefore, discrete chip formation cannot be realized regardless of the magnitude of A. Instead, a wavy continuous chip of constant thickness will be formed (figure 2.8b) at all cutting conditions.

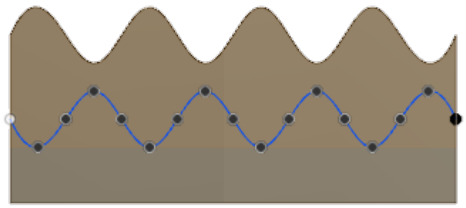

(a) $A < S_o/2$ (b) $f_m/f_m = \text{n}$

Figure 2.8. Conditions showing continuous chip formation even with imposed modulation when (a) the amplitude is low (b) consecutive passes are in phase with each other.

2.3.3 Particle size calculation

Particles of diverse shapes ranging from equiaxed to elongated fiber-like morphologies can be produced by systematic control of the process parameters in MAM [27]. Equiaxed particles are produced when the modulation wavelength, feed and the DOC are similar in magnitude; the platelets can be produced by cutting with a very small feed, and; fibers are produced by setting the DOC to be much larger than the feed and the modulation wavelength (typically > 5 times).

The undeformed particle dimensions are defined in a way that, particle or chip length, l_o, is in the cutting direction, width, w, is the depth of cut and thickness, h(t), is in the feed direction as indicated in figure 2.9. The length of the particle is given by the circumference of the tube divided by twice the number of cuts (f_m/f_w). The factor two comes from the fact that cutting occurs only during half of the duration of the modulation cycle [27].

$$l_o = \frac{1}{2}\frac{\pi d f_w}{f_m} \tag{2.19}$$

The chip produced after cutting has an average thickness, h_c, greater than the undeformed chip thickness, h_o, due to the deformation of the chip during cutting [12]. In our study, the width of the particles was set to be much larger than the length and the thickness, essentially creating plane strain conditions and producing particles in the fiber morphology. This eliminated the dependency of the chip width on the deformation conditions, leaving us with chip length and thickness as the two variables to study. For volume constancy, an increase in chip thickness is complemented by a decrease in the length of the chip from an undeformed value of l_o to l_c. The cutting ratio, r, is a measure of this thickening and is a function of the deformation characteristics of the material. Incorporating the value of the cutting ratio in equation 2, the deformed particle thickness can be calculated as, $h_c = f(feedrate) \cdot r$.

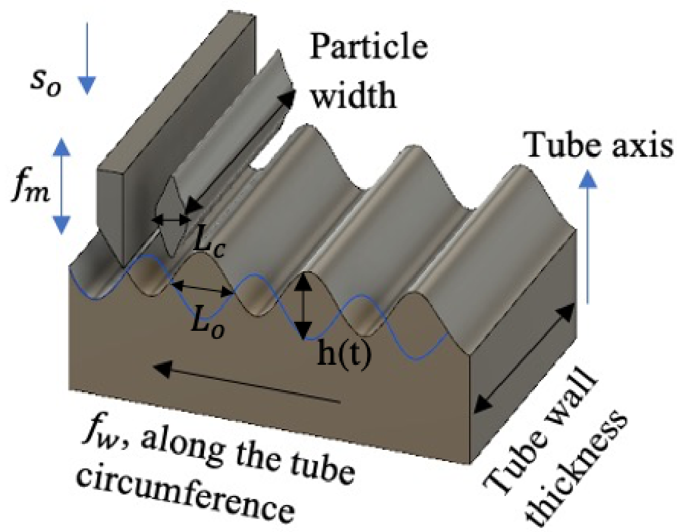

Figure 2.9. Schematic of fiber making in MAM showing the definition of the dimensions.

2.3.4 Strain inhomogeneity

In continuous cutting, the tool engages at a fixed undeformed thickness into the workpiece at a constant rake angle. In MAM, both the undeformed thickness and the rake angle changes along the tool path from the start to the end of each cutting cycle [29]. The rake angle changes from positive to negative within each modulation cycle as shown in figure 2.6. This imparts a variable strain into the material [14]. The cutting ratio being a function of the amount of strain should also change along the length of cut. This can lead to uneven thickening of the chip due to deformation. Prior studies also indicate that in MAM due to periodic engagement of the tool and the workpiece, during the start of each cutting cycle, the chip formation is in an incipient state. It was shown that during this state of deformation, the energy of cutting is lower, cutting forces are lower and consequently, a lower strain is imparted onto the material. Both these factors, the varying rake angle, and the evolution of the cutting process from transient to steady-state cause non-uniform strain in the chip during cutting.

2.3.5 Previous research work

The specific energy associated with chip formation was estimated by Yeung [15] from direct measurements of cutting forces and tool displacement. These measurements showed that the energy of cutting in MAM is 40-70 % lower than in continuous cutting under similar parameters like nominal rake angle, RPM, etc. A chip geometric parameter, $R = l_c/h_c$, was defined for MAM chips, to quantify the degree of transient behavior and predict the cutting forces/energies. The reduction in energy was attributed to the reduced levels of deformation during chip formation, an observation that was based on the lower forces measured during modulated cutting.

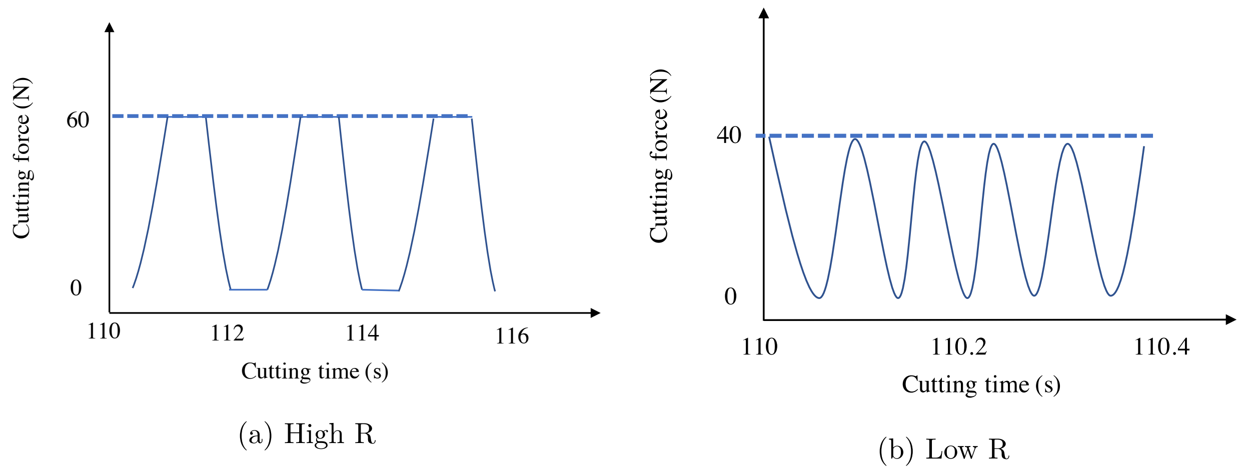

Figure 2.10. Measured cutting forces plotted against the time of cutting for (a) MAM with large R, showing increasing cutting forces, followed by a region of nearly steady-state and a drop indicating tool detachment (b) MAM for small R, showing that the forces do not reach a steady-state during a single cutting period [15].

Cutting forces measured by [15] are plotted schematically, against the time of cutting in figure 2.10. It was observed that for continuous cutting, the forces were stable at around 30 N. For cutting with MAM at a lower frequency of 0.5 Hz and feed rate of 15 $\mu m/rev$ that corresponded to R= 3738.4, the forces initially increased during the start of the cut, was nearly steady for the duration of tool-workpiece engagement and dropped at the end of the modulation cycle indicating the retrieval of the tool. For very small cycle times, i.e., cutting with a small R of 15.5 (f_m = 120.5 Hz), the forces increased and decreased alternatively, with no regions of steady behavior. Thus, at frequencies greater than 100 Hz, MAM chips are machined entirely under the incipient state.

Inferences of lower deformation level in MAM compared to continuous cutting were drawn from the prediction of shear strain in the chip using the Finite Element Method (FEM) and measurements of the deformation field and material flow using high-speed imaging of the primary deformation zone. Preliminary measurement of strain in chips formed with MAM was also performed by Mann [28] through measurement of uncut chip length and the deformed chip length using equation 2.1. It was found that the strain decreased with increasing modulation frequency, in agreement with the decreasing cutting energy for smaller R values, as observed by Yeung [15].

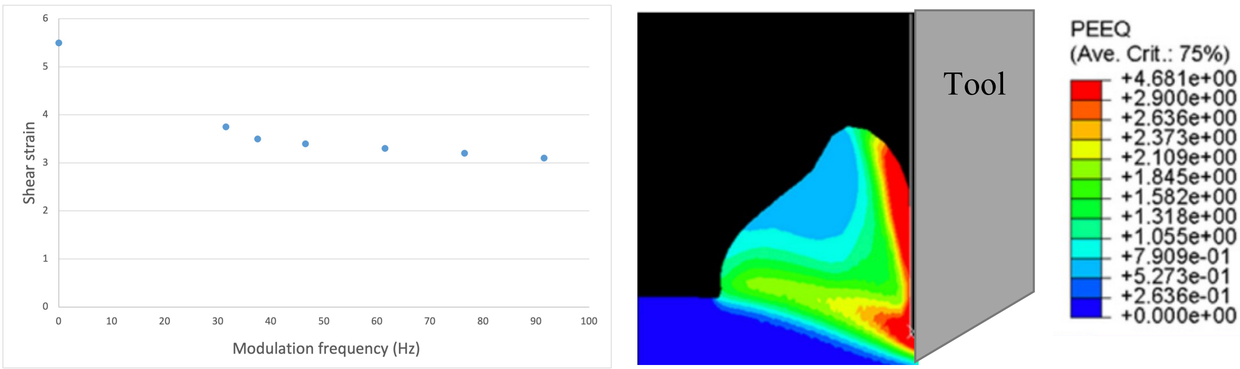

(a) (b)

Figure 2.11. (a) Variation of strain in Al 6061 chips, measured from the change in chip dimensions showing a decrease with increasing modulation frequency (b) Finite element simulation of strain in a chip produced at $f_m = 5$ Hz showing the difference in strain across the chip volume [adapted from [25], [28]].

Although these observations are strong predictors of the characteristics of chips machined under incipient conditions, the effect of such a unique deformation state on the microstructure and mechanical properties of chips has received little attention to date. A larger span of cutting frequencies has been implemented in the current study and the corresponding changes in chip characteristics have been mapped to connect the previously observed energies and forces in MAM to the chip mechanical properties.

2.4 Transient deformation observed in other cutting processes

Studies of transient deformation at the beginning of metal cutting have shown a steady increase in cutting forces with an increasing length of cut. A experiment was performed by Rosa et. al. [17] to measure cutting forces during the initial stages of orthogonal cutting in 99.9% pure lead with a 10° rake, cutting speed of 0.05 m/min and $h_o = 0.5$ mm.

Four zones were identified by the authors with distinct deformation modes. An increasing cutting force was observed during zones 1-3. During zone 1, the deformation was predicted to be similar to indentation. In Zone 2, initiation and propagation of a crack caused a small volume of material to be detached from the workpiece as a chip. In zone 3, the chip continued to separate from the workpiece and displayed severe bending away from the tool face, while the tool pushed forward into the material. In zone 4, the critical length of the chip was formed after which bending was no longer feasible (required greater energy than sustaining friction at the tool-chip interface) and shear was established as the primary deformation mechanism. The force saturated at around 850 N indicating the beginning of steady-state chip formation. Such increases in cutting force with the length of cut have also been observed in orthogonal cutting of brass [30]. This suggests that for interrupted cutting techniques, where the tool cuts a material for short intervals and therefore over very small lengths, cutting forces are lower than that for steady-state continuous processes and consequently, the deformation strain cannot be estimated from the mechanics of machining derived assuming steady-state shear.

Transient conditions are also realized when there is a sudden change in process parameters, such as the undeformed chip width, cutting directions, etc. Cutting forces for several such conditions were modeled and experimentally measured by Yun [18] for the flat end milling process in Aluminum 2014-T6. Figures 2.12a and 2.12b show schematics of two cases, first, where the tool engages and disengages with the workpiece material, and second, where the depth of cut/uncut chip width increases step-wise during the progress of the cut. The corresponding force measurements for both these cases are included in figures 2.12c and 2.12d.

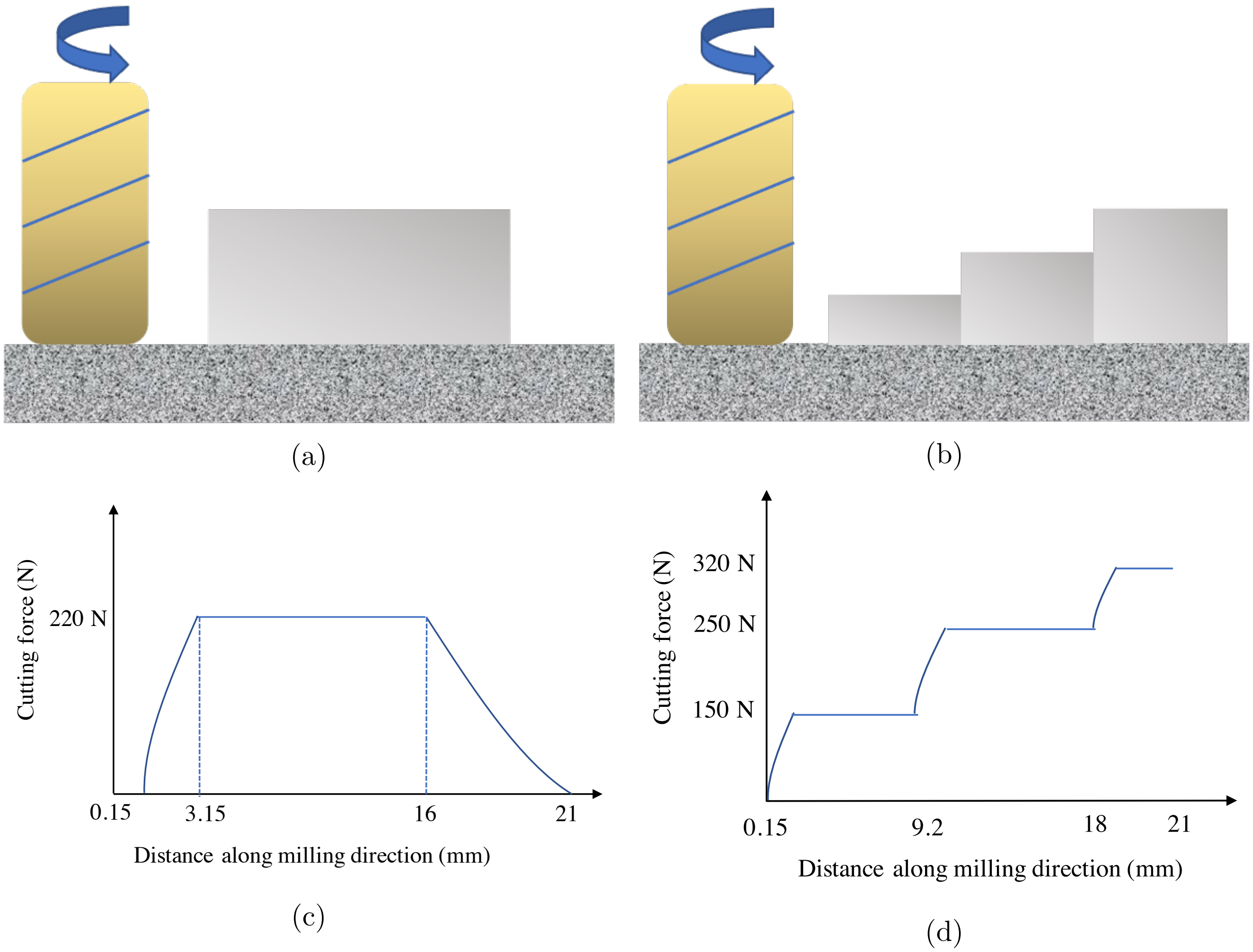

Figure 2.12. Simulating transient cutting conditions in milling, through a change in the cutter path when, (a) the tool engage and disengage with the workpiece (b) there is change in the undeformed chip thickness with time, (c) and (d) showing the corresponding change (increase) in cutting forces during the transient period before attaining the steady value. Adapted from [18].

The cutting forces undergo a gradual increase over a length of 1-2 mm after the tool engaged with the workpiece. Such increases have also been observed by Li et. al. for milling in Al 6061 [31]. A transition in cutting forces is also observed between each step of increasing workpiece depth, as shown in figure 2.12d. The changing uncut chip thickness in MAM is similar to the changing width in the above experiment, with very small changes in step size. Thus, for a process like MAM where there is periodic disengagement of the tool and the workpiece, and continuously changing parameters, cutting occurs under transient mode for the entire duration. The cutting forces are expected to be continuously varying during the cutting period, along with the imposed strain in the chip. In this study, various transients states will be imposed through the control of MAM process parameters, and the corresponding chip attributes will be characterized.

3. MATERIALS AND METHODS

The chapter includes the methodology of setting up the lathe and the modulation device to perform turning with superimposed modulation. The workpiece materials are introduced and operating conditions for the characterization tools implemented are mentioned. The sample preparation techniques for hardness and microstructure evaluation of the machined chips are also described.

3.1 Cutting process description

Modulation-assisted machining was performed by modifying the simple process of cylindrical turning. The machine used was a three-axis Miyano BNC-42 lathe. A cylindrical workpiece was clamped with a 5C collet chuck and was rotated a set RPM (rotational frequency). A tool turret was mounted on the alternate position from the workpiece; see figure 3.1a. Sinusoidal modulation was imposed on the tool along the feed direction (Z-direction in figure 3.1c), via a detachable piezo-actuator based device fitted on the tool holder. The device functions by controlling the movement of a PZT-based piezo stack [32]. The PZT discs are cased together with a ball-spline bearing to eliminate any out-of-plane motion through the movement of the bearings and produce a linear motion on the tool. The modulation device was controlled via an external power amplifier and waveform generator. The frequency and amplitude of the voltage signal provided to the piezo-device, in turn, regulated the tool oscillation. For most of the experiments, the peak-to-peak amplitude of modulation was set at 30 V with a 15 V offset, that corresponded to a peak-to-peak amplitude of 15 µm in tool movement. The modulation frequency was in the range of 50-1000 Hz.

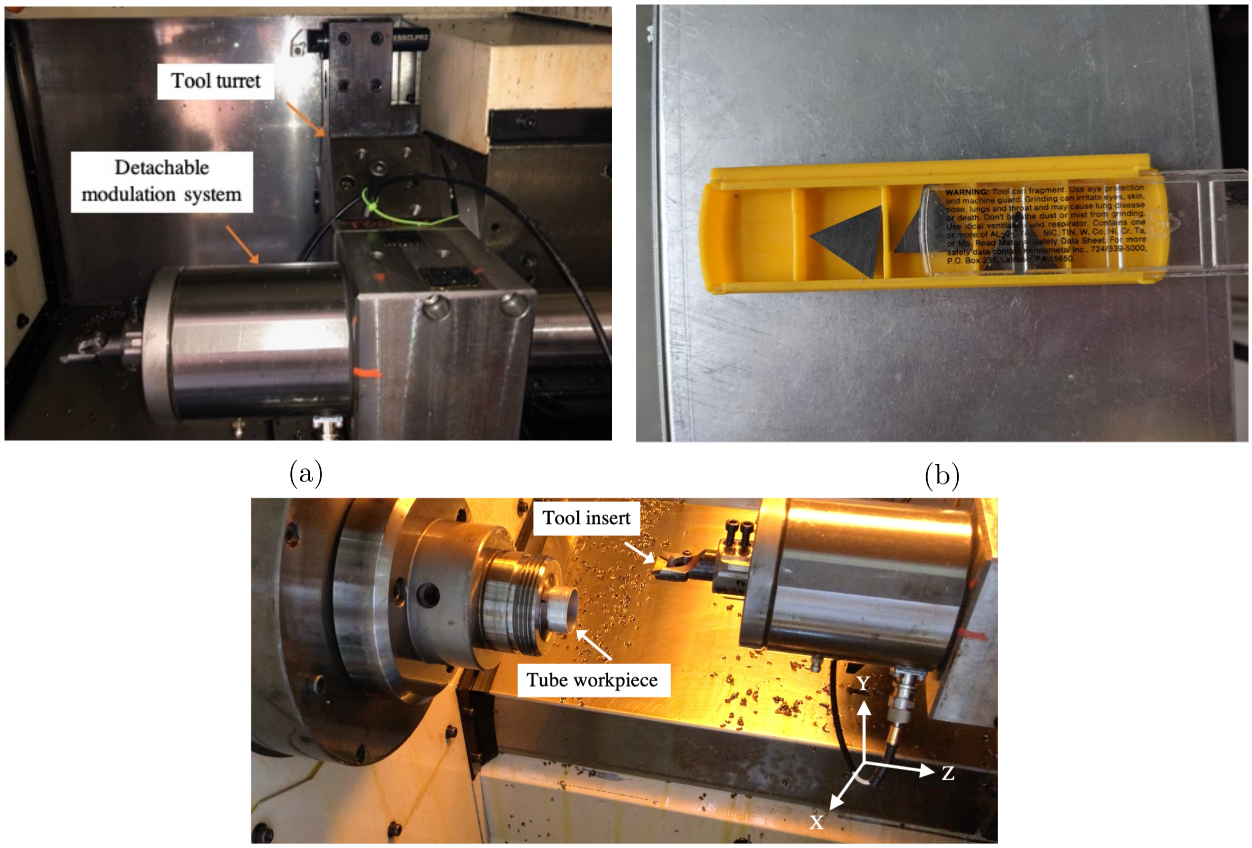

(a) (b) (c)

Figure 3.1. Showing (a) turret with the detachable modulation system fixed to one of the six tool holders (b) Kennametal cutting tool inserts (c) the cutting configuration showing the coordinate system used, the workpiece and the tool insert.

A replaceable tool insert (figure 3.1b) was fitted in the tool holder which formed the cutting edge that would engage with the workpiece material. The experiments were performed with triangular carbide tool inserts with 60° tool flank or clearance angle, ζ (Kennametal K68 grade). Two inserts, TPG 320.5 and TPG 320 were used, with tip radii of 200 μm and 100 μm respectively. The cutting edge of both the inserts produced a nominal rake angle of 0°. The workpiece rotational speeds used were in the range of 40 RPM to 120 RPM, with the majority of the experiments being performed at 120 RPM, or, a rotational frequency of 2 Hz. Therefore, to satisfy the discrete chip formation conditions, $f_m/f_w = \frac{2n+1}{2}$, or, $f_m = (2n+1)$, the modulation frequency was always set at an odd number. The feed rate was set at 5 μm per rotation of the workpiece. Isopropyl alcohol was chosen as the cutting fluid for Al 6061-T6, Ti-6-4 and copper, while, for Inconel 718, Mobil provided better lubrication and produced discrete chips.

Cutting from a solid cylinder creates a "hook" at the end of the fibers corresponding to the finite tool nose radius. The size of the hook is a direct function of the radius as illustrated in figures 3.2a and 3.2b. Note that the hook is more prominent for narrower fibers, or when the radius of the hook is in the same range as the fiber width. It is nearly absent for wider fibers made with TPG 320 insert, which has a smaller tool nose radius. Formation of the hook can be avoided by the use of a hollow cylinder or tube and setting the depth of cut to be larger than the tube wall thickness such that the tool nose is positioned past the tube wall and the workpiece only engages with the edge of the insert. All the data presented henceforth will show fibers that were machined from hollow tubes.

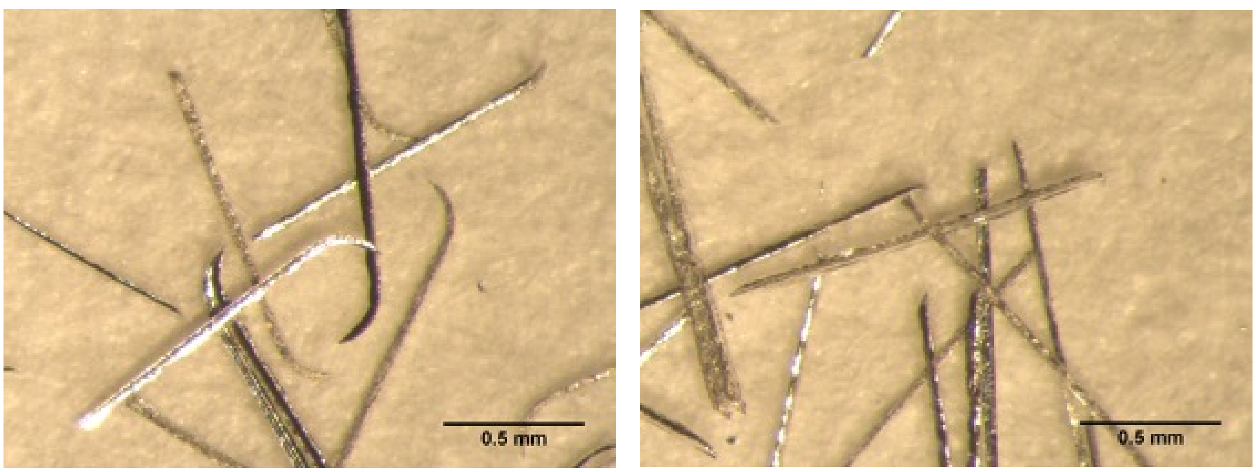

(a) Tool rip radius= 200 μm

(b) Tool rip radius=100 μm

Figure 3.2. Fibers cut using modulation from a solid cylinder showing the hook formation on the ends. The degree of curvature depends on the tool nose radius.

3.2 Experimental MAM system response

The dimensions and shape of the particles produced in MAM depend on the physical tool path inside the workpiece. Thus, to control the particle morphology effectively, it was important to measure the tool oscillation displacement with the modulation device inputs (frequency and voltage of the signal). The displacement was measured using a capacitive proximity sensor (Capacitec HPC 75-13090), calibrated at 0.02 mm/V. The probe was clamped in a 5C collet and the tool oscillation was activated. The end of the sensor and the face of the tool acted as the two plates of a capacitor. The to and fro motion of the tool resulted in a periodically varying distance between the capacitive plates which resulted in a varying capacitance and thus, a varying voltage signal. This signal was acquired at a rate of 5000 samples/sec (time step of 0.002 s) through a multi-function i/o device (National Instruments, NI USB-6259) and the LabVIEW platform on a PC.

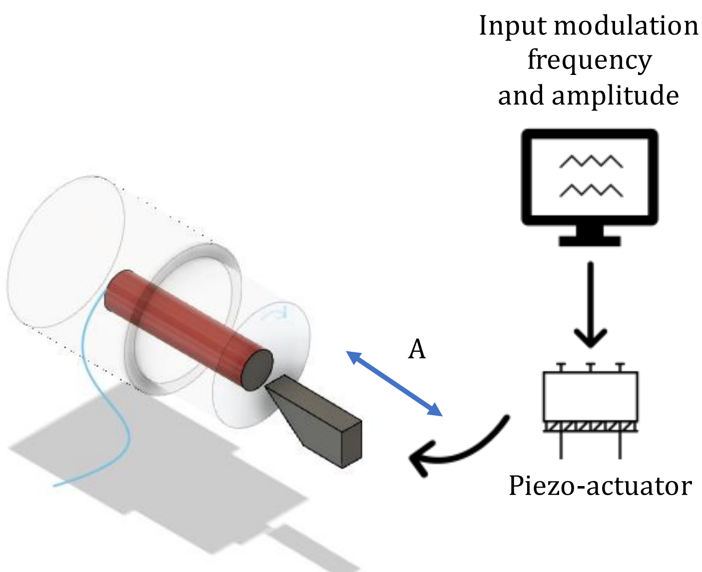

Figure 3.3. Schematic showing the process of tool feed calibration. A capacitive sensor is mounted on the workpiece holder. The varying voltage signal generated due to the oscillation on the tool is measured with a LabVIEW-based data acquisition system.

The individual voltage points traced the shape of a sin curve congruous to the sinusoidal motion of the tool. The average amplitude for each voltage, frequency combination was obtained through graphical analysis and is plotted in figure 3.4. Tool displacement in the feed direction is directly related to the input voltage, as shown by the relatively linear response for voltages below 70 V and frequencies lower than 400 Hz. However, at high voltages/high frequencies, the power amplifier has a roll-off response. This is manifested as a decay in the tool oscillation amplitude for a specific input voltage as the frequency is increased. The operational limits of the lab-based modulation system could be drawn and the physical motion of the tool could be predicted against the presented frequency and amplitude in the MAM device.

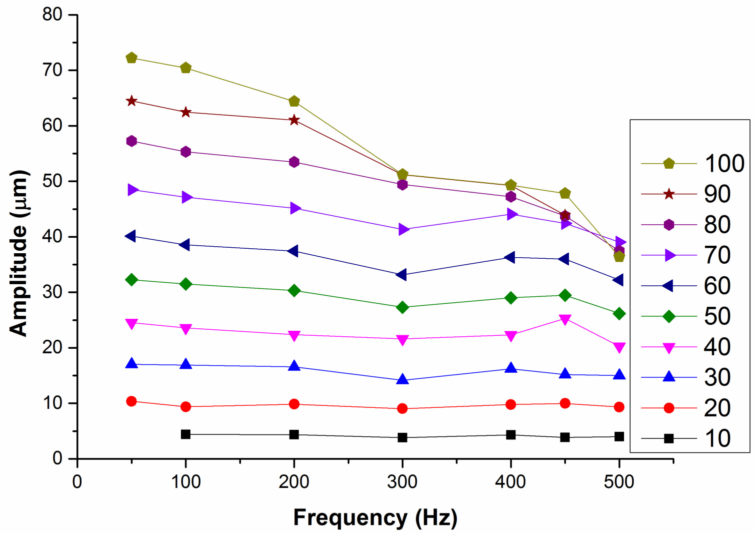

Figure 3.4. Tool oscillation amplitude (μm) obtained for specific voltage (Volts) inputs (labeled in box).

3.3 Workpiece materials

A primary aim of the project was to understand the effect of transient deformation modes on the fiber characteristics. Since the response to deformation strongly depends on the type of material, chip formation was studied for four alloys that are known to undergo distinct deformation mechanisms during conventional cutting techniques. Alloys were chosen with varying hardness and stacking fault energies to obtain particle morphologies for both soft/hard metals, and for materials exhibiting uniform/localized deformation. The feasibility of producing powders from a wide range of alloys with different machinability was also demonstrated from a manufacturing perspective.

3.3.1 Aluminum 6061-T6

Aluminum 6061-T6 was chosen as the model alloy for most of the experiments owing to its high machinability. Al 6061 belongs to the aluminum-magnesium–silicon (Al–Mg–Si) 6XXX series alloys. It is a very versatile material with applications in structural components for automotive and aerospace industries and for general use items like furniture [33], [34]. The major alloying elements in the system are silicon and magnesium which strengthen the alloy via precipitation [35] and provide corrosion resistance [36]. The alloy also has excellent formability and is, therefore, available in different forms like rods, bars, tubes, etc. The general composition of the alloy is given in table 3.1. The T6 grade is produced by first solutionizing at a temperature of around 533°C (990°F) for about an hour, followed by quenching in water. This ensures that alloying elements, Si and Mg are in solid solution in the aluminum matrix and do not precipitate out while cooling. It is then aged at around 300-500°F for 12-24 hours [37]–[39] depending on the part thickness to produce an array of ordered precipitates [(Mg_2Si)] increasing the strength to around 250 MPa [40].

Table 3.1. Chemical composition of Al 6061(wt%)

Mg	**Si**	**Cu**	**Mn**	**Fe**	**Cr**	**Zn**
0.91	0.8	0.321	0.212	0.456	0.021	0.178

A solid cylinder of Al 6061-T6 with a diameter of 25.4 mm, and cylindrical tubes with outer diameters of 25.4 mm, 12.7 mm and 6.4 mm respectively were chosen. The tube wall thickness was 1.2 mm for all three diameters, which corresponded to the chip or fiber width. Since deformation during machining occurred under plane strain (in the length-thickness plane), the width dimension was unaltered before and after deformation. Thus, all the fibers made for this thesis had a constant width of 1.2 mm. The microstructures of the solid cylinder and the tube, both having a diameter of 25.4 mm are shown in figure 3.5. The grains are predominantly equiaxed due to the tempering treatment with an average size of 25 μm for the tube workpiece and 75 μm for the solid cylinder. Impurity particles of

$[(Fe, Cr)_3SiAl_{12}]$ that do not dissolve during solutionizing, appear as the dark precipitates in the micrograph. The hardness of the tube was 112 VHN.

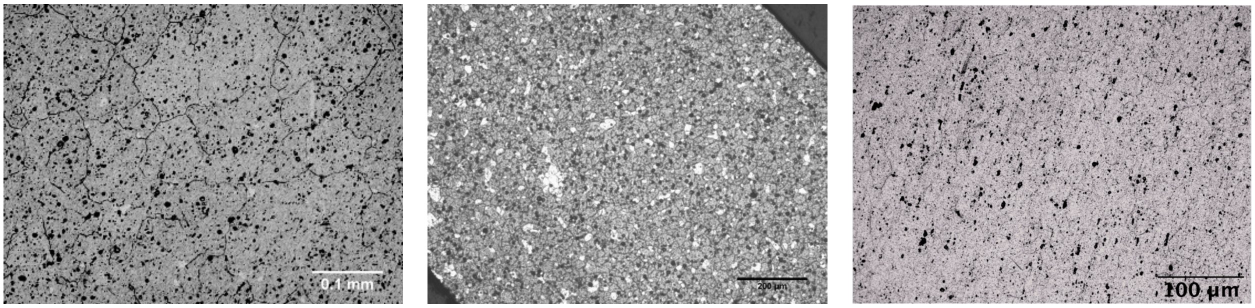

(a) (b) (c)

Figure 3.5. Microstructure of the (a) solid cylinder cross-section (b) tube cross-section (c) tube transverse section

3.3.2 Inconel 718

Superalloys, especially nickel-based, Inconel 718 are among the common alloys that are implemented in engines due to their high temperature and corrosion resistance. However, they are also difficult to machine due to the retention of high strength at high temperature and a low thermal conductivity [41]. Poor heat dissipation causes a significant increase in the cutting zone temperature, which results in overheating/burning and consequent changes in microstructure, phase transformations, heat-affected layers, etc. [42]. The high strength also leads to high cutting forces and subsequent tool wear. Surface irregularities, build-up-edges, and tensile residual stresses are a few of the other issues identified with the machining of superalloys [43].

An Inconel 718 tube of diameter 38 mm, and wall thickness of 0.8 mm was provided through the courtesy of Haynes International, Kokomo, Indiana. The alloy's nominal composition as per the specification sheet is shown in table 3.2.

Table 3.2. Chemical composition of Haynes Inconel 718 (wt%)

Ni	**Co**	**Cr**	**Nb+Ta**	**Fe**	**Mo**	**Ti**	**Al, Mn, Si, C, B**
0.52	.01	0.19	0.18	0.05	0.03	0.009	Rest

The tube microstructure is shown in figures 3.6a and 3.6b. Equi-axed grains in the cross-sectional and transverse directions show that the tube is in the solutionized state. High thermal and mechanical loads often result in thermal softening, localized shear and chip segmentation during cutting of Inconel 718 [44]. The effect of segmentation on the incipient chip morphology is key in the present study.

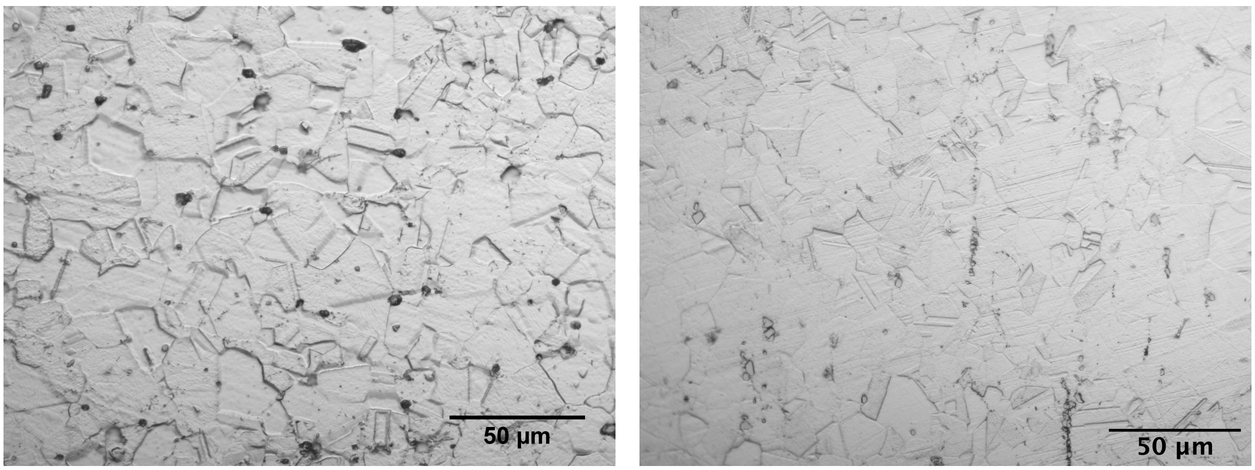

(a) (b)

Figure 3.6. Microstructure of Haynes inconel 718 in (a) cross-section and (b) tranverse direction showing equiaxed grains and twins, indicating that the material is in a solutionized/annealed state.

3.3.3 110 Copper

A solid cylinder of annealed commercially pure copper with a diameter of 23 mm was chosen as one of the workpiece materials. Copper has been of academic interest for deformation studies due to its ability to sustain large deformations. In the annealed state, material flow during cutting is highly nonuniform and mediated by a flow mode with significant rotation components referred to as sinuous flow [45]. It is of interest to observe what consequences will such a flow have on the chip morphology during interrupted cutting.

3.3.4 Titanium-6 Aluminum-4 Vanadium

Ti-6-4 is an important engineering alloy that is being increasingly used for aerospace applications due to its high strength to weight ratio. However, the high price of the alloy owing to its difficulty in processing and machining has constrained its use. Titanium alloys have a low thermal conductivity (resulting in elevated cutting temperatures), and a high chemical reactivity which contribute to increased tool wear in machining. Due to the high strength of the metal, machining also incorporates high forces and poses a challenge to obtain the desired surface finish from machining. Material flow during cutting is often localized leading to segmentation. A tube with an outer diameter of 8 mm and 1 mm wall thickness was used to produce fibers with MAM and to study the effect of saw-tooth-like chip formation, common in titanium alloys on the particle morphology.

3.4 Characterization

3.4.1 Particle size analysis

Dimensions of MAM particles were measured with the help of optical microscopy and digital image analysis. The fibers were laid flat on a piece of paper under the microscope and images were captured. From these images, each fiber was analyzed separately using quantitative image analysis to measure the fiber dimensions. The difference in the inner and outer diameters of the tube causes a variance in fiber length along its width. To incorporate that, length was measured at three locations along the fiber width to get an average length of individual fiber. For each processing condition, twenty fibers were analyzed, and the average value was reported. This method being intensive limits the number the particles that can be measured. In order to obtain better statistics, an automated particle size measuring instrument, Malvern Morphologi 3D was utilized. The fibers were laid flat in a similar fashion, but over a glass plate which formed the microscope stage. The lens then scanned over the plate in increments, taking images of the fibers. The instrument software reconstructed the images to identify each fiber separately and save it a separate image. These images were thresholded to measure the dimensions.

3.4.2 Observation of particle cross-section

To observe the flow lines caused by plastic deformation during cutting, it was essential to mount the fibers in a way that the cross-section could be imaged. The fibers being extremely thin, it was challenging to align them in the desired orientation. Further, an electrostatic interaction between the tweezers and the fibers, and between two fibers created a repulsive force due to which the fibers would move and/or reorient themselves once brought near another fiber. This problem was mitigated by laying the fibers on a piece of paper, with a layer of adhesive on it (figure 3.7a). In our case, the adhesive end of 'Post-it notes' was used. The weak hold of the adhesive prevented the fibers from moving to electrostatic forces while enabling physical maneuvering of the fibers with a set of fine tweezers. Once the fibers were placed nearly parallel to each other, a drop of epoxy was poured on the fibers and allowed to cure (figure 3.7b). This fixed the fibers to the paper which was then rotated and mounted in epoxy in an upright position such that the cross-section face was on the top of the mold (See figure 3.7). These samples were ground with silica grit papers 320, 600, 1200 and 2000, followed by polishing with a diamond paste of particle size 6 μm and 1 μm sequentially. Lastly, polishing was done with colloidal silica for 30 minutes. Etching was done with Keller's reagent for 10-15 s to reveal the precipitates that constituted the flow lines.

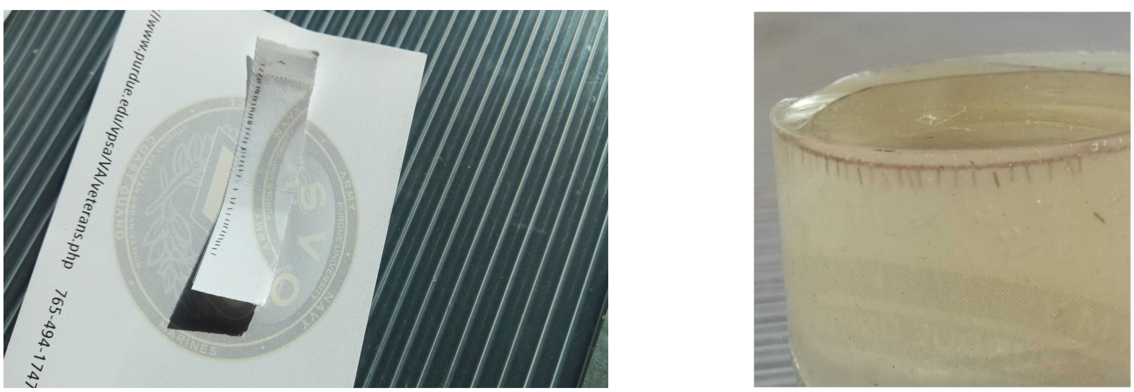

(a) (b)

Figure 3.7. (a) Fibers bonded to a piece of paper with the help of epoxy (b) The paper was mounted in an upright position to observe the fiber cross-section

3.4.3 Characterization with scanning electron microscopy

The surface topography of the fibers was observed under the SEM. Machined chips have a smooth rake face due to the sliding of the chip against the tool rake face and a rough back surface formed to the unconstrained material flow on the other side. The back surface was imaged to observe the lamella, that formed during deformation, which contained valuable information on the deformation characteristics of the material. To observe the plane of detachment of the fibers from the workpiece, they were mounted with the help of a steel clip and copper tape such that the width-thickness edge could be imaged. Imaging was done in FEI Quanta650 at 10 mm working distance, 20 keV accelerating voltage, and a spot size of 4.

3.4.4 Sample preparation and characterization in transmission electron microscopy

Deformation during machining orients the grains in a direction that is referred to as the direction of maximum elongation [46] that depends on the shear plane orientation. Extreme grain refinement also occurs due to the high shear strains [47]. Therefore, grains in a machined chip are usually not resolved under the SEM. TEM examination of Al 6061-T6 fibers made with MAM at 101 Hz frequency and chips made from continuous cutting was done to compare and contrast the microstructural changes that occur in steady-state vs. transient state of deformation. The location of the FIB lamella with respect to the cutting configuration is shown schematically in figure 3.8.

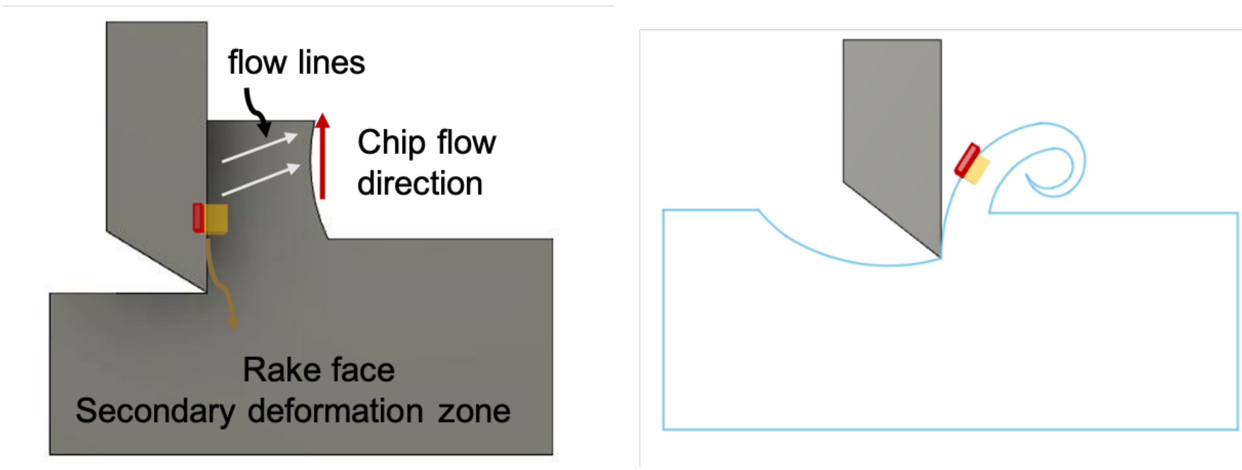

(a)

(b)

Figure 3.8. Showing schematically the location of the TEM sample for (a) a chip made with continuous cutting (b) a MAM chip. The region of interest is shown in yellow and the deposited Pt is shown in red.

Samples were prepared in an SEM, Helios G4, equipped with an ion source to perform focused-ion beam milling and lift-out. The fibers were cleaned with ethanol and laid on an SEM stub with carbon tapes attached on it, with the rake face on top. The tape held the fibers to the stub as well as provided a conducting path for the incident electrons. The main components of the SEM column are the focused Ga^+ ion beam and electron beam tilted by 52° relative to one another. The Ga^+ ion beam was used for milling, while the electron beam was used for imaging. The sample stage was positioned at 4 mm away from the pole piece which was then alternatively tilted in steps of 10° and translated in the z-direction (along the SEM column) to precisely position the region of interest at the 'eucentric point', which is the point of intersection of the two beams. This makes sure that further tilting of the stage during sample preparation does not cause the region to go out of focus for both the beams. While the sample stage was tilted at 52°, a 1.5 μm thick layer of Pt was deposited on the region of interest. The Pt layer is deposited to protect the material underneath from the damage that would be caused by splashing of high energy ions from the adjacent regions during milling. Two trenches were milled on the opposite sides of the Pt layer. A pattern of size 15 X 12 X 10 μm was drawn with the regular cross-section setting, which increased the milling depth as the beam moved closer to the region of interest. A high ion beam current

(21 nA) was utilized to cut the trenches within a reasonable time. After that, the stage was tilted back to 0° so that the U-cut could be made. This cut separates the lamellae and the bulk material, from the bottom and one of the sides. The EasyLift needle (tungsten tip) was then inserted in the chamber and carefully maneuvered to position the tip near the free end of the lamella. The tungsten tip was welded to the lamella via the Pt deposition process. Once the lamella is affixed to the needle, it would be released from the bulk by cutting the part connecting the lamella to the bulk. The lamella ($\sim$ 1-2 μm thick at this point) was then transferred to a Cu half-grid with the help of the EasyLift needle as shown in figure 3.9a. The edge of the copper grid was milled to render a flat area to which the lamella would be attached using the same Pt deposition process (figure 3.9b).

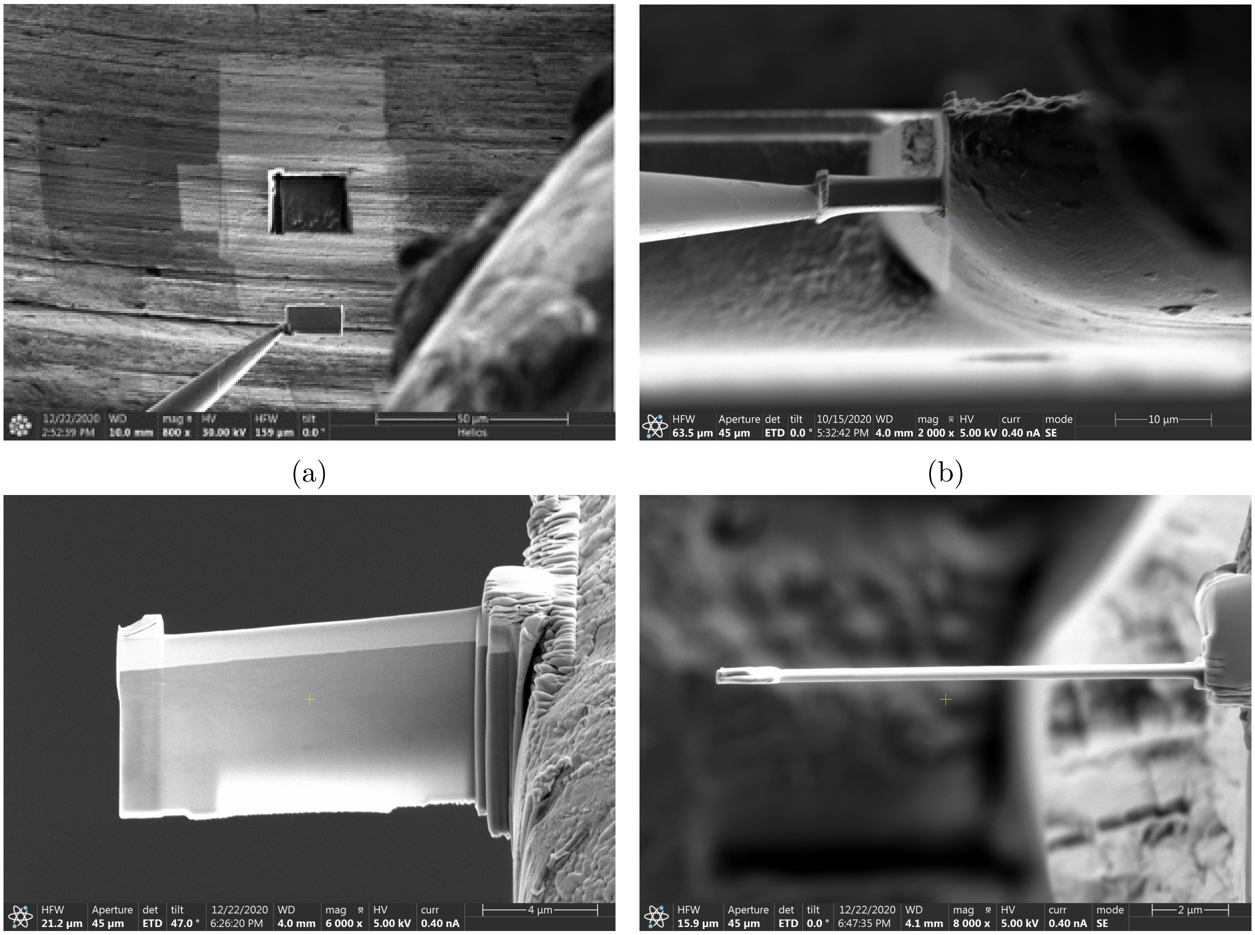

(a) (b) (c) (d)

Figure 3.9. (a) Showing the lift-out procedure using the tungsten needle (b) The lamella being welded to a copper grid (c) Lamella after thinning, the brightness is due to electron transparency (d) Transverse view showing the lamella thickness.

The last few steps are to thin the lamella down to below 100 nm in thickness to make it electron transparent. Thinning was done in consequent steps of reducing voltage and current to obtain the final surface with minimum ion beam damage. Firstly, the stage with the grid was rotated to 52° such that the lamella area is parallel to the incoming ion beam. The sample was thinned by drawing two rectangular patterns over and above the center region and milling at 30 keV, 0.26 nA. Milling was monitored by taking screenshots from the e-beam window at regular intervals and using the measurement feature on the software to estimate the lamella thickness. Once the thickness was around 300 μm, the voltage was changed to 8 keV and the current used was lowered to 40 pA. The stage was alternatively tilted to $\pm 2°$ to mill the top and the bottom part of the lamella respectively. Milling was continued till the lamella thickness was around 200 μm. The process was repeated with 5 keV voltage and 21 pA current to obtain a lamella thickness of below 100 μm. Lastly, both sides of the lamella were polished at 2 keV voltage and 17 pA current, one minute on each side to finish with a damage-free surface.

TEM specimen preparation using the FIB Lift-Out method provided an additional advantage of observing the grains through orientation contrast which is a result of electrons channeling into the material. An example of an SEM image showing this channeling contrast is depicted in figure 3.10.

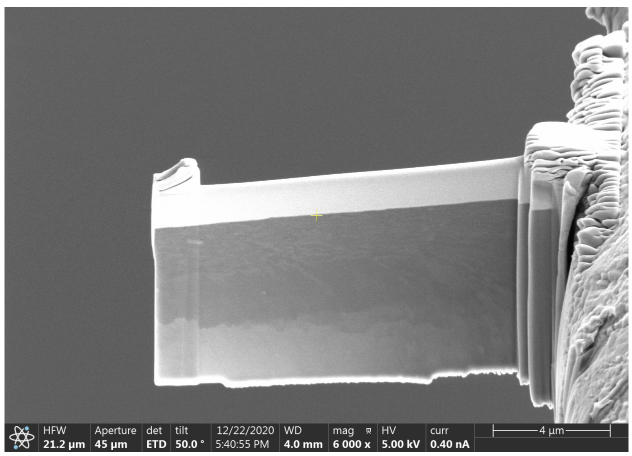

Figure 3.10. FIB lamella lifted out from a chip made with continuous cutting showing the grain structure due to orientation contrast.

The orientation (electron channeling) contrast is a result of these grains being oriented differently relative to the incident electron beam. The penetration depth of the incident electron beam into a material depends on the spacing between the atomic planes of the crystal and the atomic density of these planes. A longer length of interaction yields more secondary electrons from the surface, that are further detected by a secondary electron detector. The lower the yield of secondary electrons from a particular feature on the surface, the darker the feature would appear in the orientation contrast image. The secondary electrons originating from the interactions between the ion beam and the material produced orientation contrast images as shown in figure 3.10. TEM imaging was performed on a FEI Talos 200X transmission electron microscope equipped with the LaB6 filament. Bright-field (BF) images were taken to analyze the microstructure. The imaging area was $\sim 10\ \mu m^2$.

3.4.5 Hardness measurement

Hardness measurements were performed with Leco Vickers indenter as a measure of the shear strain of cutting. One indent was made on the polished cross-section of each fiber approximately at the center. For each cutting condition, 10 fibers were indented and the average was reported along with the standard deviation. The lowest load setting available on the instrument, 10g, was used to obtain a small indent, sufficiently far from the edges. The dwell time was 10s. Also, to get a hardness profile along the fiber length, a series of indents were made, positioned from the start to the end of the cut, along the fiber length. Indentation was performed with Nanoindenter XP, also on polished chip cross-sections, in the depth-controlled mode to a maximum depth of 1 μm.

3.4.6 X-ray diffraction

Powder diffraction studies were performed to determine the preferred orientation of the grains in the deformed chips. MAM fibers were randomly sprinkled into the slot to hold powders in an X-ray sample holder. Experiments were performed on Bruker D-8 diffractometer equipped with a copper k-alpha source. The divergence slit aperture was set to 2.5 cm to increase exposure to as many fibers as possible. Scans were performed from 2θ values of 15°- 90° at 0.05°/s scan rate. The intensity vs. 2θ data was plotted in MATLAB and cleaned with a background elimination algorithm [48]. The asymmetrical Huber function (one of the function options provided in the algorithm) was found to be the closest fit to the background and was applied to all the intensity plots. The corrected plot was further analyzed to determine the preferred orientation of the grains in the fibers.

3.5 Rolling experiments

Determination of strain in cutting requires precise measurement of undeformed and deformed chip thicknesses. In MAM, the uncut chip can only be approximated by modeling the tool movement caused by a specific set of parameters; however, any unpredicted change in these parameters will cause variations in the actual uncut chip shape. Although the physical motion of the tool was calibrated with the applied voltage and frequency in the MAM system, it was done only for free oscillation of the tool (unloaded or not during cutting). Upon engaging with the workpiece, cutting forces will reduce the actual modulation amplitude due to contact. The finite stiffness of the lathe machine will also affect the tool oscillation. These uncertainties, together with the varying chip thickness with length make it very difficult to physically calculate the strain in a MAM chip.

In a deformation-based process, the amount of strain imparted on the workpiece material directly controls the hardness of the final product. Thus, the strain in a MAM chip can be inferred indirectly from its hardness with the help of a strain-hardening relationship obtained from other conventional deformation processes. The strain-hardness relationship for Al 6061-T6 was determined by performing plane strain rolling on a bar of 64 mm width and 12.7 mm thickness of the same material. The setup used was Stanat TA215 with a roll diameter of 51 mm. Rolling was chosen as the deformation technique because the strain can be easily obtained by measuring the thicknesses of the bar before and after each pass. Rolling strain is calculated as,

$$\mathrm{e}_u = \ln h_f/h_o \tag{3.1}$$

where, h_i and h_f are the thickness of a plate before and after a roll pass. Rolling increments were chosen to obtain e_u from 0-4 at equal intervals of 0.5. The above equation assumes deformation to occur under uniaxial compression. However, since rolling occurs under plane strain conditions, a correction factor needs to be incorporated to calculate the effective strain,

$$\mathrm{e}_p = \mathrm{e}_u/1.15 \tag{3.2}$$

After each pass, a sample was cut from the edge to be mounted and polished for hardness measurements. The samples were cut with a large enough area such that measurements could be made avoiding the region at the end, where widening was seen to occur. The samples were mounted in epoxy, such that the cross-section of the bar was exposed and were prepared in a similar fashion as mentioned in section 3.4.5. Vickers hardness was performed with a load of 50 gf and 10s dwell time. Since these values will be compared to MAM chip hardness values which were obtained with a load of 10 gf, a few indents on rolling samples were taken at 10gf to examine if any difference was caused due to the different applied load. Minor variations were observed that are well within the error bars of each set of data for the respective loads. Thus, it was concluded that the two sets of data (the MAM chip hardness measured at 10 gf load and the rolling sample hardness measured at 50 gf load) could be compared without any ambiguity.

The indents were positioned approximately at the center of the cross-section across the width of the sample for the majority of the samples; see figure 3.11b. However, for lighter reductions, deformation only penetrates to a shallow depth into the plate thickness which often results in a variation in the hardness from the edges to the center of the plate. For strain, $e_u = 0.5$ and 1, indents were positioned both across the sample width and the sample thickness to identify any variation in the hardness that may be present due to the insufficient deformation penetration. Figures 3.11a and 3.11b show the position of the indents on the plate cross-section for these two configurations.

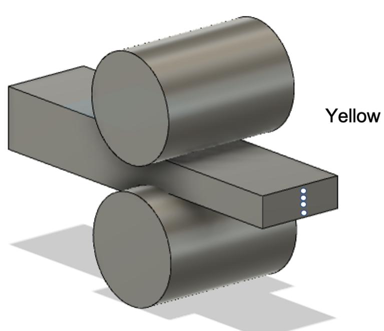

(a) Across sample thickness

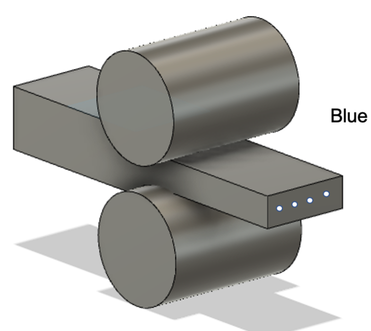

(b) Across sample width

Figure 3.11. Showing the position of hardness indents.The data for each condition is represented by the colour mentioned.

The average of the indents taken along the centerline (across width, blue points in the figure) was lower than the average of the indents across thickness (yellow points) as shown in figure 3.12. This suggests that the deformation was mostly limited to the top and bottom edges of the plate resulting in a higher hardness near the sample ends than the sample interior. To get a true average of the sample, indents were made on a 5X5 matrix of points all over the sample cross-section (only for the conditions, $e_u = 0.5, 1$) and the average was reported as the sample hardness.

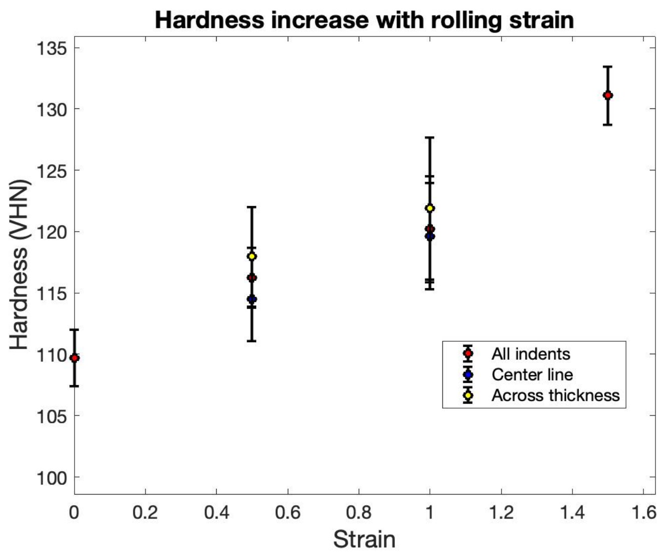

Figure 3.12. Hardness variation between indents positioned along the center line of the cross-section and along the thickness direction for the first two passes.

The results of these characterization techniques applied on the machined chips are discussed in the following chapters.

4. PARTICLE MORPHOLOGY

One of the main objectives of the study was to identify the accuracy with which the MAM system can produce particles of target dimensions. Multiple cutting parameters (modulation frequency, workpiece diameter, rotational frequency) were varied systematically, and the corresponding particle morphology was characterized both qualitatively and quantitatively. Due to plane strain deformation conditions, changes in chip dimensions occurred only over the fiber cross-sectional plane, therefore, the study focused only on the variation in particle length and thickness only, as defined in figure 2.9 with the variation in process parameters. In turning of tubes, the difference in chip velocities at the outer and inner diameters has been known to cause chip side flow [2], thereby, changing the chip width. However, the degree of change in the width direction was minimal (<10%) for the fibers produced in this study and thus, this change has been ignored in the analysis presented in the thesis.

4.1 Effect of process parameters on fiber morphology

4.1.1 Effect of modulation frequency

Modulation frequency controls the number of cuts per unit time. A lower frequency will result in a longer time between two cuts. For a constant circumferential velocity of the workpiece, a longer time of engagement will produce a larger particle. This has been illustrated schematically in figures 4.1a and 4.1b, and with fibers produced at 101 Hz and 401 Hz in figures 4.1c and 4.1d. Recall that the depth of cut/ particle width was the larger dimension leading to the fiber morphology of the particles. Thus, the longest dimension of the fibers shown in figures 4.1c and 4.1d, which is conventionally referred to as fiber length, is however the chip width as per the cutting configuration. Two distinct surfaces with contrasting roughness can be observed. The chip width-length plane that was in contact with the tool is called the *rake face*. Due to a sliding motion against the tool face, this plane has a smooth appearance. The alternate "free" *back face* accommodated the irregularities in material deformation caused by the presence of stress concentration or weak points in the material [2]. When a shear plane passed through a point of stress concentration, material deformed at a lower flow stress than the surrounding area. This led to an inhomogeneous strain and therefore, an uneven chip thickness. The back face is characterized by a dull appearance in the figures below.

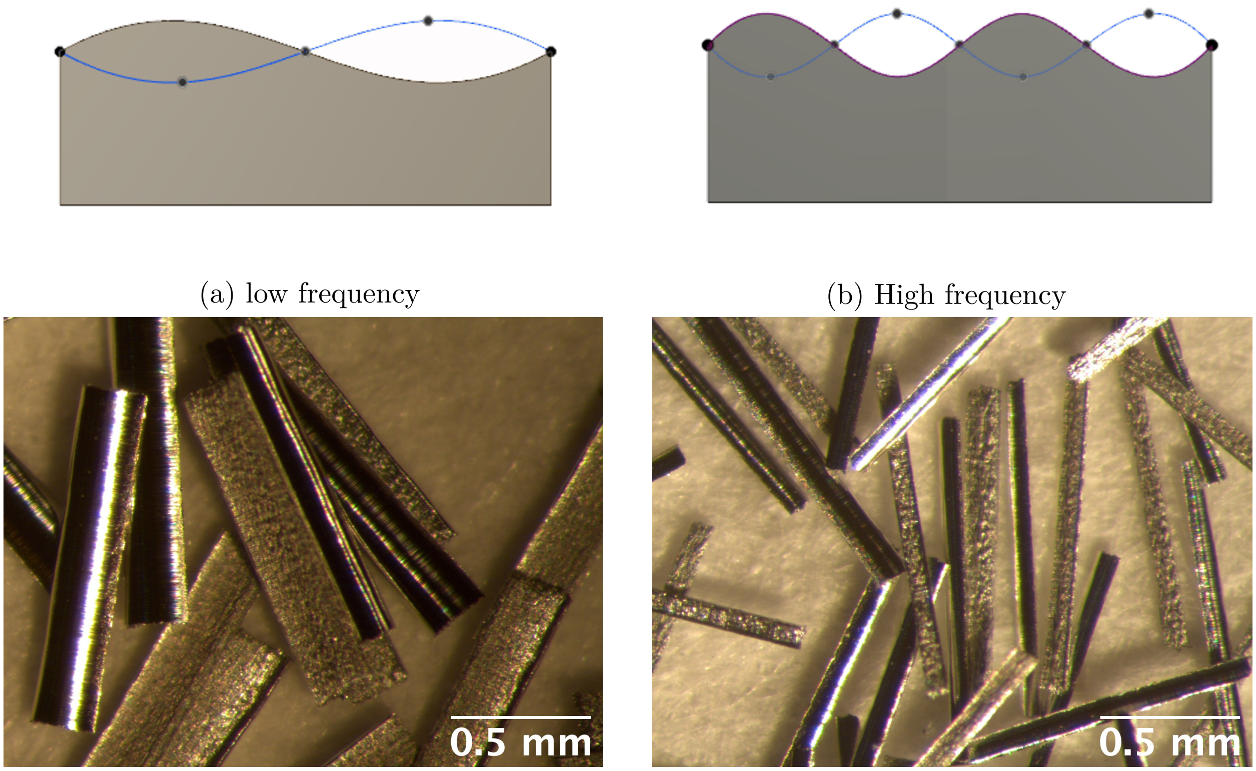

(a) low frequency

(b) High frequency

(c) 101 Hz

(d) 401 Hz

Figure 4.1. Schematic of the tool path with (a) low modulation frequency and (b) high modulation frequency showing the decrease in cutting length with increasing frequency. Fibers cut from Al 6061 tube with d = 25.4 mm at modulation frequencies of (c) 101 Hz (d) 401 Hz showing decreasing fiber length with increasing modulation frequency.

4.1.2 Effect of workpiece diameter

The length of a chip/fiber is the distance traveled by the tool along the cylinder circumference through the duration of each modulation cycle. Thus, a higher workpiece surface velocity produces a longer chip. The surface velocity of the workpiece is directly related to the diameter and the rotational frequency. Thus, with a constant RPM, the length of fibers increases with the diameter of the workpiece (d) used. Fibers machined from tubes with d= 25.4 mm, 12.7 mm and 6.4 mm are shown in figure 4.2. Due to the circular geometry of the workpiece, fibers are tapered along the width direction. The degree of taper is lower for a larger workpiece because of the smaller relative difference between the inner and outer diameters. For fibers made with the same diameter, the taper is more prominent when the average length is smaller. Thus, for a high f_m of 401 Hz, fibers made from the largest workpiece (d=25.4 mm) had nearly constant lengths across its width (figure 4.2c), while for the smallest workpiece (OD=6.4 mm), they narrowed down to a point (figure 4.2a).

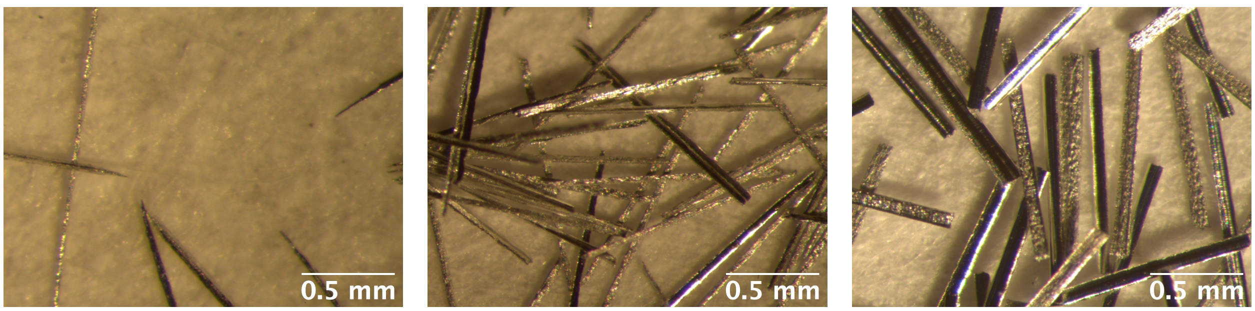

(a) (b) (c)

Figure 4.2. Fibers cut from a tube workpiece with outer diameter, d = (a) 25.4 mm (b) 12.7 mm (c) 6.3 mm, at f_m = 401 Hz, showing decreasing length with decreasing diameter and a more prominent taper in fibers made from the smallest diameter.

4.1.3 Effect of spindle speed or the ratio of frequencies

As mentioned in section 4.1.2, a higher workpiece surface velocity results in longer chips. Surface velocity can also be controlled through the rotational frequency or the RPM of the workpiece. The ratio of modulation frequency to the workpiece rotation frequency controls the number of cuts per rotation and recalling from equation 2.18, can have discrete values depending on the value of n. This variable is set as per the particle size requirements; a higher ratio produces a smaller length. It is also apparent that an increase in both the spindle speed and the modulation frequency, keeping the ratio constant, will not produce any effect on fiber dimensions. This has been observed in the experiments and is illustrated in figure 4.3 below.

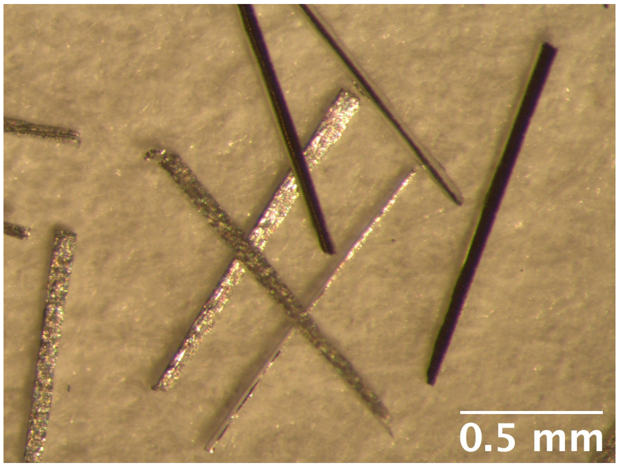

(a) 45 RPM, 38 Hz, $f_m/f_w = 50.5$

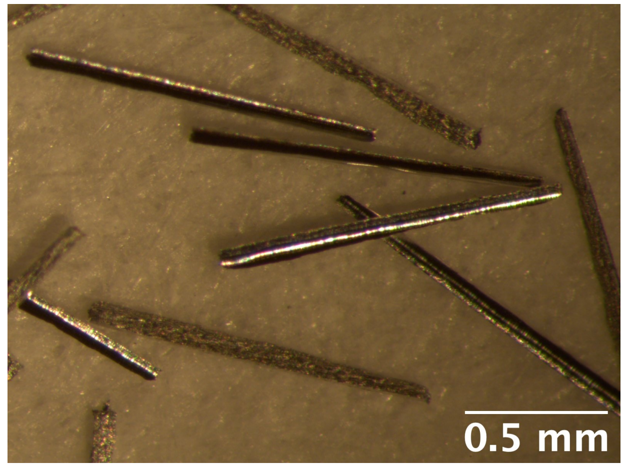

(b) 120 RPM, 101 Hz, $f_m/f_w = 50.5$

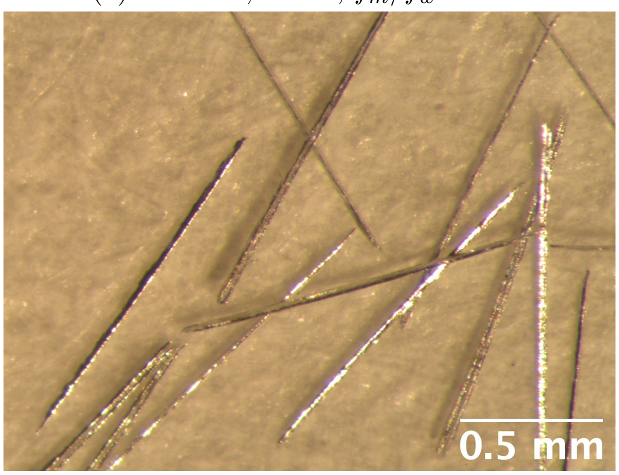

(c) 45 RPM, 189 Hz, $f_m/f_w = 250.5$

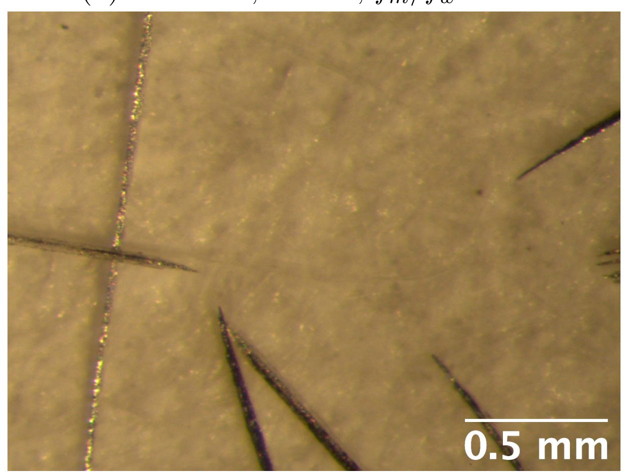

(d) 120 RPM, 401 Hz, $f_m/f_w = 250.5$

Figure 4.3. Fibers cut from a tube with d = 6.4 mm at varying f_m/f_w ratios showing decreasing particle length with increasing frequency ratio.

Figures 4.3a and 4.3b show fibers cut at two modulation frequency and rotational frequency combinations. However, since their ratio is same (50.5), fibers produced have the exact dimensions. Figures 4.3c and 4.3d show fibers cut at a much higher ratio (250.5), i.e., the frequency of cutting was much higher than the rotational speed resulting in slender fibers.

4.2 Particle size measurement

The kinematic relationship given by equation 2.19 was used to calculate the undeformed particle length. To predict the deformed dimensions, a cutting ratio (r) value of three was assumed, as was determined from a previous study for a modulation frequency range of 30-90 Hz [25]. The predicted length of the particles, $l_{cpredicted} = \frac{l_o}{3}$ is plotted as a solid line in figure 4.4.

Initially, plan-view images of the fibers were captured with the help of a Paxcam camera fitted to an optical microscope. Quantitative analysis of these images was performed with ImageJ to measure the chip length. The process for imaging and analyzing each fiber separately was labor-intensive, which limited measurement to only a few fibers for few conditions. An automated particle size measurement system was then utilized to measure the lengths of >500 particles for each frequency and for frequencies from 51 Hz-999 Hz. This is plotted as the data points in the figure below.

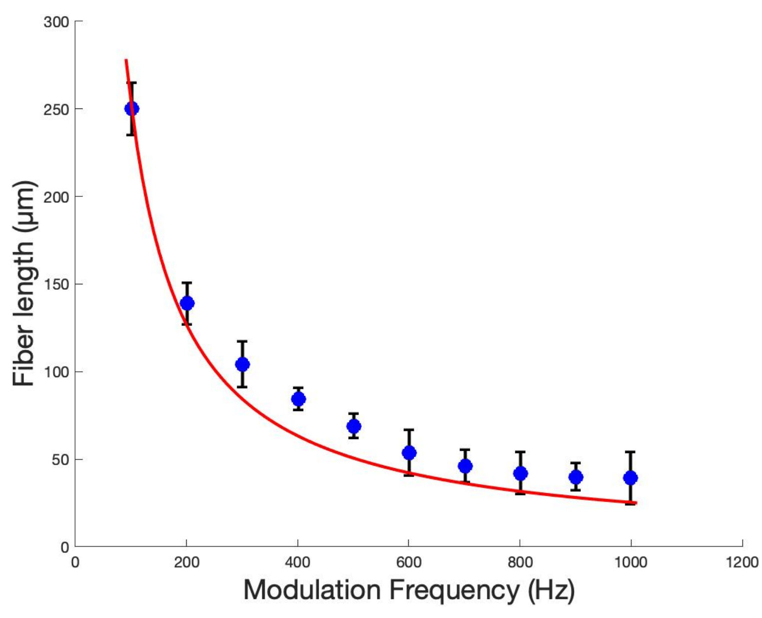

Figure 4.4. Predicted (solid line) and measured chip length vs. modulation frequency.

The calculated length (solid line) shows a gradual decrease in fiber length, following the shape of a reciprocal function, $(L \propto 1/f_m)$. There is good agreement between the predicted and the measured dimensions; the slight mismatch arises possibly from the assumption of a constant cutting ratio, r, for all the frequencies. The cutting ratio is a function of the amount of strain imparted onto the material during cutting. It will be shown later that the deformation varies with the frequency of cutting, thereby, a change in r is expected. The curvature in the fibers is another source of error since imaging was performed in 2-D and the length measured (projected length) was affected by how each fiber rested on the microscope stage. Note that the undeformed length calculated using process kinematics also gives a projected length (figure 2.9). The assumption of plane strain conditions in the equation relating cutting ratio to the chip dimensions can also incorporate errors in the predicted length values. Nevertheless, even with these challenges, the kinematic equations could predict the particle dimensions within 10% error for most modulation frequencies. In other words, MAM process parameters can be tailored to match a target particle size.

4.3 MAM particle cross-sectional shape

In modulation assisted machining, the undeformed cross-section of a particle is determined by the locus of the tool inside the workpiece. To visualize the tool path, a numerical simulation was performed by superimposing sine waves with frequency and amplitude corresponding to the experimental modulation parameters.

4.3.1 Prediction and observation of particle shape

The sinusoidal nature of modulation was expressed as a function of the position coordinate, x, following equation 2.16. If f_m is the modulation frequency, the number of modulation cycles, or the number of sine waves in one rotation of the workpiece is $f_m \cdot T$ (time period of rotation) or f_m/f_w. Since in time T, the tool covers a distance of one circumference, the wavelength, η will be given by the fraction of tube circumference traversed per modulation, i.e., circumference/number of modulation cycles, $\lambda = \frac{\pi d f_w}{f_m}$. Therefore, using the values of process parameters used in this study, equation 2.16 can be written as,

$$y_n = A \sin\left(2\pi x/\lambda + n\pi\right) - n s_o \tag{4.1}$$

where, A $=$ half amplitude $=0.075$ mm, s_o $=$ feed per rotation $=$ 0.005 mm and λ $=$ wavelength $= (\pi \cdot 25.4 \cdot 2)/101 = 1.579$.

The sine waves obtained from equation 4.1 were superimposed, each pass anti-parallel to the one before and after and with an offset in the Y-axis corresponding to the tool's feed rate. The phase difference between consecutive passes was applied by incorporating $n\pi$ in the above equation. The tool passes take the form shown in figure 4.5.

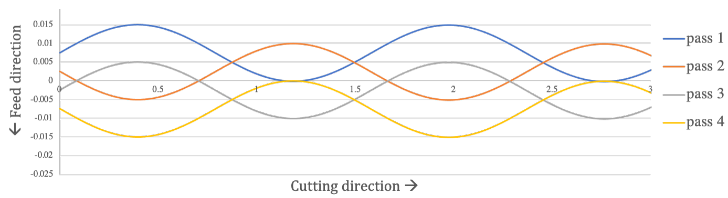

Figure 4.5. Tool paths for the first four passes for f_m =101 Hz, f_w = 2 Hz, A= 7.5 μm, $s_o = 5\ \mu m$

The undeformed chip shape can be modeled by separating the passes in the above figure and identifying the overlapping area between an n^{th} pass and the workpiece surface profile after the $(n-1)^{th}$ pass. The prediction showed that it takes three passes for the process to achieve a steady-state chip shape with a uniform thickness (figure 4.6).

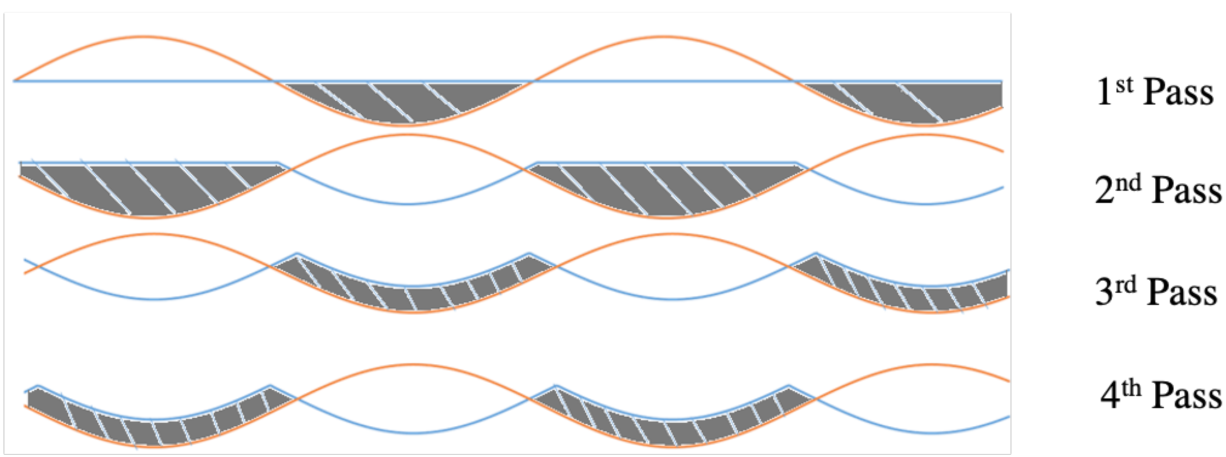

Figure 4.6. Simulation of tool passes for f_m = 101 Hz. The orange line is for the tool pass, and the blue line is for the workpiece surface after the previous pass. The shaded area shows the steady-state ideal uncut cross-sectional shape of the particle.

Experimentally observed cross-sections of particles produced at three frequencies are shown in figure 4.7. The bottom and the top edge of the cross-section correspond to the chip rake face and back face; characterized by the smooth and rough surface profiles respectively. Unlike the prediction, the thickness of the fibers is non-uniform, with a curl at one end, a region of nearly constant thickness in the middle, followed by narrowing down to the other end (figure 4.7). Chip curl is commonly observed while cutting ductile materials for smaller undeformed thicknesses. At the start of cutting, a small volume of material, removed as a chip, undergoes bending away from the tool face. The process continues until the energy required to further bend this strain hardened chip is greater than that required to overcome friction at the tool-chip interface [2]. Thus, the presence of curl indicates that cutting started from the thinner end.

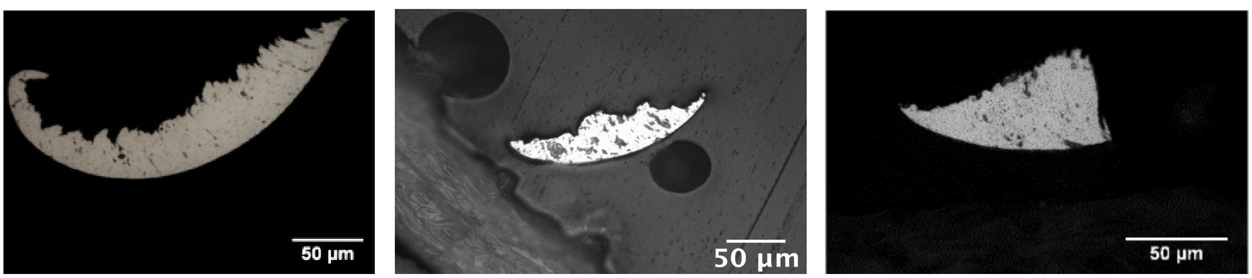

(a) 101 Hz (b) 201 Hz (c) 401 Hz

Figure 4.7. Typical cross-sections of fibers produced at different modulation frequencies. Note the scale bar difference in the figures to appreciate the reduction in chip length with the increasing modulation frequency.

Fiber cross-sections were etched with Keller's reagent to reveal the flow lines. Cross-sections included in figure 4.7 show the precipitates in Al 6061 aligned in the direction of chip flow. In a cutting configuration, flow lines are inclined back toward the start of the cut. Thus, the flow line orientation is consistent with the hypothesis that the thinner curled end is the start of the cut. It was observed that some fibers machined at 101 Hz have a straight edge, as shown in figure 4.8. This feature is presumed to be a result of shear fracture of the chip towards the end of the cut and has been discussed later.

Figure 4.8. Cross-section of a MAM fiber machined with conditions, d = 25.4 mm, f_w = 2 Hz, f_m = 101 Hz, showing a sharp edge towards the end of the cut.

4.3.2 Effect of parameter inconsistencies

The observation of a relatively thicker end and a thinner start can manifest from variations in the undeformed geometry. These variations can occur when the MAM process conditions do not follow the optimum discrete chip formation conditions described in equation 2.18. Under such non-exact modulation conditions, phase differences between consecutive tool paths vary and thus, produce an irregular thickness in the undeformed chip shape. To motivate this idea, chip cross-section predictions was performed on two “offset” frequencies, 100.6 Hz and 101.4 Hz, both being at equal offsets from the ideal modulation frequency of 101 Hz. Sinusoidal waves were superimposed with a phase difference in the position corresponding to a 0.4 offset in frequency. This has been illustrated in figure 4.9, the dashed lines showing the direction of chip flow.

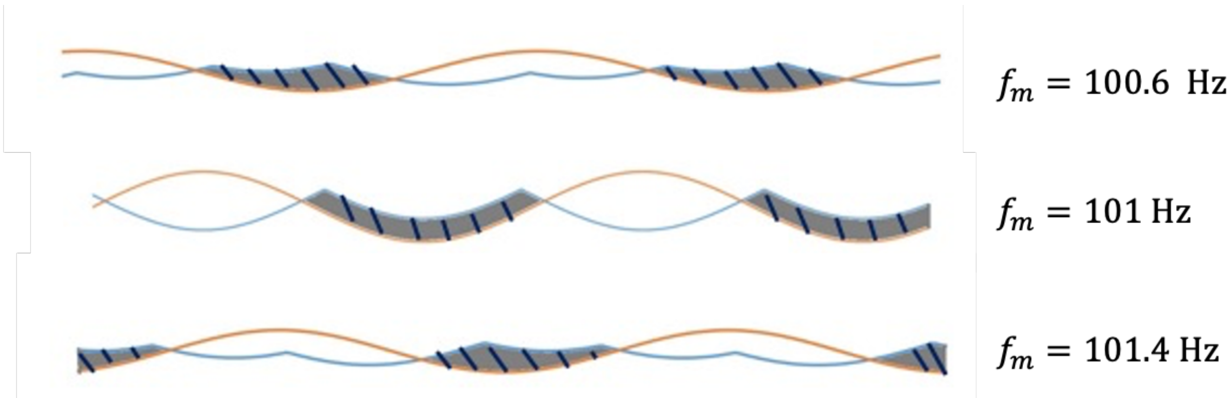

Figure 4.9. Undeformed cross-section predictions for two offset conditions showing the reversal of the thicker and the thinner end depending on the offset direction.

The mathematical visualization of the tool path and the corresponding uncut chip shape predictions suggest that the thick and the thin end can be an attribute of the uncut chip geometry in the event of an "offset" from the exact condition of modulation. For a fixed offset (in this case of 0.4 Hz) from the ideal condition of 101 Hz, the position of the thick end is reversed. It is thicker towards the start of cut in 101.4 Hz and toward the end of cut for 100.6 Hz. Such predictions have also been made by Eren et. al. [29], while simulating chip shapes in modulated cutting systems as a function of the phase difference between consecutive tool paths.

To observe if the flow lines have reversed in our case, machining was performed at intermediate frequencies between 100 Hz to 200 Hz to inspect change in the flow line orientation, if any. Chip cross-sections observed for these conditions are shown in figure (4.10).

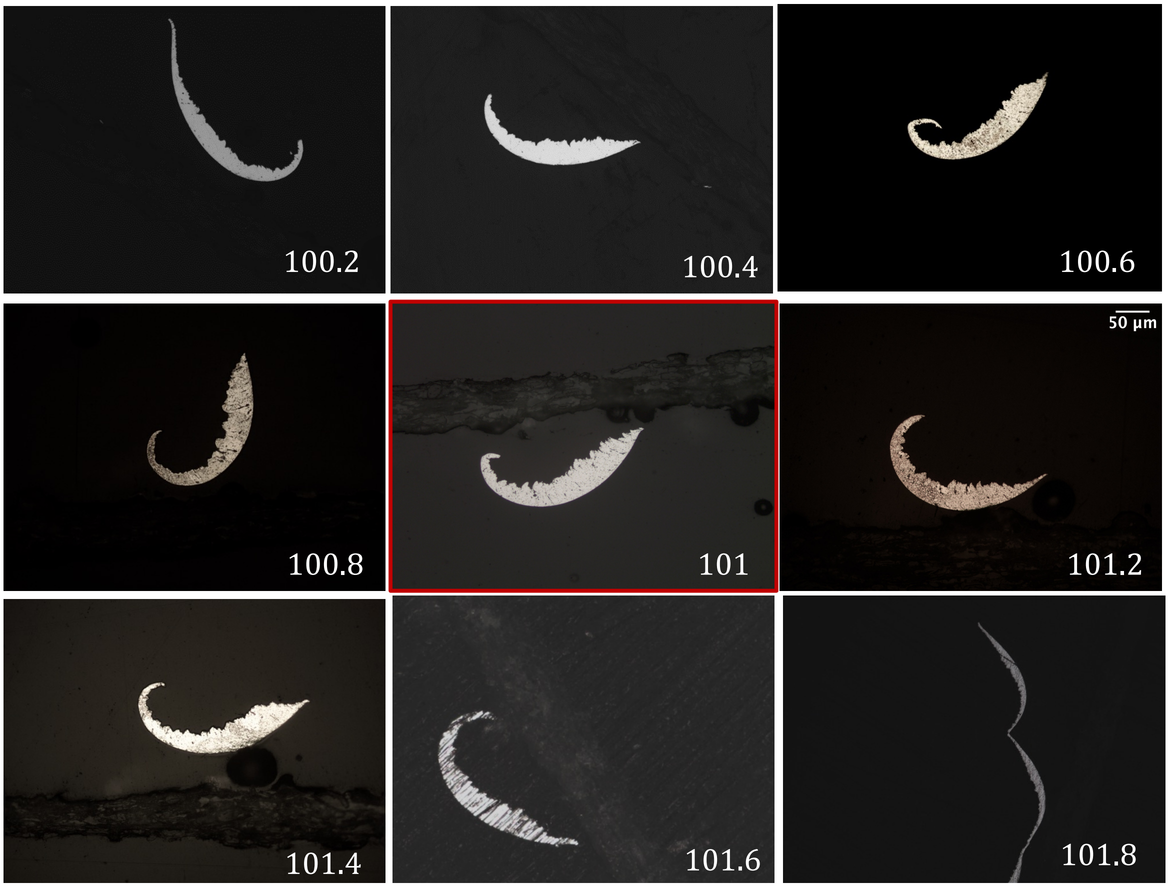

Figure 4.10. Cross-sections of fibers produced at offset conditions of modulation frequency (in Hz) showing the gradual change in morphology from nearly continuous to discrete to nearly continuous again.

The prediction of mathematical does not incorporate the deformation during chip formation. However, under steady-state orthogonal cutting assumptions, the deformed chip shape should exhibit a uniform increase in the chip thickness and a corresponding decrease in length. The experimentally observed chip shapes are largely non-uniform displaying a similar curl and gradually increasing chip thickness. For the boundary conditions of f_m = 100.2 Hz and 100.8 Hz, the chips were elongated and occasionally welded to each other signifying notable deviation from the ideal discrete chip formation conditions. Flow lines on chips made at four separate frequencies are shown in figure 4.11.

Figure 4.11. Cross-sections of fibers made at offset frequencies showing the flow lines oriented toward the thinner curled end irrespective of the offset direction.

In contrast with the prediction, it was observed that for both directions of offset, flow lines aligned toward the thinner curled end, suggesting that the non-uniform thickness do not arise from the differences in uncut chip shapes but likely from the variation in deformation from the start of the cut till the end of the cut. It is, therefore, evident that deformation plays a more dominant role in controlling the fiber's final shape, so much that it can mask the effect of varying undeformed geometry, to begin with.

4.4 Effect of workpiece material on particle size and shape

Modulation-assisted machining was also performed on copper, titanium grade 5 and Inconel 718 to examine the material cutting behavior on the particle morphology. The undeformed length of fibers made from Ti-6-4 tube was calculated using the same kinematic equations used in section 4.2 and is plotted with the measured deformed chip lengths in figure 4.12. The difference between the predicted and measured fiber lengths is significantly lower for higher modulation frequencies. This suggests that the cutting ratio (the ratio of the undeformed lengths/thicknesses) cannot be assumed to be a constant parameter in interrupted cutting techniques.

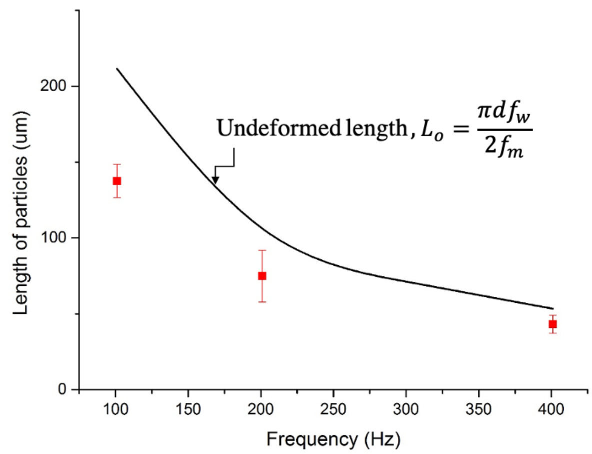

Figure 4.12. Deformed (data points) and undeformed (solid line) lengths of Ti-6-4 fibers showing that the difference decreases with increasing modulation frequency.

The average cutting ratio was only 1.4 for titanium as compared to 3.2 in the case of Al 6061-T6. The measured cutting ratios of the materials used in the study are presented in table 4.1 along with the tube hardness (measured for Al 6061 and obtained from the material manufacturer for the rest).

A strong correlation is observed between the material hardness and the cutting ratio. Cutting ratio is higher for materials that can sustain a large amount of shear. Harder materials tend to undergo localized deformation and fracture during machining limiting the amount of shear strain that can be imposed over the chip volume. Premature fracture could also lead to a shorter chip length and can be a source of error in comparing the deformed length of fibers for Inconel 718 to the uncut length. Thus, caution must be exercised while

Table 4.1. Cutting ratio and the approximate tube workpiece hardness of alloys used in the study

Material	Hardness (VHN)	Cutting ratio
Al 6061	112	3.2
Copper	77	3.8
Ti-6-4	300	1.4
Inconel 718	350	2.2

comparing these values. Nevertheless, the difference in the cutting ratios of Al 6061 vs. Ti-6-4 is substantial and is manifested in the form of a smaller decrease in chip length for the latter.

The cross-sections of fibers made from the different alloys for similar cutting conditions are shown in figure 4.13.

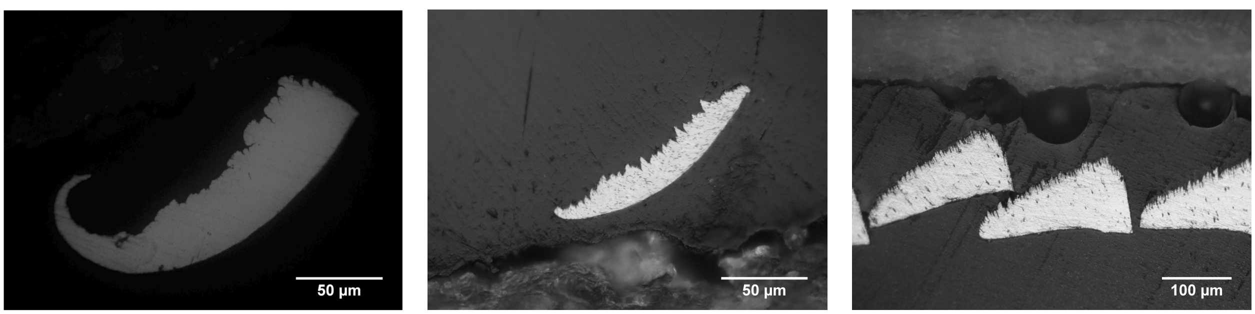

(a) copper, d = 23 mm (b) Ti-6-4, d = 8 mm (c) Inconel 718, d = 38 mm

Figure 4.13. Cross-section of fibers machined from different alloys with the same condition of f_m = 101 Hz, f_w and 2A= 15 μm, showing the non-uniform thickness of fibers.

Note that each of these fibers has a different length resulting from the difference in respective tube diameters. However, they also share several key features, such as the thickness of the fibers is non-uniform, thinner at the start and thicker at the end. Flow lines also orient toward the thinner end suggesting that for all the materials, thickness increases from the start to the end of the cut. An interesting feature of the Inconel fiber cross-sections was that a majority of them had a straight edge at the "end of the cut" side which was observed only for fibers machined at higher frequencies for Al 6061 (figure 4.7c) and Ti-6-4 (figure

4.14b) suggesting that:

a. Chips are more prone to fracture when cutting at high frequencies.

b. Harder workpiece materials undergo fracture even at lower frequencies.

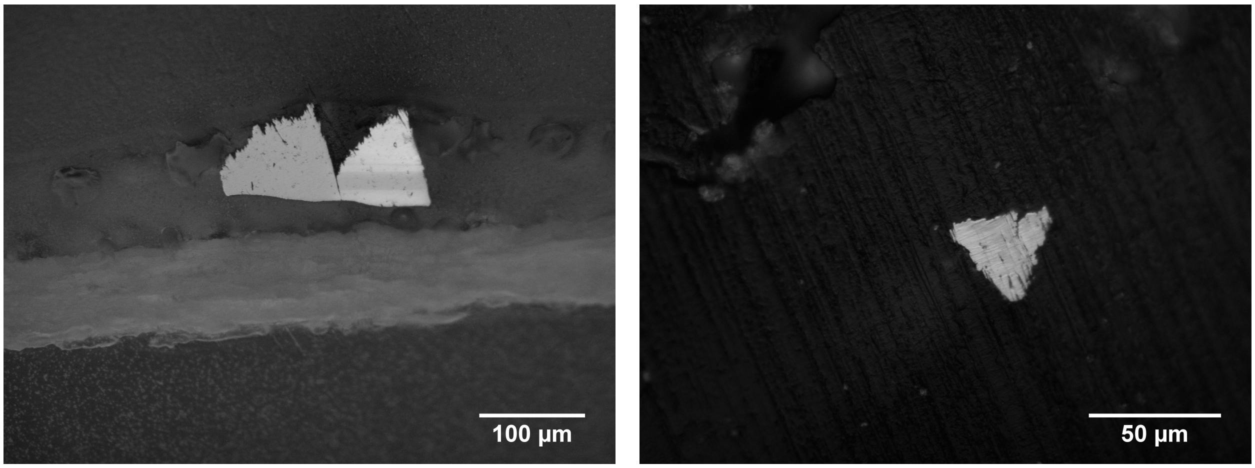

(a) copper (b) Ti-6-4

Figure 4.14. Cross-section of fibers machined from Ti-6-4 and Inconel 718 at higher frequencies showing the presence of shear fracture end.

4.5 Surface quality of chips

As shown earlier in section 4.1.1, machining chips have a smooth rake face and a rough back face. This roughness arises from the presence of points of stress concentration in the workpiece material that causes the small volume of material in the primary deformation zone to deform at a lower stress. Figure 4.15 shows that material flow in the chips occurs in the form of a *lamella* of thickness around 1-2 μm. the formation of these lamellae stems from the finite thickness of the deformation zone, as opposed to one atomic layer thick shear plane assumed in most studies of cutting mechanics. The thickness of the lamella has been shown to be independent of grain size [49] or processing parameters, except for cuts made with extremely low undeformed thickness $<$ a few micrometers [50]–[52], where the lamella size increases with the uncut thickness.

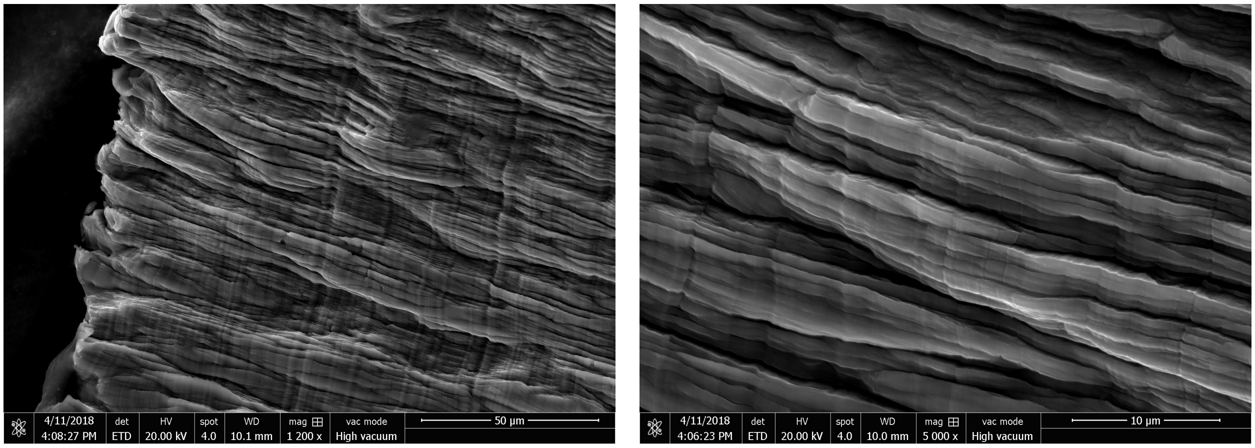

(a) (b)

Figure 4.15. (a) Low magnification and (b) high magnification of the back surface roughness on particles produced at 101 Hz showing the lamellar structure.

Chip surface roughness was measured with optical profilometry and the results are shown in figure 4.16. The R_a observed for the MAM chip made at 101 Hz was 13 μm and that for CC was 15 μm. Due to the curvature of a MAM chip, the surface roughness is overestimated, as seen from the SEM images of the back surface.

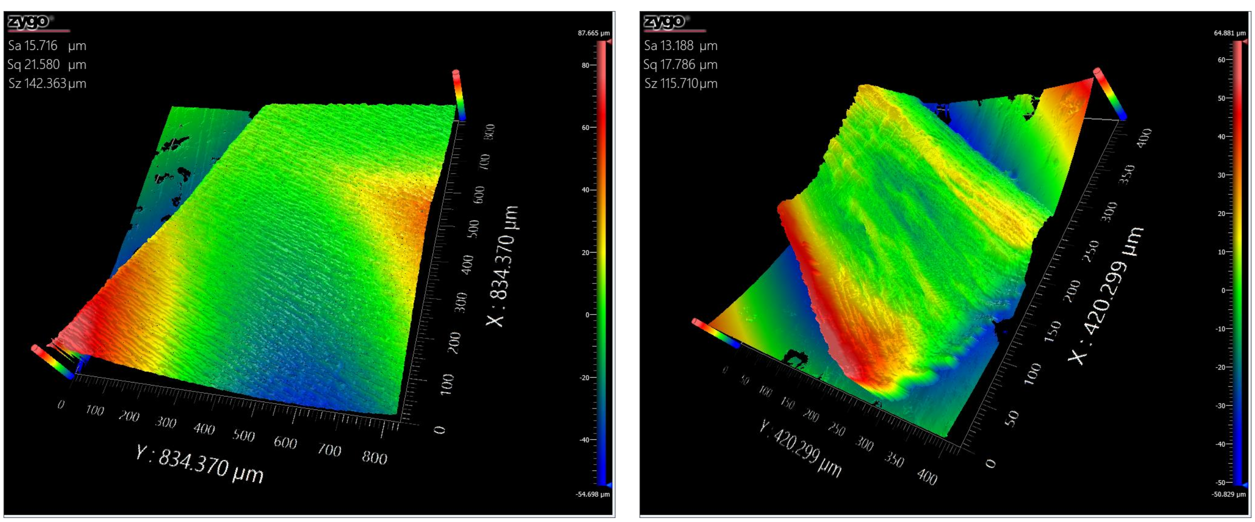

(a) (b)

Figure 4.16. Reconstruction of the back surface of Al 6061 particles produced at 101 Hz through optical profilometry.

A correction factor was applied to eliminate the curvature in the chip surface and measure the local surface roughness, as shown in figure 4.17a and 4.17b. The profile along the chip length is also included with the reconstructed surface. The corrected surface roughness was 2.3 μm for the MAM chip and 1.7 μm for CC.

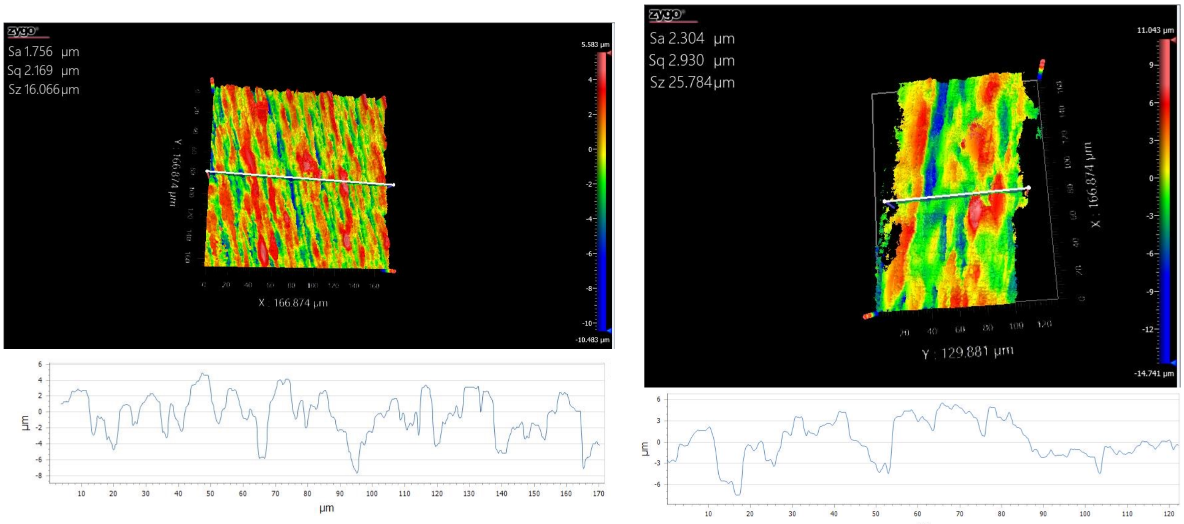

(a) (b)

Figure 4.17. Reconstructed surface after correcting for chip curvature.

4.6 Fractography

It is now established that depending on the working material and the operating frequency, at the end of a cutting cycle, chip thickness either decreased to a point or continued to increase till the end of the cut. In the latter case, the cross-section of the fibers displayed a relatively straight edge on the thicker end. The plane along which a chip detached from the workpiece after the end of a modulation cycle was examined to identify the mode of fracture. The fibers were positioned such that the width-thickness plane could be imaged in an SEM. Figure 4.18 shows that for Al 6061 fibers machined at 101 Hz, some fibers undergo ductile fracture (thickness of edge $\sim$ 10 μm as shown in figure 4.18a) while some show shear fracture (thickness of edge $\sim$ 30 μm as shown in figure 4.18b) as characterized by a flatter and thicker plane. Fibers machined at a higher frequency of 401 Hz primarily displayed the presence of a shear fracture end (figure 4.18c).

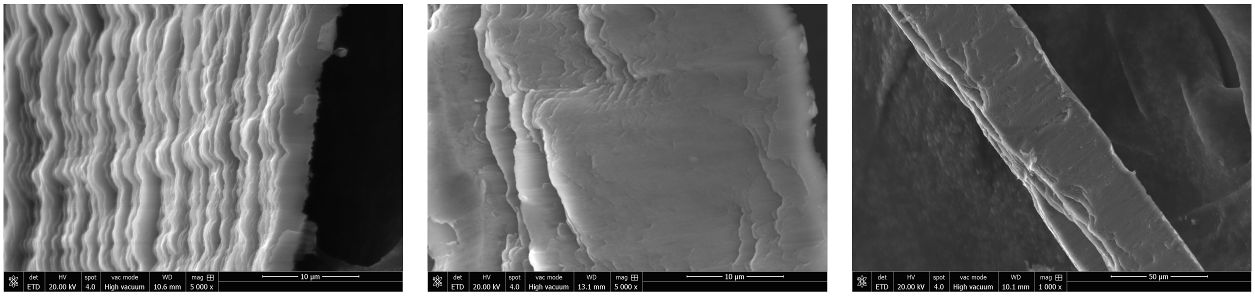

(a) (b) (c) 401 Hz

Figure 4.18. Fracture plane of Al 6061 chips made at (a) 101 Hz, showing the completion of cut (b) 101 Hz showing fracture (c) 401 Hz, showing shear fracture.

Observation of the fracture surface explains the occurrence of the straight edge observed on some of the fiber cross-sections. Due to the build up of strain at the tool tip, a crack may initiate that will lead to the fracture of the chip before the undeformed thickness goes to zero resulting in the flat fracture surface on some Al 6061 fibers. Systematic studies of inspection of fiber cross-section were performed to assess the probability of occurrence of the fractured end vs. the pointed end. It was found that for four batches of fibers, the cross-sections showed both a flat fracture edge and a pointed end but each batch was either predominantly fracturing at the end (20/25 exhibited a flat edge) or thinning down to a point, even though the cutting conditions were nominally identical. Thus, the occurrence of shear fracture can arise from the process instabilities and/or the distribution of flaws in the workpiece material that would initiate the fracture. Further studies on in-situ observation of chip formation can probably help identify the predominance of one mode over the other.

Alloys with a higher hardness are more prone to fracture and this has been observed in MAM while cutting with Ti-6-4 and Inconel 718. These alloys are known to produce serrated or *saw-toothed* chips due to the periodic generation of shear cracks that initiate at the chip surface, and propagate toward the tool tip along the shear plane [53]. Thus, the occurrence of shear fracture is frequently encountered in particles machined out of harder (more brittle) materials due to the increased probability of crack formation. In the event of strain localization followed by fracture, the majority of the chip volume is exposed to much lower strains which justifies the lower cutting ratio for chips made at a higher frequency.

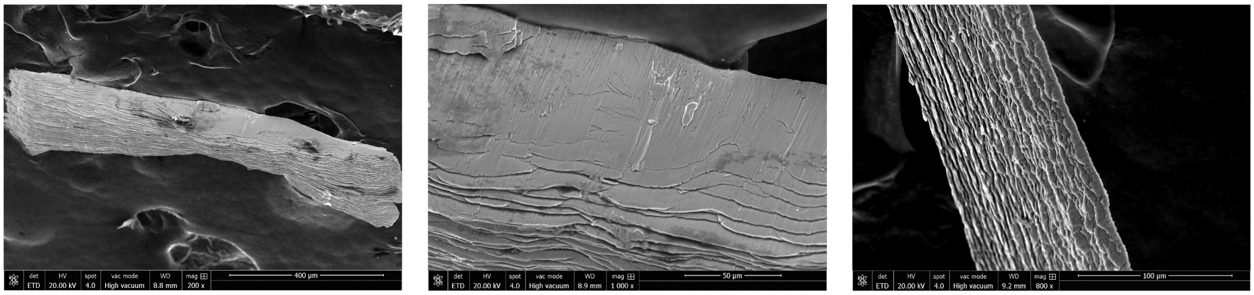

(a) Inconel 718 (b) Inconel 718 (c) Ti-6-4

Figure 4.19. (a) Fracture plane of fibers of Inconel 718 made at 101 Hz showing breaking of the chip before the completion of the cut (b) Higher magnification of the plane showing smooth flat traces characteristic of shear fracture (c) Ti-6-4 fibers made at 101 Hz, showing shear fracture but at the very end of cutting.

In continuous cutting of alloys exhibiting segmented chip formation, the width of each saw-tooth on a chip depends on the cracking frequency, which is often in the order of 10,000 Hz, resulting in a tooth width of a few hundred micrometers [2] for common machining speeds. Since the modulation frequency is much lower than the cracking frequency, multiple teeth may be formed during each cutting cycle, which can further fracture and generate more than one particle per modulation cycle. Thus, chip length in materials demonstrating serrated chip formation is strongly affected by the length of a saw-tooth in addition to the length of the tool path in each modulation cycle. This may introduce an error in the prediction of particle size and shape, and in the calculation of cutting ratio in table 4.1. Thus, simulation of chip formation in modulation-based cutting techniques incorporating chip fracture due to the cyclic crack formation will be helpful in the prediction of particle morphologies with better accuracy for the alloys exhibiting saw-tooth chip formation.

4.7 Summary

Cutting conditions in modulation-assisted machining can be readily manipulated to produce metal particulates of various morphologies. The size and shape of the uncut volume of material that forms each fiber were determined by a set of kinematic equations and through modeling the intersection of the tool locus of the current pass and the workpiece surface profile generated by the previous passes. After incorporation of an average cutting ratio value observed over a low frequency regime, these predictions could estimate the final deformed dimensions with reasonable accuracy but failed to capture the shape change caused by transient deformation mechanisms. Although the fibers were predicted to have a uniform thickness, the changing deformation strain from the start to the end of the cut resulted in a highly irregular shape. The cross-sectional shape of the fibers machined with frequencies spanning over an order of magnitude shared common features such as a smooth rake face and a rough back surface (typical of all free machining chips) and a gradually increasing chip thickness. Cutting started from the thinner end as was proven from the presence of chip curl and the orientation of flow lines. Fibers cut at higher frequencies often exhibited fracture characterized by a flat edge on the end of the cross-section.

With the right choice of lubricants, particles could also be produced from alloys such as Ti-6-4 and Inconel 718 that are traditionally known to present challenges in machining. Elevated cutting temperatures, increased tool wear and very high cutting loads are the common issues faced that arise due to the restricted flow of coolant to the cutting zone. Modulating conditions allow the tool-workpiece contact to be broken periodically, thus, greatly improving lubrication and therefore, the machinability. The change in particle dimensions before and after deformation was lower for harder materials, indicating a lower cutting ratio and lower imposed strain. The cutting ratio was further shown to decrease with increasing modulation frequency. The cross-sectional shape of fibers made from relatively softer alloys (such as Al 6061, Cu) shows the occurrence of chip curl which is absent in those made from the harder alloys (Ti-6-4, Inconel 718). For the latter, a flat end is almost always observed as the edge toward the end of the cut which was shown to be a consequence of shear fracture in the chips before a cutting cycle was completed. The origin of the non-uniform chip thickness, variation of cutting ratio with f_m, and consequent effect on chip hardness and microstructure will be discussed in the next chapter.

5. DEFORMATION

The varying chip thickness observed in the previous chapter suggests that the shear strain of the chip also varies along the length of the cut. Previous observation of lower cutting forces and energy while cutting with modulation led to the hypothesis of incipient chip formation in interrupted cutting techniques. Since the degree of incipient behavior depends on the cutting time/length, a wide range of deformation conditions, from steady-state to incipient can be realized in a chip by controlling the length of cut during each modulation cycle. This chapter describes the effects of these varying deformation conditions on the mechanical properties and the microstructure of chips produced at various modulation frequencies.

5.1 Hardness variation in chips

Shear deformation during cutting strengthens the material removed from the bulk which is evident from the increased hardness of a chip compared to the starting workpiece. This increase in hardness can be directly correlated to the shear strain imposed in the primary deformation zone given in equation 2.1. Since each modulation frequency corresponds to a unique deformation condition, the corresponding strain level in the chips was estimated through the measurement of chip hardness.

5.1.1 Deformation change with modulation frequency

Vickers hardness test was performed on Al 6061 fibers produced from the tube of diameter 25.4 mm, at $f_w = 2$ Hz and f_m of 101-701 Hz. The data is plotted in figure 5.1 as a function of the modulation frequency. One indent was made in the center of a fiber cross-section which measured the average hardness of the fiber. 10 fibers were indented for each frequency and their average is reported along with the standard deviation. Although care was taken to use the lowest load possible and to position the indents exactly in the center, because of the small thickness, it was hard to place the indent sufficiently far (greater than 3 times the indent size according to ASTM E384 and ISO 6507-1 [54]) from the particle edges.

Thus, effects originating from the proximity of indents to the edges could not be prevented in some fibers.

The hardness of the chips produced at 0 Hz or via continuous cutting was 152.5 VHN, which corresponded to a 36 % increase from the workpiece material hardness of 112 VHN. Such increases in chip hardness are commonly observed in conventional cutting operations (∼37% increase in chip hardness has been reported for steady-state cutting of Al 6061 at 5° rake [22]). For $f_m = 51$ Hz, the chip hardness was 30 % higher than the workpiece hardness, while for $f_m = 701$ Hz, the corresponding increase was only 4%. Modulation conditions, therefore, are capable of producing machined chips with minimal strain hardening and consequently, with much lower hardness than that observed in continuous cutting operations. Previous research found that particles formed from Al 6061 cut at 10 Hz and 150 Hz showed a 15 % and 40 % decrease, respectively, in the specific energy dissipation as compared to continuous cutting [15]. As this energy mainly originates from the plastic deformation of the chip, it can be inferred that the particles cut at high f_m were subjected to lower deformation. This is in agreement with the present results, which show a decrease in hardness with increasing modulation frequencies. For a high cutting frequency, the length of cut is very short (small value of R), thus, deformation occurs entirely in the incipient stage before the tool starts to disengage with the workpiece, resulting in a lower hardness.

Prior measurements of shear strain in MAM through the measurement of approximate chip thicknesses, showed a 35% decrease in the strain imposed in chips made at a modulation frequency of 100 Hz than that in chips produced by CC at the same nominal rake angle [25]. Due to the non-uniformity of chip thickness and the curvature in the direction of chip length, such measurements need to be considered with caution. Direct measurement of chip hardness in the present study provides concrete evidence of the reduced levels of strain hardening in chips formed during interrupted cutting techniques and reinforces the body of literature that supports the presence of transient deformation states in MAM.

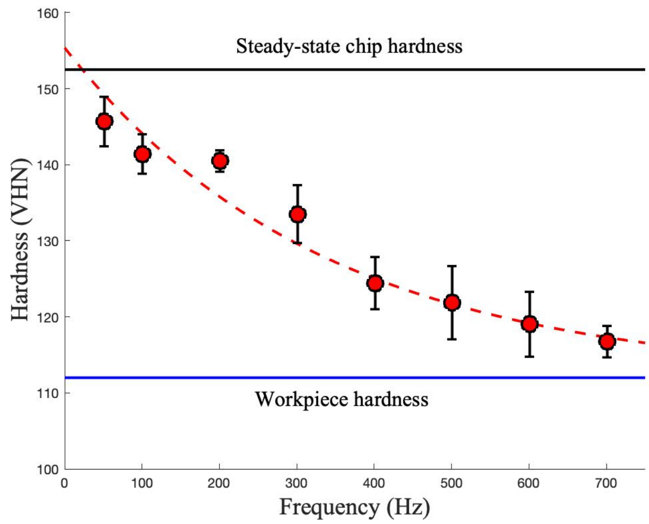

Figure 5.1. Vickers hardness of aluminium fibers vs. modulation frequency showing a gradual decrease with the increase in frequency.

Since the Vickers indents were made approximately at the center of the fiber cross-section and the fiber length is a function of the modulation frequency, the center of a fiber at a specific frequency also denotes a specific length/time after the start of the cut. Thus, the hardness measured from chips made at different frequencies can also be used to map the variation in cutting strain with varying length/time from the start of the cut. The duration of each modulation cycle is $1/f_m$. Therefore, the time of cut at the indent location (center of the fiber cross-section) can be approximated as $\frac{1}{2} \cdot \frac{1}{f_m}$. The hardness data shown in figure 5.1 was plotted against the time of cutting $1/2f_m$ and is shown in figure 5.2.

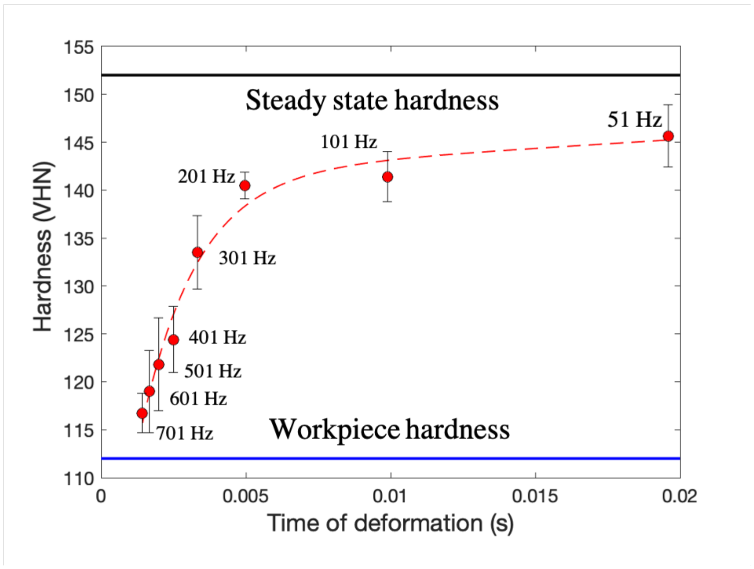

Figure 5.2. Vickers hardness of aluminium fibers plotted as a function of the cutting time (proportional to the cutting distance) showing a gradual increase with time. The hardness becomes asymptotic while approaching the steady state hardness.

A gradual increase in hardness is observed with the increase in cutting time as expected. It is interesting to note that a sharper increase in hardness is observed in the higher frequency regime (701-201 Hz) than that in the lower frequency regime (51- 201 Hz) for the same relative increase in the cutting length. For example, the length of cut for chips made at 301 Hz is double that of 601 Hz which results in a 13% increase in the hardness of the longer chips, however, chips made at 51 Hz are only 3% harder than those made at 101 Hz. This suggests that the variation in the shear strain of cutting along the length of cut is more significant at the very beginning of cutting. As the cutting time progresses, the increase in strain is more gradual until the primary deformation zone is formed and the strain eventually reaches the steady value depending on parameters such as the rake angle, the shear plane orientation, etc. (equation 2.1).

5.1.2 Proposed incipient chip formation mechanisms

The origin of the strain variation lies in the changing deformation mechanisms before a definite shear plane is established. During the first engagement of the tool and the workpiece, deformation is more akin to indentation. The material ahead of the tool face is compressed due to the tool movement into the workpiece. It then builds up against the rake face followed by the removal of a strip of material from the bulk that constitutes a chip. Typically, the length of the removed chip material is larger than the thickness that facilitates bending, causing the chip to curl away from the tool rake face. Curling continues till the energy required to bend the chip further is greater than that to overcome friction at the tool-chip interface [2]. In steady-state cutting, the compression of the material ahead of the tool face gives rise to the formation of a shear plane along which steady-state shear occurs, thereby, forming the primary deformation zone. The steps preceding the formation of the primary shear zone are illustrated in the schematic shown in figure 5.3.

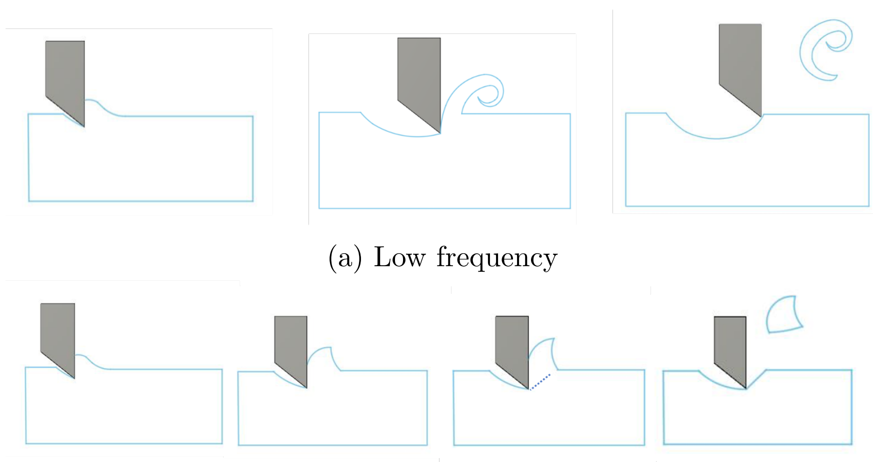

(a) Low frequency

(b) High frequency

Figure 5.3. Stages of incipient deformation before reaching steady-state for (a) low frequency, showing the occurrence of chip curling (b) high frequency, showing the mechanism of chip fracture.

Before the onset of primary shear, the system undergoes deformation but in an incipient phase. During this time, the amount of strain (initially due to indentation and then due to continuous bending) increases with the time of cut (also leading to the increase in cutting forces) before saturating to the value associated with primary shear. If the time of tool-workpiece engagement is shorter than that required for the formation of the primary deformation zone, cutting will always be in an incipient state. Since the length of cut is strongly dependent on the modulation frequency, particles cut at different frequencies are subjected to varying levels of deformation between fully incipient to fully steady-state (corresponding to a zero modulation frequency or continuous cutting). For higher frequencies, due to the higher thickness relative to chip length, bending is suppressed. The strain builds up at the tool chip and may often lead to the initiation of a crack, leading to fracture and consequent removal of the particle. These steps are shown schematically in figure 5.3b. The varying modes of deformation will also impart a varying strain, which is characterized in the next section.

5.1.3 Deformation inhomogeneity within a fiber

Numerous studies have shown the gradual increase in cutting forces with the length of cut [17], [18]. The critical length at which the forces saturate is a function of the workpiece material and the cutting conditions. This section attempts to characterize the change in micro-hardness within each fiber as a function of the cutting length.

Micro-indentation tests were performed to obtain a hardness profile along the particle length (fiber width). Indents are numbered 1 to 6 and spaced evenly with respect to their position along the length of the particle from the start to the end of the cut (figure 5.4b). Since l_c is small for a high f_m, the number of indents that could be made on the cross-sections was lower for higher modulation frequencies. Note that the distance between the indents is relative, i.e., the absolute distance between two consecutive indents was higher for 101 Hz than for 401 Hz. Indents near the start of the particles that were too close to the edge (figure 5.4b left end) were statistically scattered and were not considered due to edge effects. Five fibers were indented for each frequency. The average hardness at each location is plotted with the error bars corresponding to ± one standard deviation of the mean.

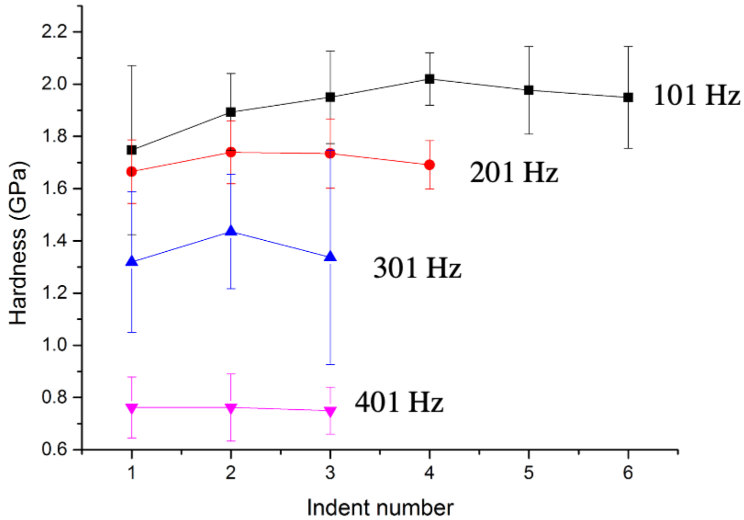

(a)

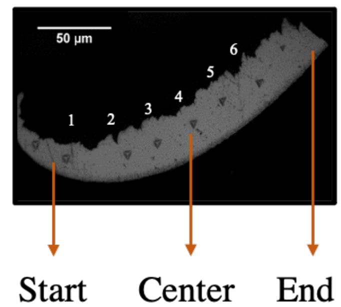

(b)

Figure 5.4. (a) Micro-hardness of Al 6061 chips along the cutting length, for different modulation frequencies (b) Showing the position of the indents along the length of the chip (cut), numbered from the starting end. The first indent positioned at the right end, before 1, is made by the instrument to identify the location of the sample surface.

Figure 5.4a shows that the average hardness decreases with increasing frequency, as was observed in the Vickers hardness results. The spatial variation in hardness showed that the hardness was lower at the start of the particle formation and increased till the center of the fiber. This suggests that the center was more likely to have been deformed under conditions closer to steady-state, leading to higher strains and higher hardness compared to the start of the particle. In a previous study, the strain distribution within a MAM particle was computed through finite-element analysis [28], which showed the effective von Mises strain in the center of a particle to be twice of that near the starting edge. The micro-hardness data validates this previous simulation.

The changing nature of deformation and the variation of rake angle along the cutting length are the phenomena underlying the varying hardness with the length of cut for each MAM particle. Starting with the indentation-like deformation, followed by bending, and lastly, shear along the shear plane, the strain increases, increasing the undeformed chip thickness in the process to a constant value (close to the center of the fiber). Towards the end of the cut, when the tool is about to disengage with the material, the particle remains attached to the workpiece over a very short length. Fracture in chips may occur before the tool completes its path to disengage with the workpiece that led to the straight edge observed on some of the fiber cross-sections shown in section 4.3. This also imposes little to no deformation at the end of the chip which is depicted by the slight drop in the hardness of the region near the end of cutting shown in figure 5.4a. Chips made at higher frequencies (>401 Hz) displayed the presence of shear fracture. Thus, it is likely that a crack was initiated locally, shortly after the tool engaged with the workpiece that led to the fracture of the chip, even though the bulk of the material ahead of the workpiece was strain-hardened only to a small extent, if at all. This explains the relatively constant hardness for 401 Hz, suggesting that the deformation mode may not be reaching the bending stage. These changes in cutting modes cause inhomogeneous strain across the volume of each MAM particle which is evident from the varying local thickness and hardness measured in this study.

5.2 Estimation of strain variation with modulation frequency

Determination of shear strain via chip thickness measurement is tricky even for continuous cutting because of the roughness on the back surface of the chip. Traditionally, the decrease in chip length has been measured through a deep scratch method to evaluate the cutting ratio, and hence, the shear strain [2]. In modulation cutting systems, the tool path inside the workpiece material is different from that measured by free oscillation of the tool due to the material resistance. Instantaneous changes in parameters like f_m, f_w and A will also give rise to uncertainties in determining the precise tool locus inside the material, making it difficult to assess the uncut chip dimensions. The varying thickness in each chip and chip bending also makes it challenging to measure the deformed chip dimensions.

Since the chip hardness can be directly correlated to the shear strain, the strain corresponding to each frequency can be obtained by matching the chip hardness value to a predetermined strain-hardening curve obtained for the same material under plane strain compression-based deformation processing. Plane strain rolling was performed on Al 6061-

T6 plates to generate a (rolling)strain-(plate)hardness calibration curve. Each subsequent rolling pass resulted in an incremental increase in the amount of strain, thus, increasing the plate hardness. Figure 5.5a shows the variation of rolled plate hardness with the effective rolling strain, considering plane strain conditions, as defined in equation 3.2. A quadratic fit was computed to establish a relationship between the above variables. This relationship (calibration curve) estimates the amount the strain imparted during cutting that would result in a certain chip hardness. MAM chip hardness obtained from chips produced at various frequencies was superimposed on the above plot, as shown in figure 5.5b. Points on the calibration curve were identified where the Y coordinate is the hardness value of MAM chips made at a particular frequency. From this point of intersection, a perpendicular is dropped on the X-axis to estimate the corresponding strain.

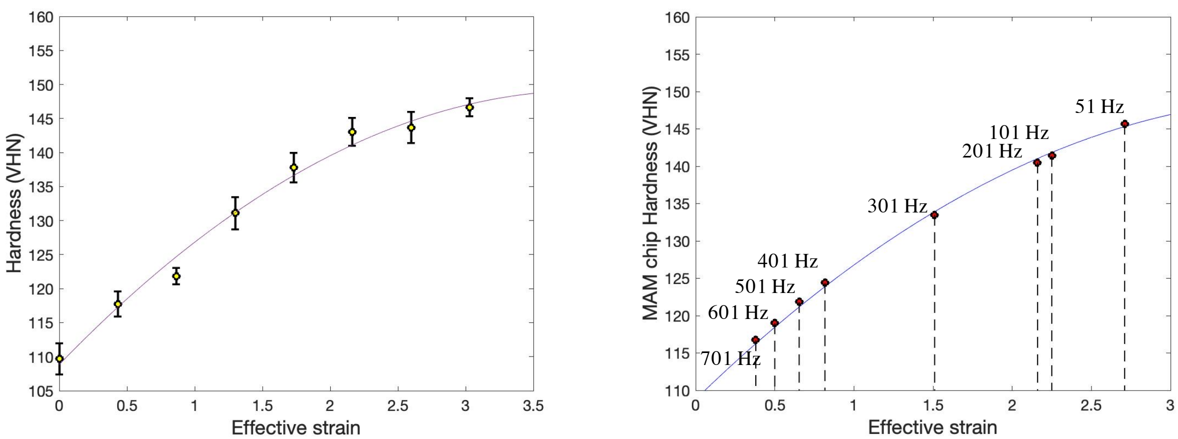

(a) Calibration curve

(b) Strain measured from hardness

Figure 5.5. (a) Increase in the hardness of Al 6061-T6 bar with an increase in rolling strain fitted to obtain a calibration curve (b) Vertical lines dropped from Y-values corresponding to MAM chip hardness for different frequencies (labeled) to estimate the corresponding strain from the hardness-strain relationship derived from (a).

Table 5.1 shows the strain values calculated from the chip hardness for some frequencies, and the corresponding strain variation is plotted in figure 5.6. Previous works in MAM had suggested that the strain in interrupted cutting varies as a function of the processing parameters through the observation of cutting forces. This work is the first successful attempt at measuring the variation of strain by resulting chip hardness quantitatively.

Table 5.1. Measured effective strain for a few modulation frequencies

Modulation frequency (Hz)	Effective strain	Shear strain	Shear strain rate
51	2.7	4.7	480
101	2.2	3.9	790
201	2.1	3.7	1500
301	1.5	2.6	1570
401	0.82	1.4	1130
501	0.65	1.1	1130
601	0.5	0.9	1040
701	0.4	0.6	900

The shear strain and the strain rate was calculated from the measured effective strain as,

$$\gamma = 1.732 \cdot \mathrm{e}_p$$

$$\dot{\gamma} = \gamma \cdot 2 \cdot f_m$$

as, the time period of each modulation cycle was half of $1/f_m$. The calculated shear strain is plotted as a function of the modulation frequency in figure 5.6.

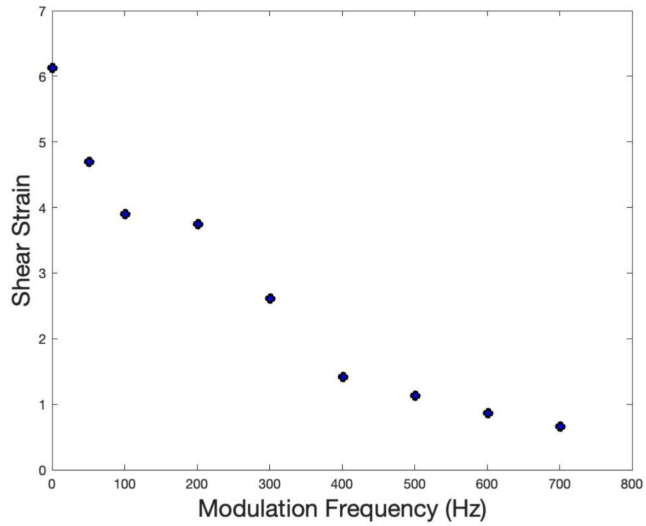

Figure 5.6. Variation of MAM strain with frequency as determined from the strains in rolling.

Yeung had measured an effective strain of 1.45 for f_m/f_w ratio of 150 through finite element analysis ([15]), which matches well with the data (1.5) obtained in the current study for 301 Hz corresponding to the same frequency ratio. It is interesting to note that due to the decreasing strain with increasing modulation frequency (and consequently, decreasing time of deformation in each cutting cycle), there is no systematic variation in the strain rate.

5.3 Transient deformation effects on chip microstructure

Careful sample preparation and etching revealed the flow lines in the chips, marking the deformation path during cutting (figure 4.7). However, the grain structure of these highly deformed chips could not be resolved under the optical microscope. MAM chips are unique because they undergo a transition from incipient nature at the beginning of the cut to steady-state. The cutting parameters also change during the modulation cycle making deformation conditions transient. The deformation mechanisms are different from the steady-state shear observed in continuous cutting; thus, it is expected to cause a variation in the chip microstructure. The microstructure of chips produced at 0 Hz and 101 Hz have been studied by observing the chip cross-section under the TEM. Figures 3.8a and 3.8b show schematically the location on the chip rake face from where the FIB lamellae were lifted out. The location with respect to the chip cross-section is shown in figure 5.7 below. The low surface roughness of the rake side allowed us to mill the trench directly on the fiber surface without any requirement of grinding/polishing.

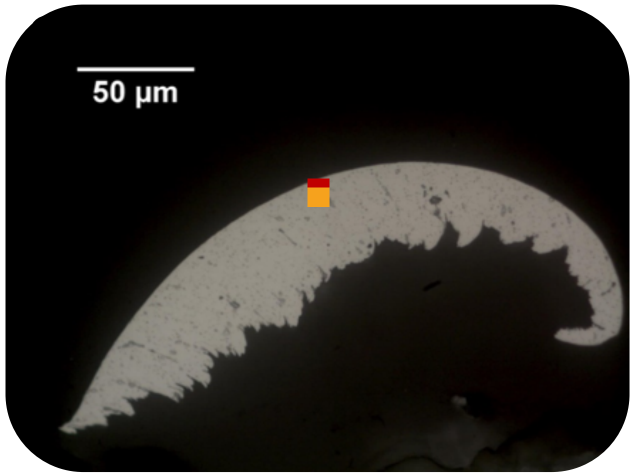

Figure 5.7. Schematically showing the position of the TEM sample that was lifted out using FIB from Al 6061 chip made with (a) continuous cutting (b) MAM at $f_m = 101$ Hz.

The TEM micrographs obtained from the chips are included in figure 3.9b. In both cases, the grains are elongated and oriented toward the chip flow direction. For the chip made with continuous cutting, the boundaries are prominent, while for the MAM chip, a few diffused boundaries are observed, characteristic of lower imposed shear strain.

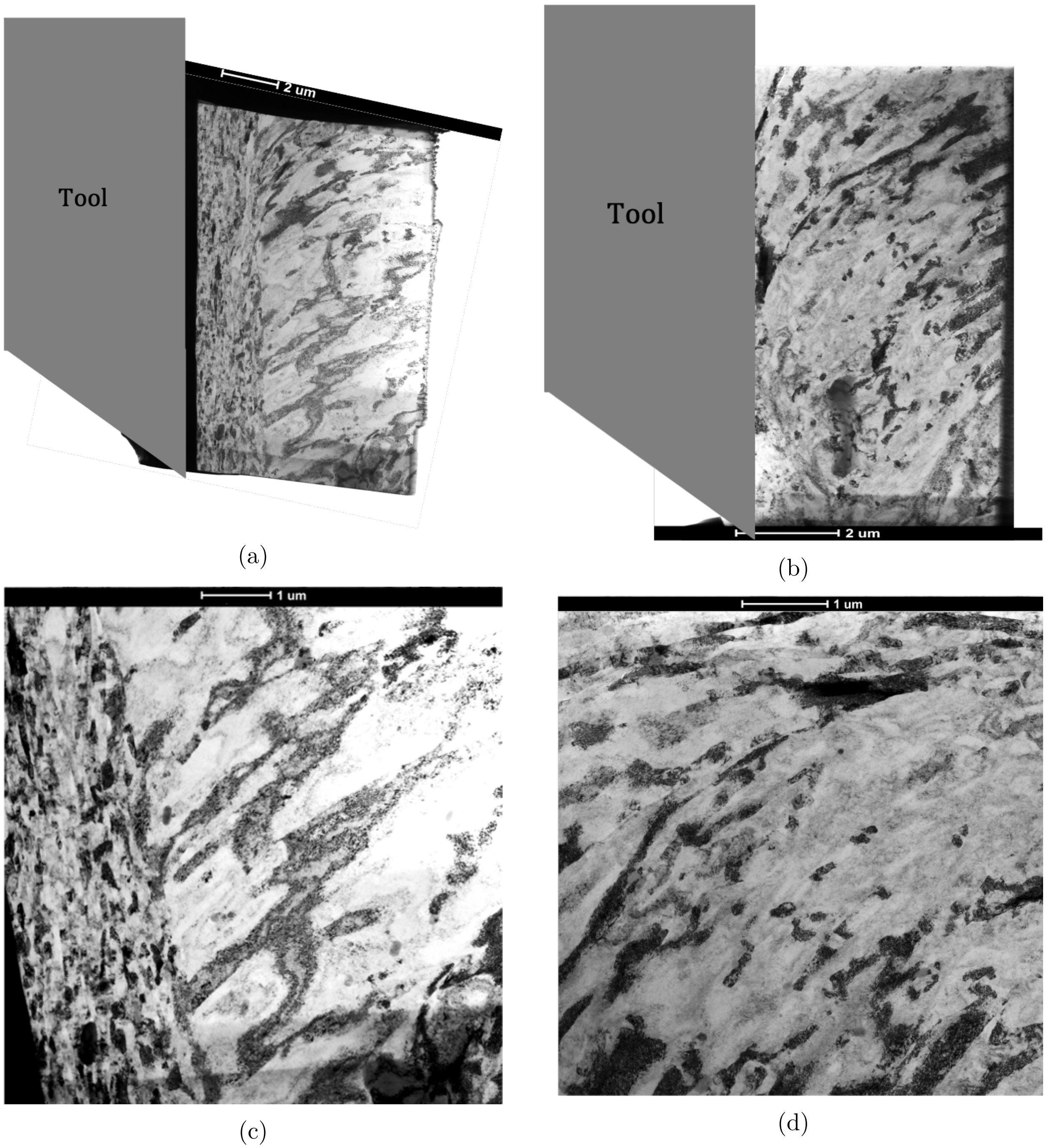

Figure 5.8. Showing the orientation of the TEM micrograph with respect to the position of the tool for (a) CC and (b) MAM. Higher magnification micrographs of (c) CC and (d) MAM chip showing the grain structure.

Figures 5.8a and 5.8b describe the orientation of the microstructure corresponding to the cutting configuration by schematically showing the position of the tool. For the CC chip, there is a pronounced secondary deformation layer. From figure 5.3a, it can be inferred that secondary deformation only occurs after chip bending, when the chip starts to flow freely along the tool rake face. The presence of the secondary deformation layer symbolizes the prevalence of shear as the dominant deformation mechanism. No such secondary deformation layer is observed for the chip made with modulation. During the early stage of cutting, the chip curls away from the tool face and keeps curling till shear flow across the tool face takes over. In MAM, however, shear deformation never starts; instead, the tool begins the retract from the workpiece leading to either the end of the cutting path or, in some instances, chip fracture. Thus, the chip never undergoes sliding across the tool rake face, as has been observed through the absence of secondary deformation layer in figure 5.8d. This microstructural observation is direct evidence that the deformation never reaches a steady state in MAM.

The preferred orientation of the grains was determined using X-ray diffraction. For the workpiece material, the peak corresponding to the (200) set of planes displayed the highest relative intensity while, for the machined chips, (both continuous chip and the MAM chips), the highest intensity was for the (111) set of planes. The workpiece was in tempered condition, thus the predominant grain orientation was the cube texture. Since chips machined with and without modulation both showed the (111) orientation, it suggests that the grains re-orient themselves in the direction of easy slip, soon after the tool-workpiece contact to facilitate the plastic deformation. Significant broadening was observed in the case of chips made by continuous cutting indicating a high amount of 'microstrain' or local misorientations in the lattice. A large microstrain is commonly attributed to the presence of defects in the microstructure, which in turn is a characteristic of large strain deformation.

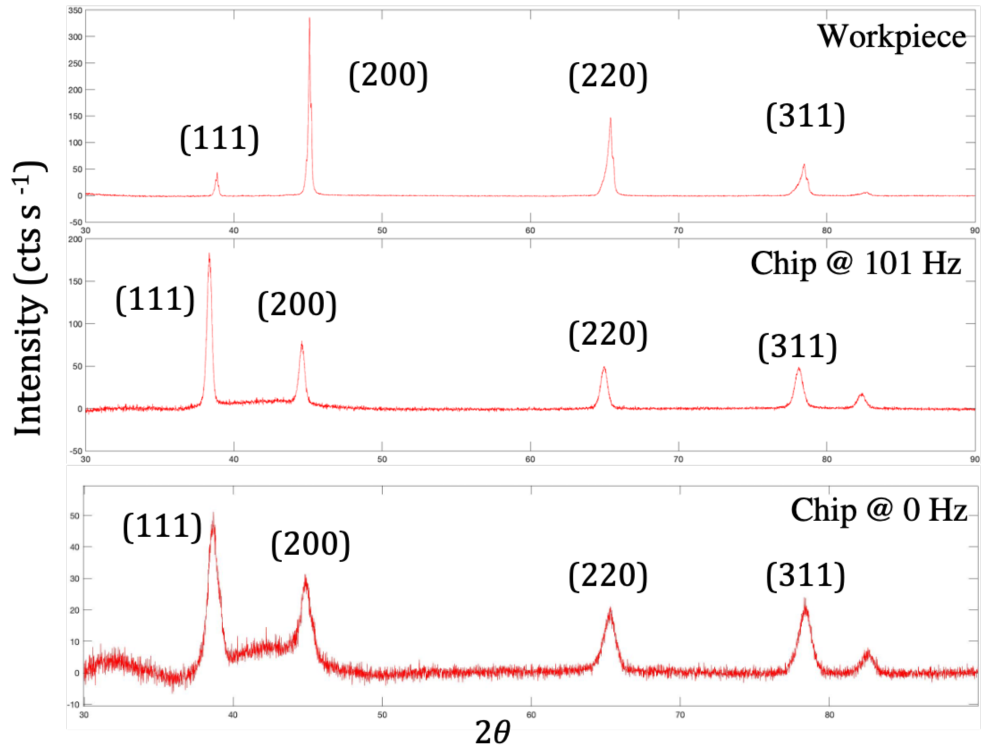

Figure 5.9. Intensity vs. 2 θ plot for the workpiece tube, MAM fibers made at 101 Hz and CC chips showing the change in relative intensities before and after deformation, and the relatively broader peaks in CC compared to MAM

5.4 Effect of modulation on the workpiece surface profile

The surface texture of the workpiece cross-section after cutting with modulation is governed by the modulation parameters. Simulation of the surface profiles was done for various modulation frequencies using equation 2.16 for conditions d = 25.4 mm, f_w = 2 Hz and A = 15 μm. Figure 4.5 showed that the system takes three passes to reach a steady uncut chip shape. The surface profile after passes 3, 4, 5 and 10, obtained for f_m = 101 Hz is shown below in figure 5.10a and the corresponding surface profile observed through optical profilometry in figure 5.10b.

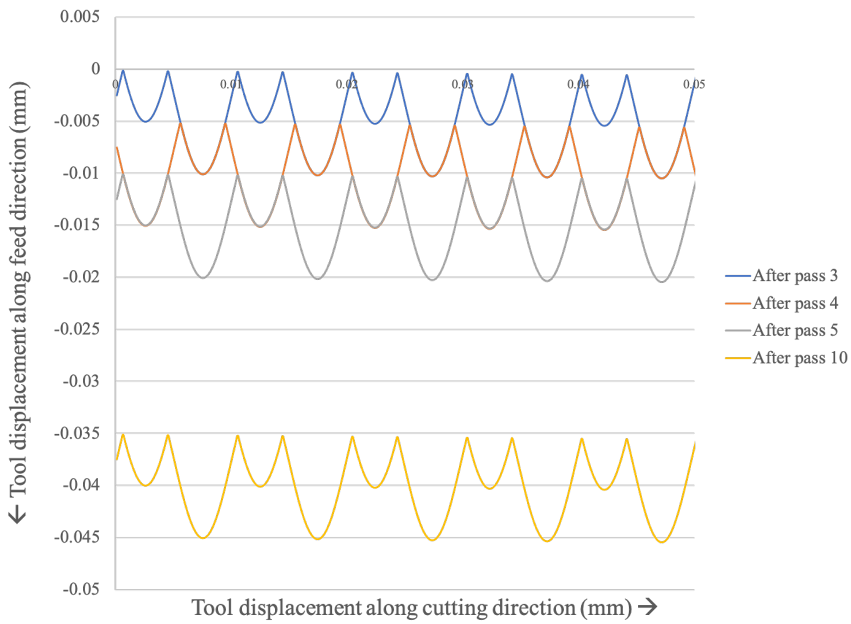

(a)

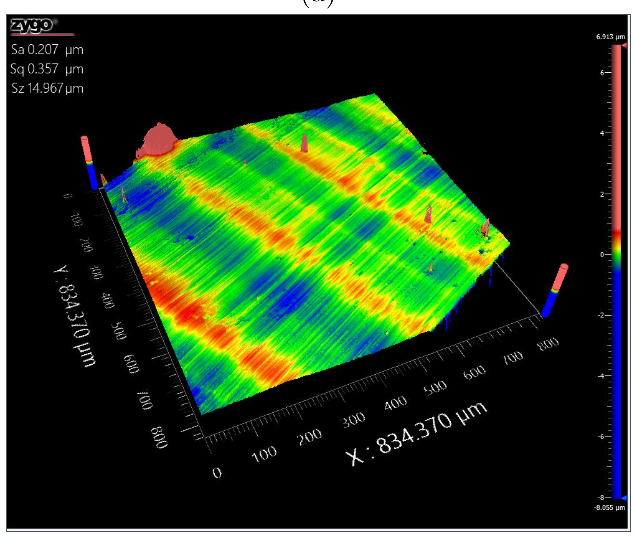

(b)

Figure 5.10. (a) Simulated and (b) experimentally observed workpiece surface after cutting with $f_m = 101$ Hz showing the periodicity of the surface asperities.

The simulated curve shows the periodic nature of the workpiece cross-section surface profile when cutting with MAM. The roughness profile periodicity corresponded to the periodicity of cutting, i.e., the number of peaks in each "period" (marked with blue dotted line) and the length of each period was a function of the modulation frequency. A similar periodicity was also observed in the experiments. Both the simulated and the experimentally observed profiles contained two peaks in each period. The spatial gap between the periods in the simulated and the observed surface was 300 μm and 350 μm respectively. The mismatch likely arises from the incorrect approximation of the tool feed and the instantaneous variations in the process parameters. For intermediate conditions between those leading to discrete chip formation and continuous chip formation, the surface follows a gradual change in the periodicity. Thus, observation of the experimental surface profile can provide an indication of whether the MAM system and the piezo-modulation device can produce the minor changes in frequency required for the experiments performed in section 4.3.2. Similar predictions of the surface profile were made for f_m = 101.4 Hz, 101.6 Hz and 101.8 Hz, and are shown in figure 5.11. The predictions showed that the number of peaks in each period changes with the change in frequency. There are three peaks in each period for 101.4 Hz and four peaks in 101.6 Hz, while for 101.8 Hz, only one peak occurs.

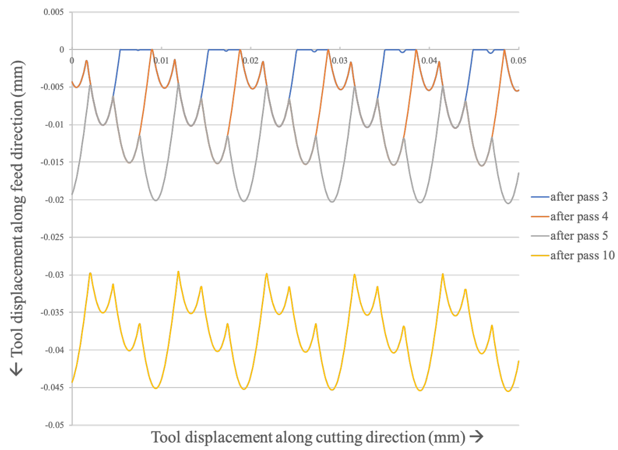

(a) 101.4 Hz

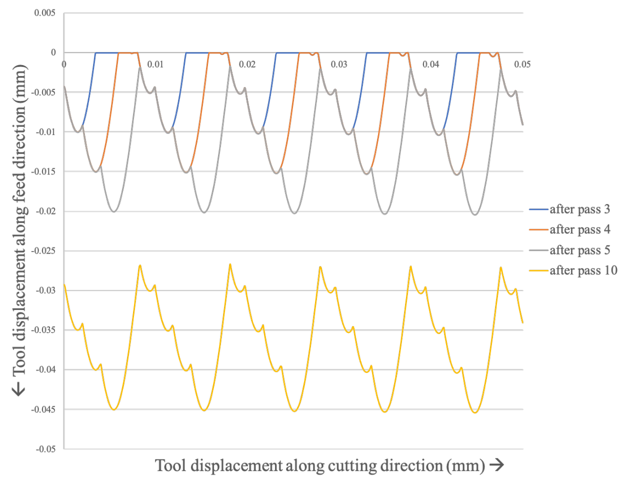

(b) 101.6 Hz

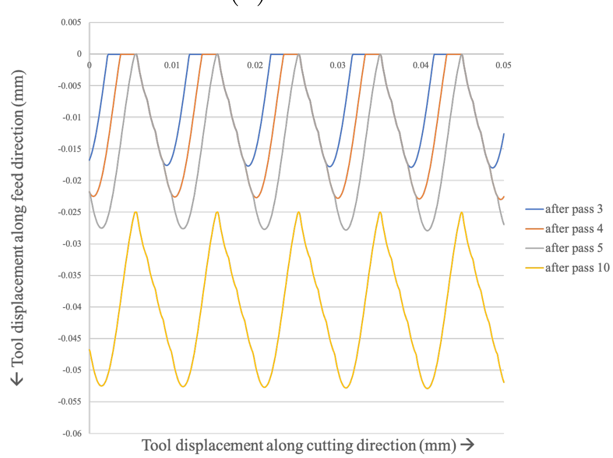

(c) 101.8 Hz

Figure 5.11. Surface profile predictions for offset conditions, showing that the number of peaks in each period (marked with blue dotted lines) change with the change in offset.

Experimentally observed profiles are included in figure 5.12. For f_m = 101.4 Hz and 101.6 Hz, each period has four and three peaks respectively, opposite of what was predicted. The periodicity is also not consistent with some regions showing three peaks for 101.4 Hz and four peaks for 101.6 Hz. The observed profile for 101.8 Hz, however, matches well with the prediction.

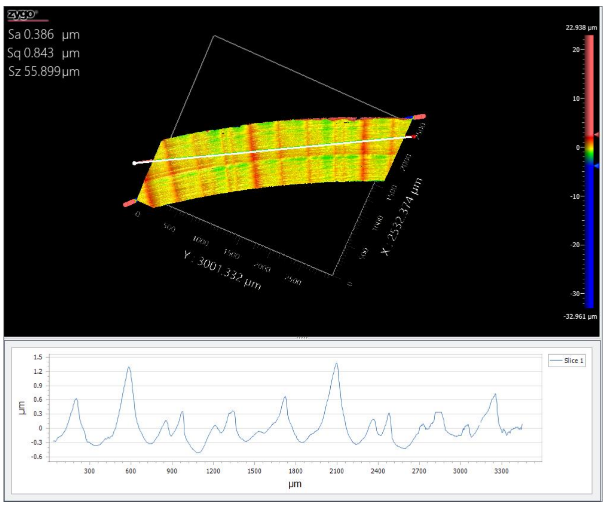

(a) 101.4 Hz

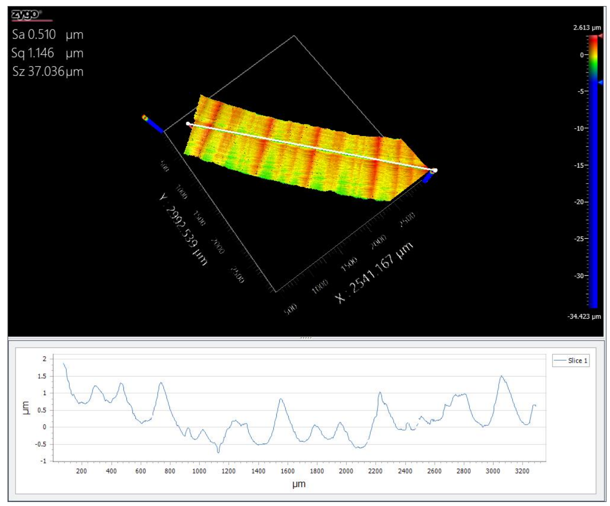

(b) 101.6 Hz

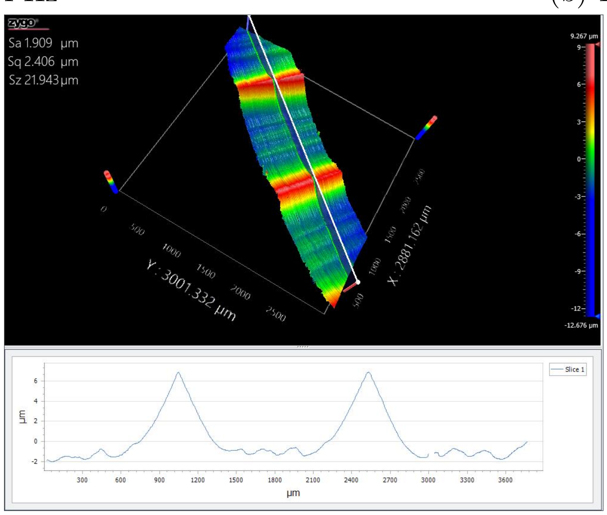

(c) 101.8 Hz

Figure 5.12. Surface profile for offset frequencies showing a non-uniform periodicity.

It is possible that instantaneous variations of ± 0.2 Hz occur in the MAM system response, leading to these variations in periodicity. Since the uncut chip shape for a specific modulation condition can also be affected by these changes, it is difficult to compare the undeformed and deformed chip shapes in MAM. Linear orthogonal cutting or 2-D machining was performed on a special specimen designed to interrupt cutting at regular intervals. Such a system produced a fixed uncut geometry allowing comparison between the deformed and undeformed chip shapes. These experiments are described in the next chapter.

5.5 Summary

Strain hardening in chips made with modulation is lower than in those made by continuous cutting which results in a comparatively lower increase in MAM chip hardness from the workpiece hardness than for CC chips. The hardness of chips decreases with increasing modulation frequency. A larger modulation frequency implies a lower length of cut, thus, chip hardness decreases with decreasing length/time of cut. Microindentation tests on chips suggest an increasing hardness along each chip length from the start till the end of the cut, suggesting a gradual increase in the imposed strain as the cutting progresses. This is consistent with the increasing chip thickness to a nearly steady thickness at the center. The preferred orientation of the grains in both CC and MAM chips was (111) as opposed to (200) of the aged workpiece. This suggests that grain re-orientation occurs almost instantaneously after the tool is engaged with the workpiece. Microstructures of chips made without modulation show the presence of a secondary shear zone consisting of fine grains oriented parallel to the chip flow direction. This layer is absent in the fiber made at $f_m = 101$ Hz. Secondary shear occurs only after the primary shear zone has been established, the chip has reached the steady-state thickness and it flows along the tool rake face. The absence of the secondary deformation layer indicates that the chip was ejected before the onset of shear as the predominant deformation mode.

6. STUDY OF INCIPIENT CUTTING USING LINEAR SLIDE

The morphology of particles (chips) made by machining is a function of the uncut chip geometry caused by tool motion inside the workpiece and the deformation during cutting. To investigate the effect of incipient deformation conditions prevalent in periodic cutting systems on the final shape of a chip without the uncertainty in the uncut chip geometry (mentioned in section 5.4) a new set of experiments was designed with a linear slide and a grooved Al 6061-T6 rectangular sample, and has been described in this chapter. The same machine was also used to perform a simple linear orthogonal cutting in a plain Al 6061-T6 bar to study the initial stages of chip formation.

6.1 Simulation of interrupted cutting

A plane strain (2D) cutting system was employed (figure 6.2). Gaps were machined on a 5X40X240 mm Al 6061-T6 rectangular sample, leaving pillar-like regions of short length to simulate discontinuous cutting. The experiment involves a simple and known undeformed geometry and thus, any change in the dimension/shape of the deformed chips can be attributed to shear deformation alone. Pillars of height 650 μm and width 350 μm were machined on top of the bar using electro-discharge machining (figure 6.1). The workpiece moves with a velocity V relative to a tool with rake angle 0° set at a depth of cut h_0 (undeformed chip thickness). Cutting was interrupted each time the tool traveled across the gap between two adjacent pillars.

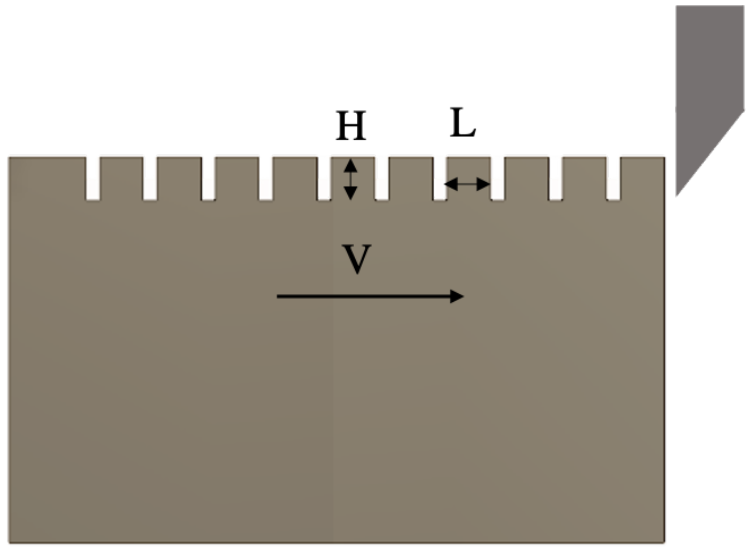

Figure 6.1. Schematic of the sample used for linear orthogonal cutting showing the height, width and spacing of the pillars machined with EDM.

The cutting apparatus was Tormach PCNC 770 equipped with a piezoelectric dynamometer (Kistler 9254, natural frequency $\sim$ 2 kHz. The aluminum bar was clamped to a workpiece holder and constrained behind a glass plate, preventing material side flow. The workpiece holder was programmed to move against a fixed-wedge tool (Mo-Max M42 high-speed steel) with 0° rake at a constant speed of 2 mm/s; see figure 6.2. A high-speed CMOS camera, pco.dimax, coupled to an optical microscope (Nikon Optiphot), was used to image the cutting process in situ, at a frame rate of 500 frames/s. The imaging configuration provided a spatial resolution of 1.4 μm per pixel and recording areas as large as 1296×1296 pixels. The cutting region was illuminated by a 120-W halogen lamp. Post-processing of the images was done using a particle image velocimetry (PIV)-based image-correlation algorithm to obtain a quantitative record of the displacement. Early applications of PIV were to analyze fluid flow by tracking the relative motion of particles in a fluid [55], [56]. Asperities on a material surface serve as the markers and the relative displacement of these "points" in a series of images captured during cutting, can provide an estimation of the displacement and strain fields. Such quantitative measurement of deformation field in machining has been demonstrated earlier by Lee [57], [58].

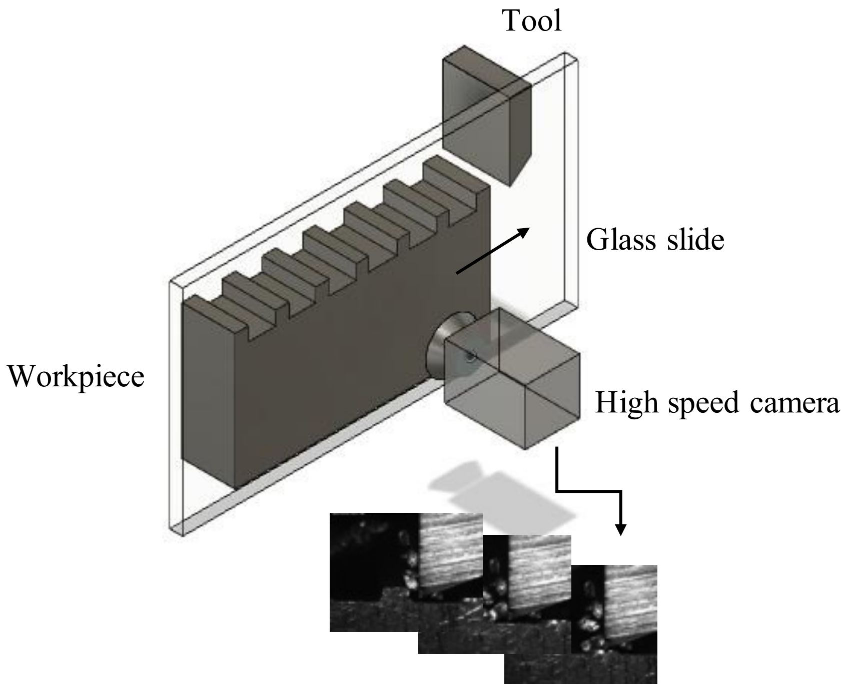

Figure 6.2. Schematic of the set up showing the cutting machine and the high-speed camera.

Early experiments were performed with pillar dimensions, H = 0.5 mm and L = 0.5 mm and 1 mm, as defined in figure 6.1. Cutting was performed with a depth of cut of 400 μm and 2 mm/s velocity. Snapshots of the process are included in figure 6.3a. Although, the experiment was successful in disrupting the tool-chip contact periodically, it is apparent that the chips formed from the individual pillars were not effectively removed from the cutting zone, but deposited in the space between two pillars. When the tool traveled through these gaps, these chips were locked between the tool and the next pillar, and were cut for a second time resulting in two separate fragments. Thus, an undeformed volume of material removed from each pillar resulted in two different chips, with different strain levels. A lower DOC of 100 μm was proposed to achieve better chip evacuation, but that led to severe bending in the pillars after coming in contact with the tool and only one of the corners could be machined (figure 6.3c).

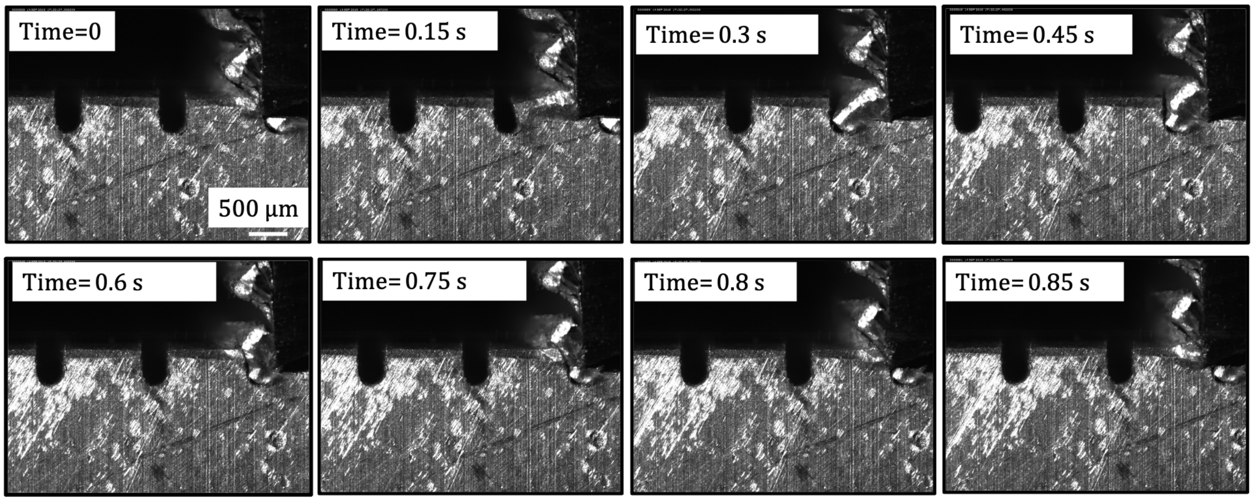

(a) Snapshots of the cutting process with L = 1 mm, H = 1 mm, DOC = 400 μm, showing chips trapped between two pillars and undergoing a second cutting.

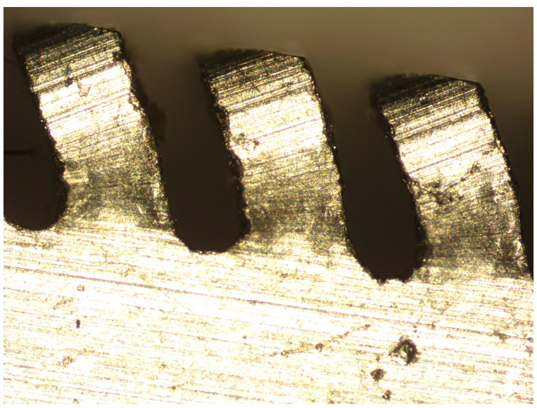

(b) Bent pillars for L = 0.5 mm, H = 1 mm, DOC = 100 μm

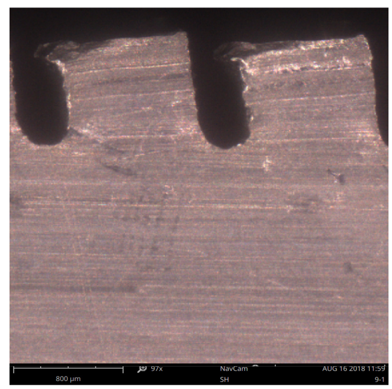

(c) Bent pillars for L = 1 mm, H = 1 mm, DOC = 100 μm

Figure 6.3. Early experimental results showing inconsistent deformation due to poor chip evacuation and severe bending in the pillars.

A couple of modifications in the sample design followed, i.e., a large gap was left between two pillars, and the pillar height was reduced to 350 μm to enable more efficient removal of chips after each pillar was machined. The modified sample performed better although the deformation of the pillars was somewhat affected by the chip produced from the previous pillar. In this experiment, a chip removed from a pillar traveled along with the tool through the length of the gap but was promptly ejected after coming in contact with the subsequent pillar. This contact did not cause any significant damage to the pillars as can be observed from figure 6.4.

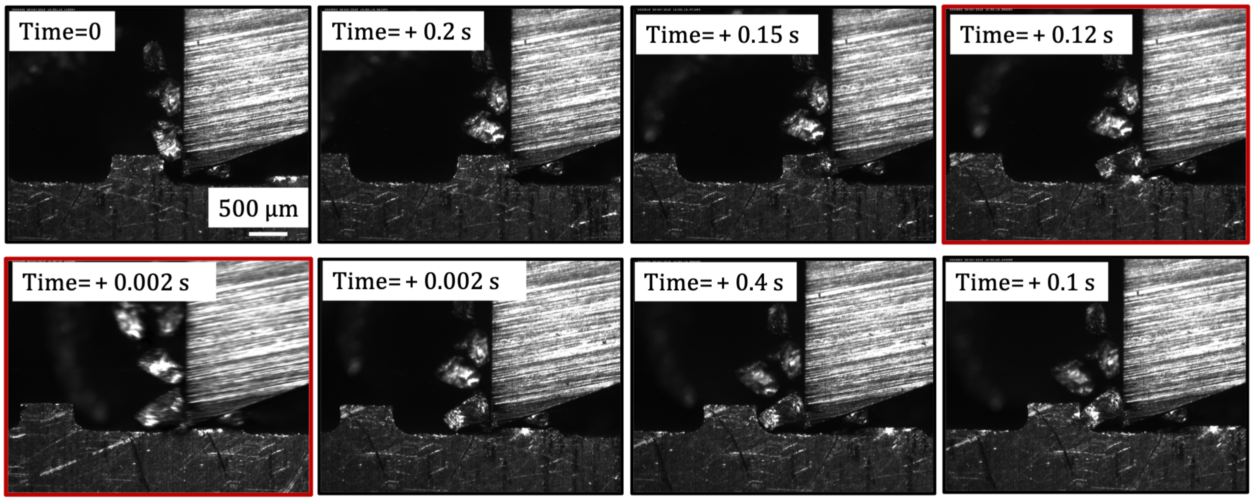

Figure 6.4. Snapshots of the cutting process with L = 650 μm, H = 350 μm, DOC = 200 μm showing chips travelling with the tool before removal from the cutting zone and the fracture in pillars before the completion of the cut.

A major inference from these experiments was that the pillars fractured before the cutting was completed, i.e, before the tool traveled through the entire length of each pillar. The fracture of a pillar has been shown through the very short time interval over which the chip is detached; the relevant figures are marked with a red outline in figure 6.4.

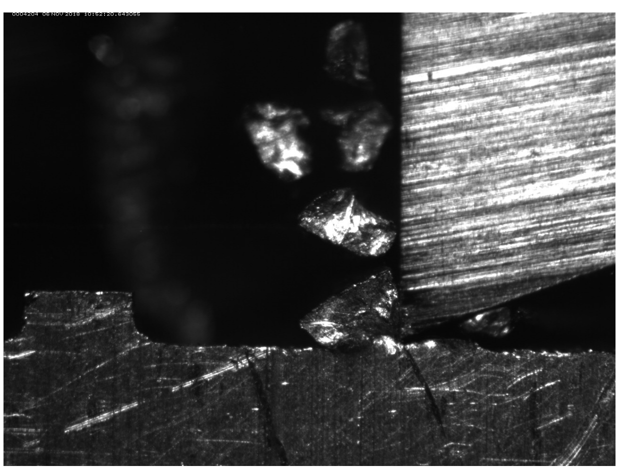

(a)

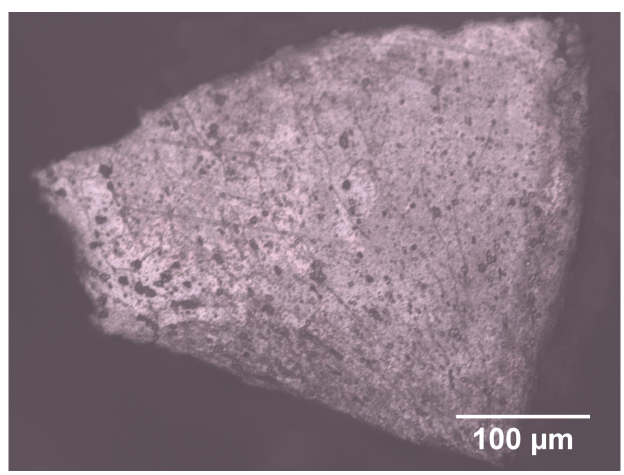

(b)

Figure 6.5. (a) Snapshot of a chip from the in-situ images showing chip bending (b) Chip microstructure showing flow lines due to bending at the pillar base.

It is interesting to note that even though the uncut chip thickness was constant, the deformed chip geometry is rather non-uniform. Bending was the initial mode of deformation, as supported by the in-situ images and the arc-shaped flow lines in the chip microstructure, which was followed by chip fracture. Thus, the steady-state shear flow never occurred during this short period of cutting.

A similar experiment was performed on a Ti-6Al-4V bar of 3.1 mm thickness and 25.4 mm width. The pillar height and length were 500 μm each and the DOC was 200 μm. The snapshots obtained during the test are given in figure 6.6.

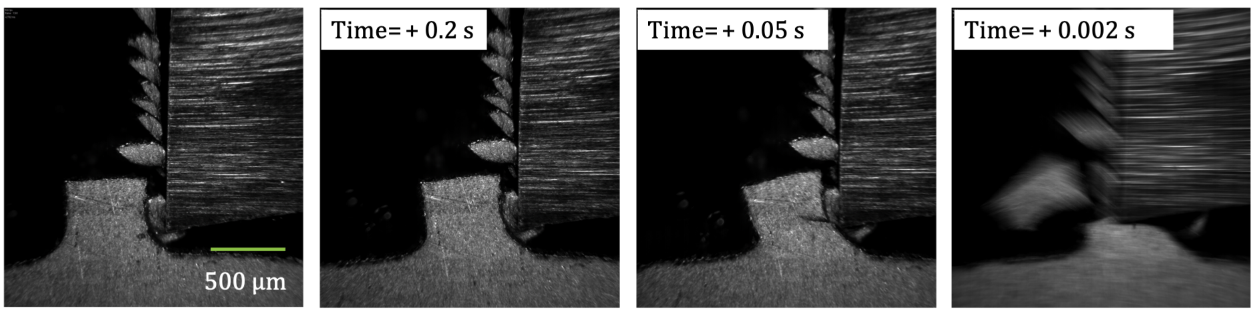

Figure 6.6. Snapshots of the cutting process with Ti-6-4 showing that the pillars undergo minimal bending before fracturing.

Chips removed from a pillar also traveled with the tool as was observed in the case of Al 6061. But, titanium being a heavier metal, the chips did not evacuate from the cutting zone upon contact with the next pillar. Instead, they remained on the workpiece surface, essentially forming the cutting edge for the subsequent pillar. Thus, the chip shape and the microstructure could not be reliably connected to the uncut geometry and the deformation of cutting.

However, some conclusions can be still be drawn from the experiment. The extent of bending in the pillars was lower than in Al 6061, and that is expected as Ti-6-4 is a harder material. Pillars also exhibited sudden fracture along a nearly horizontal plane coinciding with the end of the cutting edge. Particle image velocimetry was used to quantify the strain field in the first pillar that was machined and deformed by the cutting tool only (as opposed to the other pillars which came in contact and were thereby, deformed, by the chip removed from the previous pillar).

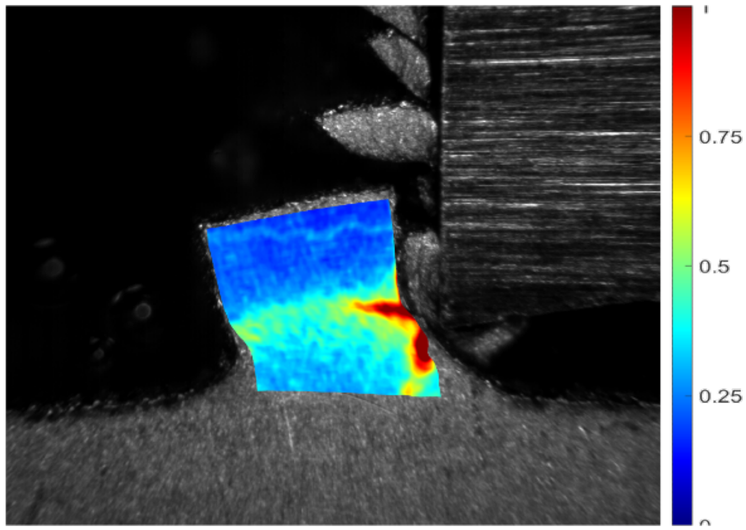

Figure 6.7. PIV calculation of strain in the first pillar showing regions of concentrated strain corresponding to the point of crack initiation.

A strain of high magnitude was concentrated at the tool-pillar contact suggesting that the crack nucleated from the tool tip. The remaining volume of material was subjected to very low strains (blue regions). The volume of material removed as a chip in MAM under high frequencies, can take the aspect ratio, similar to the pillars machined for these linear interrupted cutting tests. Such a hypothetical case is shown schematically in figure 6.8.

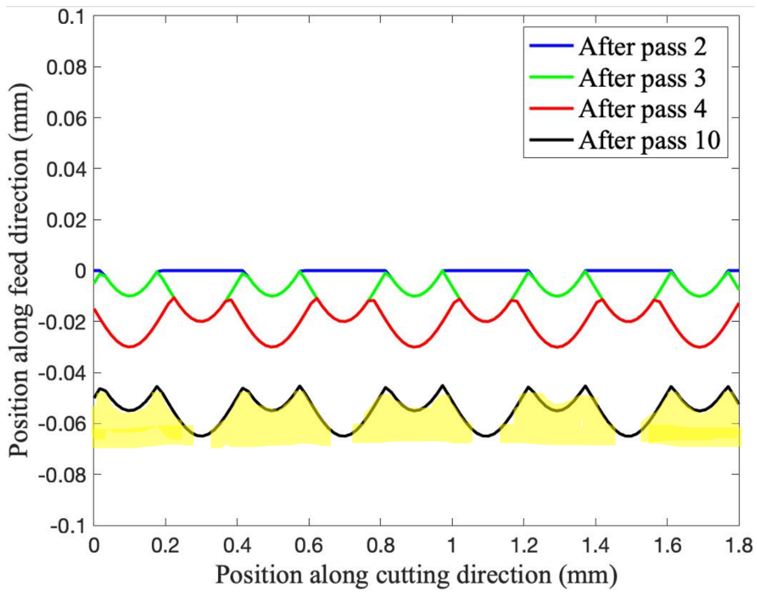

Figure 6.8. Schematic of uncut chip volume for 401 Hz showing that the pockets of material that are removed during each cycle, are similar to the pillars in the linear cutting experiments.

Similar to the pillars, each uncut material of a chip in MAM, could also be undergoing fracture, through the nucleation and propagation of cracks from the tool tip, while the bulk of the material remains undeformed. This causes the chips to have a lower hardness, lower change in the dimension from the undeformed values and flat edges, as was observed in the case of Ti-6-4 and Inconel 718 fibers, and for Al 6061 fibers made at high frequencies.

6.2 Critical length of cut for steady-state chip formation in orthogonal cutting

Linear orthogonal cutting was also performed on an aluminum 6061 bar (without any pillars machined on it) to observe the change from incipient to steady-state cutting. A strip was cut with a 0° rake tool and the hardness of the chip was tracked from the start of the cut till the chip thickness was uniform, indicating steady-state cutting. To make the cutting conditions similar to that of high-speed turning, the highest possible cutting velocity of 30 mm/s was used.

The hardness of fibers was plotted against the time of cut in figure 5.2. An exponential fit was computed for the above set of data and extrapolated to the continuous chip hardness to obtain an approximate time of cut (half of the inverse of frequency) required that would produce steady-state conditions, which was found to be $\sim$ 200 ms. This is also consistent with the time period over which the forces were seen to saturate in the studies made by Yeung [15], shown in figure 2.12. Thus, after a length of $30 \times 0.220 = 660\ \mu m$, cutting was expected to be under steady conditions. Measured hardness values from the chip are plotted as a function of the distance from the start of cut in figure 6.9.

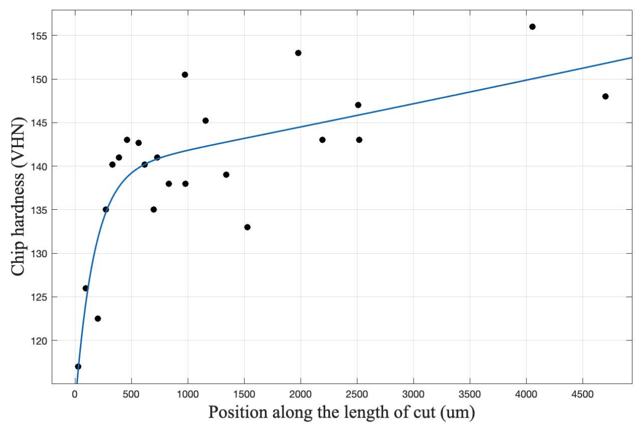

Figure 6.9. Vickers hardness of a chip produced by linear orthogonal cutting, plotted as a function of the distance from the starting edge. Hardness is seen to increase sharply till around 500 μm.

A steep increase in hardness is observed till a cutting length of around 500 μm. The nature of the curve is similar to the plot showing the increase in chip hardness vs. time of cutting in MAM (see figure 5.2). All the chips made for this thesis were shorter than 300 μm, suggesting that they were all subjected to the incipient modes of deformation. Similar studies made in 99% pure lead showed that the critical length for steady-state cutting was around 2 mm [17]. Therefore, this critical length is a strong function of the workpiece material.

6.3 Summary

Experiments of interrupted cutting in 2-D machining provided the advantage of cutting, and therefore, deforming a known undeformed geometry of the workpiece material to enable better comparison of deformed and undeformed chip shapes. Also, the linear cutting setup, being connected to a high-speed camera, allowed us to observe the process in situ. Bending followed by fracture was the common mode of deformation of the pillars during cutting. The fracture occurred before the tool traveled across the full length of a pillar suggesting that premature fracture can be also be occurring in other periodic cutting methods such as MAM. Harder materials like Ti-6-4 undergo minimal bending and are more prone to fracture. This observation is consistent with the observation of the fracture end of MAM fibers made from the high-strength alloys.

7. APPLICATION OF MAM FOR METAL PARTICULATE PRODUCTION

Powder processing is the preferred mode of production of many complex metal parts and is widely used in additive manufacturing and for producing coatings, porous structures and parts with complex geometries. In a majority of these applications, the production of the powder feed is the costliest or one of the most technically challenging steps in the manufacturing process. This is because of the high cost and low yield (due to a large particle size distribution of each batch of powders produced) of the commercial powder production processes. The discrete chip formation in MAM allows the use of this technique as a novel metal particulate production process capable of producing particles of various morphologies (equiaxed, elongated, flat platelet, etc.) with an extremely narrow size distribution. Since all the particulates are machined from the same workpiece, there is no composition/density variation between particles. This chapter describes some of the aspects of using MAM as a powder processing technique.

7.1 Commercial processes of powder production

Atomization is the most common method of metal powder production. The process utilizes a molten pool of metal which is injected into a chamber through a nozzle while a media (most commonly, jet of gasses like nitrogen and argon, sometimes water) is introduced into the chamber through another inlet. When the molten metal is released from the nozzle, the sudden decrease in pressure and the turbulent flow of gasses break the stream into droplets which eventually solidify as individual powders. Although the process has key advantages like a very large throughput, powders formed in each batch are often irregular, inhomogeneous with regard to composition and density, and have a large particle size distribution [59]. A large number of satellite particles is also encountered that deteriorate the powder flowability [60]. Other processes of powder production such as electrolysis also produce a large size distribution [61], [62]. Metal powders used for applications like additive manufacturing are required to meet stringent conditions for shape, size, PSD and density

[20], [63]. Thus, a large volume of powders from each batch is rejected as either oversize/undersize resulting in loss of material, waste of energy, and lower efficiency of the production process.

7.2 Particle size distribution in MAM

Particles produced through MAM are unique because of the uniformity in their shape and size. Each chip particle is machined under identical conditions, thereby producing similar dimensions with only minor differences due to the instantaneous process instabilities and inhomogeneous deformation. The average particle length produced for frequencies 50-999 Hz was shown in figure 2.19. This data, which was obtained from an automatic size analyzer, Morphologi, from a batch of >500 particles, was also analyzed with Jmp software to study the particle size (length) distribution (PSD). PSD of fibers produced at 101 Hz, 120 RPM, from a 25.4 mm diameter tube is shown in figure 7.1.

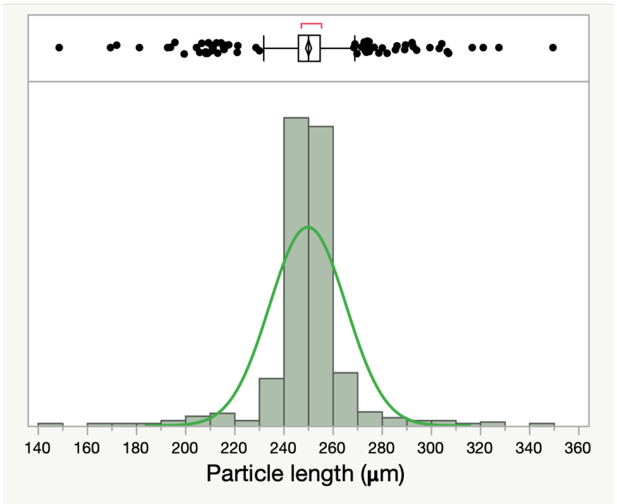

(a) Histogram for 101 Hz

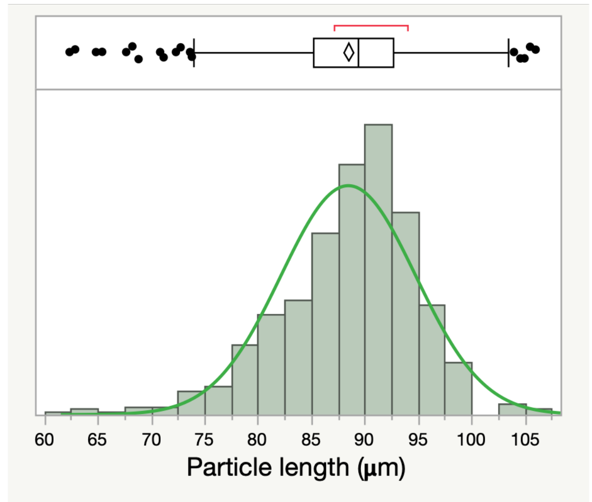

(b) Histogram for 401 Hz

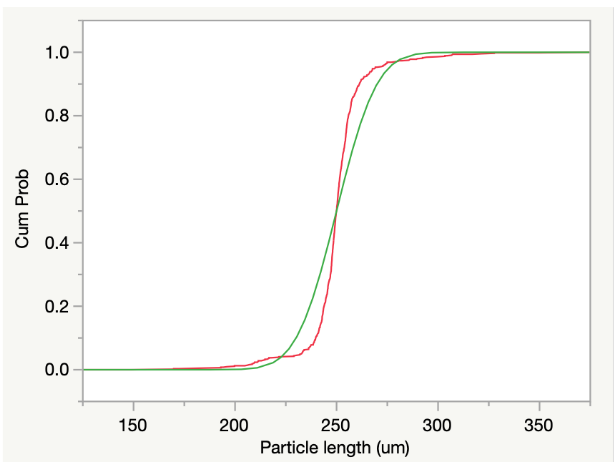

(c) Cumulative frequency plot for 101 Hz

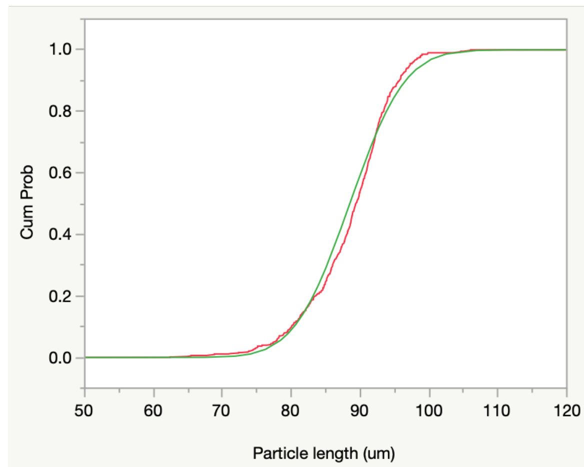

(d) Cumulative frequency plot for 401 Hz

Figure 7.1. Particle length distribution of fibers produced at f_m = (a) 101 Hz and (b) 401 Hz respectively, with a normal distribution curve superimposed on the histogram and the corresponding cumulative distribution is shown in (c) and (d) respectively.

A normal distribution was fitted to the histogram as shown by the smooth curve and the box plot is included at the top. The boundaries of the box correspond to the upper and lower quartile value of the distribution and the points lying beyond the bars are classified as outliers. The cumulative density plot for the data (red) and the fitted normal curve (green) are included in figures 7.1c and 7.1d.

The particle size range was within 100 μm and within 50 μm for most cases and the standard deviation of the mean was between 10 μm to 25 μm. The error measurement is likely due to the curved nature of the fibers that make them rest in different orientations leading to different projected chip lengths. Manual measurements of fiber length through optical microscopy and image analysis produced standard deviations of as low as 5 *mum* suggesting that the distribution is tighter than what was measured through the Morphologi instrument. For particles made at frequencies lower than 401 Hz, the median value coincides with the mean suggesting that length is uniformly distributed. This is also evident from the nearly same amount of outliers in both directions of the median. However, for smaller particles, the percentage of outliers on the larger length side is considerably greater than on the lower length side. This is due to the "rewelding" action of the fibers at smaller length scales. Due to the elevated temperatures of cutting, discrete particles are sometimes welded after formation leading to a doublet or sometimes an array of joined fibers. These anomalous cases are shown in figure 7.2.

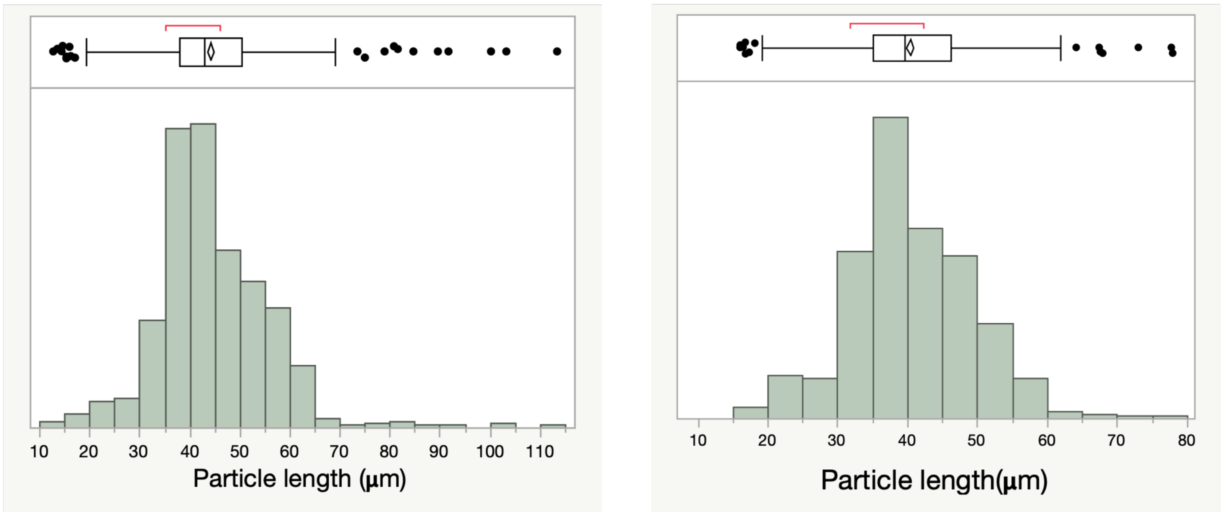

(a) Histogram for 801 Hz (b) Histogram for 901 Hz

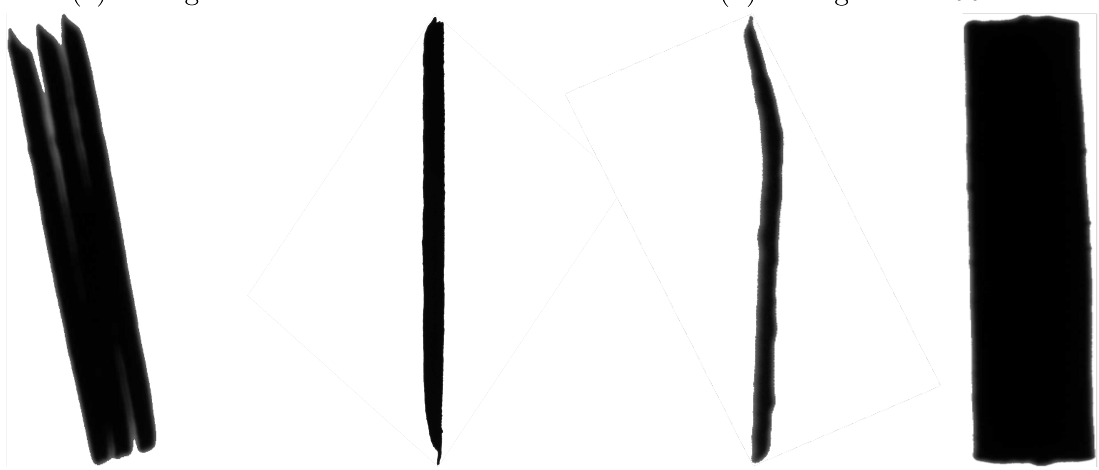

(c) Welded fibers (d) Two fibers joined (e) A single curved fiber (f) Single straight fiber

Figure 7.2. (a) Particle size distribution for chips produced at (a) 801 Hz (b) 901 Hz showing the relatively greater number of outliers with larger lengths. Reconstruction of particles shown in (c), (d) and (e) will produce errors in measurement, while, (f) will provide a more correct value.

The system identifies a group of joined fibers as a single particle which incorporates an error in the measured length. Although it is possible to apply filters such as the largest and smallest length (the lower limit eliminates measurements from dust particles) that will be considered as a separate particle, variable orientations in which a particle rests on the sample plate gives rise to variable projected lengths, often close to the actual length of a single discrete fiber, making it difficult to eliminate. Curvature in the fibers (figure 7.2e) can also be a cause of an error in the measurement, as the projected length of the particle will be greater than the actual length. However, a correction factor can be utilized in the instrument software after which the particles are identified as fibers, and instrument measures the actual length (figure 7.3).

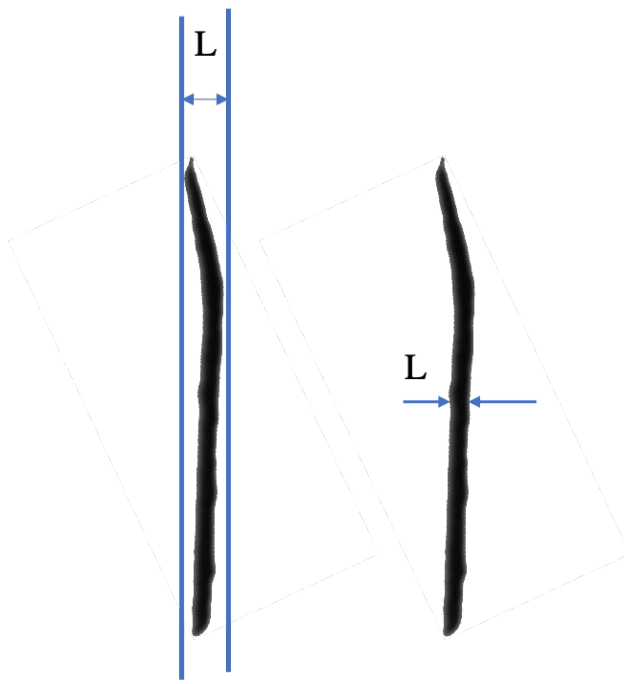

Figure 7.3. Length of a fiber measured by the software without fiber correction (left) and with fiber correction (right).

7.3 Particle size limits

It is now well established that MAM can produce particles of controllable shapes and sizes. It was worthwhile to study the process operational boundaries and determine the limits of the particle sizes that can be produced through MAM. Experiments were performed over a wide range of parameters; f_w = 10-120 RPM, f_m = 51-999 Hz, and a feed rate of 1-15 $\mu m/rev$. The highest modulation frequency and the lowest rotational frequency were identified that would produce discrete particles. These values constituted the working limits of the lab-scale setup and the smallest cross-section of particles that could be produced. The highest modulation frequency that the MAM device could produce was 1000 Hz. The parameters that produced the smallest fiber cross-section were 40 RPM, 1 $\mu m/rev$ and 999.67 Hz, which corresponded to roughly 20 μm particle length and 15 μm particle thickness. The cross-section of these fibers is shown in figure 7.4a and 7.4b. Below 40 RPM, the system was unstable, producing a mixture of discrete and continuous chips. Several chips were welded at the edges to produce an array of lightly attached fibers. It may be possible to remove this limitation through better lubrication, and it is a matter of further study.

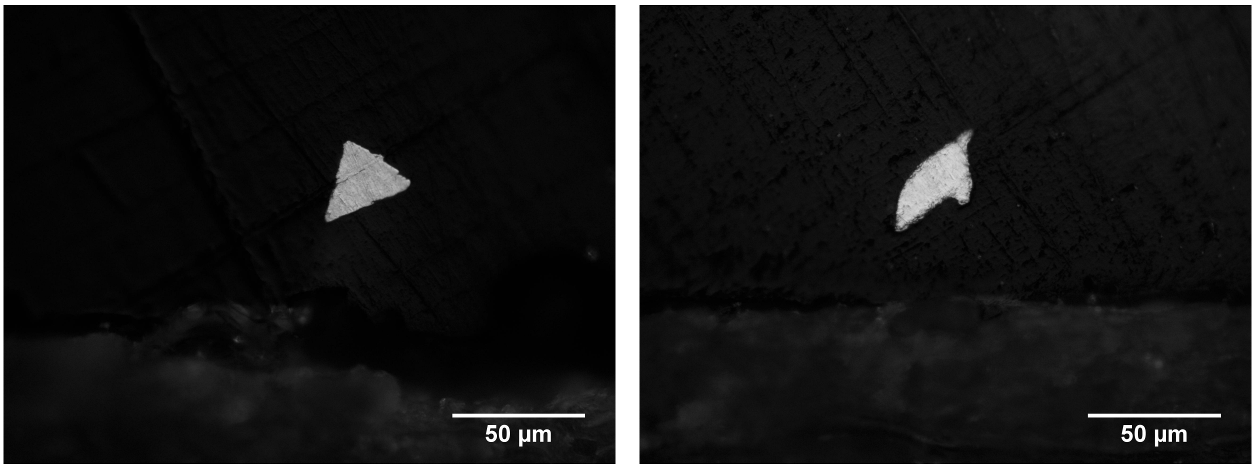

(a) 999 Hz, 60 RPM (b) 999 Hz, 60 RPM

Figure 7.4. Cross-section of particles produced at conditions to achieve the smallest length.

7.4 Energy efficiency

The high cost of powder metallurgy parts can be primarily attributed to the high cost of powders. Powder production via atomization requires a large amount of energy as it involves heating the metal to its melting temperature. A simple comparison of the energy required in atomization for different metals can be estimated by calculating the energy required to heat the metal to its melting point and the latent heat. In contrast, for powder production via machining (assuming continuous machining leading to an equal weight of chips), the energy required is the specific energy of cutting. Although the specific energy varies with cutting parameters like chip (particle) thickness, it is largely dependent on the material. Some representative values of u are tabulated for a few common alloys.

Table 7.1. Specific energy of cutting for a few engineering alloys [2]

Material	**Specific cutting energy,** J/m^3
Aluminum	7×10^8
Free machining brass	10.5×10^8
Titanium alloys	35.1×10^8
Mild steel	21.1×10^8
Superalloys	49.1×10^8

Thus, the energy of atomization, u_a, can be expressed as,

$$u_a = C_p(T_m - RT) + H_L \tag{7.1}$$

Where, C_p, T_m and H_L are the specific heat, melting temperature and latent heat of melting of the metal, and RT is the room temperature. A comparison of u_a and u is shown in figure 7.5.

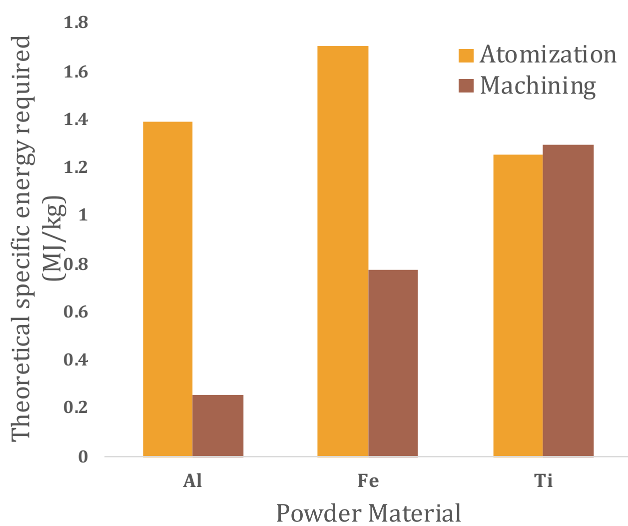

Figure 7.5. Theoretical energy required to produce 1 kg of powder from atomization and machining for three common metals.

For aluminum and iron alloys, particle production via machining can produce significant energy savings compared to atomization. But, for titanium and similar high strength metals, due to the inherent low machinability of such materials, the energy required for machining is higher. However, it is important to note that the value of U used for comparing the two processes, obtained from table 7.1, is for continuous cutting. It has been shown that the energy dissipated in continuous cutting is much higher than that for cutting with modulation. The strain in MAM is reduced nearly five times (figure 5.6) suggesting that the specific energy in MAM can also be significantly lower. Since the particle size depends on the modulation frequency, which in turn determines the degree of incipient behavior, the energy of particle production with MAM is not a constant value but is dependent on the required particle dimensions. The conditions leading to higher cutting energies, such as insufficient fluid penetration, high friction at the tool-chip interface, high cutting forces are also much less severe in MAM. Thus, metal particulate production via machining may potentially require lower energy than atomization, even in the case of high-strength metals.

7.5 Production rate

For any process to be economically viable, an important property is its throughput or production rate. Modulation assisted machining unlike many other commercial processes can produce only one particle at a time and thus, have a very low volumetric production rate. The rate is related to the volume of material removed per second, and thus, can be expressed in terms of the process parameters as,

$$V_{\text{prod}} = \pi d f_w s_o (DOC) \tag{7.2}$$

Note that, modulation frequency does not affect the production rate as the volume removed in each rotation of the workpiece is constant, only the number of particles that will be produced from that volume depends on the modulation frequency. Calculated production rates for producing equiaxed particles ($DOC \sim s_o \sim \frac{\pi d f_w}{f_m}$) is shown in figure 7.6. The rate increases with the increase in workpiece diameter and RPM, following equation 7.2 above.

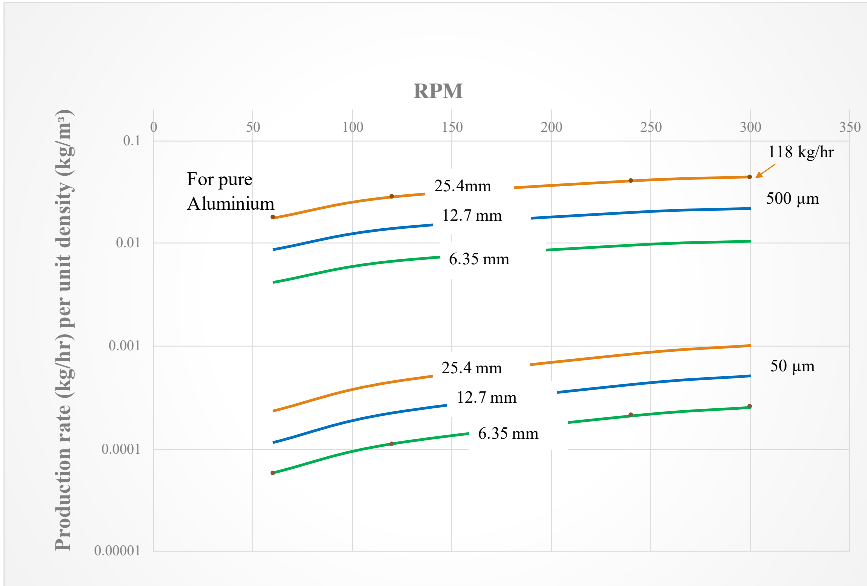

Figure 7.6. Production rate of equiaxed particles with MAM showing that the rate is dependent on d, RPM and the required particle size.

An interesting aspect of particle production with MAM is that the production rate is a function of the desired particle size. Although the particle length can be controlled by modulation frequency, without affecting the production rate, to produce smaller equiaxed particles, we also need a smaller DOC and tool feed rate, thereby, lowering the production rate. A possible way to improve the rate is by increasing the number of cutting edges or by incorporating a multi-point tool. If k is the number of cutting edges, in each rotation of the workpiece the volume of material removed is increased by k times. However, this also requires careful control of processing parameters, as, the conditions of discrete chip formation will change with a change in the number and the relative position of the cutting edges.

7.6 Design and performance of metal fiber-reinforced epoxy composite

The addition of fillers can greatly influence polymer properties such as strength, conductivity, color, and wear resistance [64]. Metal fibers have been utilised as fillers for making polymer-based composites to improve ductility [65], rigidity [66]–[68] and electrical conductivity [69]–[71]. Addition of a small percentage ($< 10\%$ of aluminum particles of size < 50 μm) to glass-fiber-reinforced composites have been shown to improve its mechanical properties [72] and decrease the frictional coefficient in dry sliding, thereby, improving the wear resistance [73]. The most commonly studied mechanical property is the modulus as this property depends primarily on the geometry, particle size distribution and the concentration of the filler. By contrast, the tensile strength of a reinforced polymer is more difficult to characterize because it depends on the unknown local polymer-fiber interactions, along with the above factors [66]. Thus, for this study, the elastic modulus of epoxy was compared with that of a fiber-reinforced polymer (FRP) sample, made of epoxy filled with MAM fibers.

7.6.1 Sample preparation and test methodology

Tensile testing was performed in an MTS test frame on dog-bone shaped specimens. The sample preparation steps are illustrated in figure 7.7. A mold was specially designed to cast epoxy in the dog-bone shape. The dimensions were chosen in accordance with sample V of ASTM D638-14-Standard test methods for tensile properties of plastics. The mold was machined out of a Teflon bar. The lubricating nature of the Teflon surface ensured that the epoxy sample does not stick with the mold.

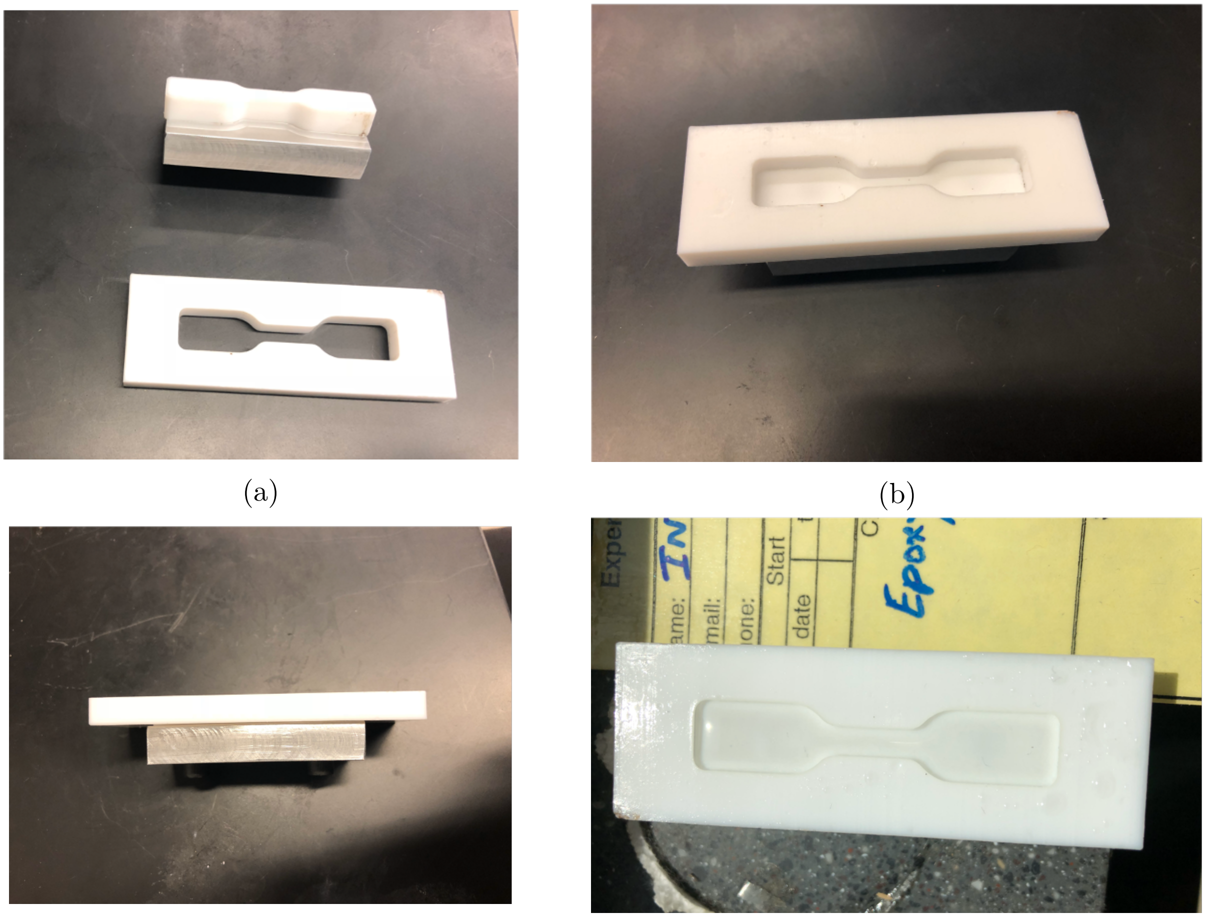

(a) (b) (c) (d)

Figure 7.7. Preparation of a tensile test sample using the custom mold.

Two components of the mold are shown in figure 7.7a. The bottom part is a tensile test sample machined out of the Teflon bar that is attached to a steel base. The top part, also made of Teflon slides over the bottom part to create a slot/mold for casting the liquid polymer (figure 7.7b). Samples of variable thicknesses can be produced by adjusting the position of the top part with respect to the steel base. Liquid epoxy resin and hardener were mixed in the Flaktrek rotary mixer and was poured into the slot. Once the mixture cured, the bottom component was pushed upward (such that there is no gap between the top part and the steel base; (see figure 7.7c) to push the sample out of the mold. A sample cast in the mold is shown in figure 7.7d.

Al 6061-T6 and Ti-6-4 fibers made with MAM at 101 Hz, 120 RPM were used as fillers to reinforce epoxy. Fibers were randomly packed into the sample slot shown in figure 7.7b.

Liquid epoxy resin and hardener mixture was poured over them to bind all the fibers into one composite sample. With a known weight of fibers and epoxy forming each sample, the volume percentage of fillers was calculated to be 20 % for Al 6061-T6.

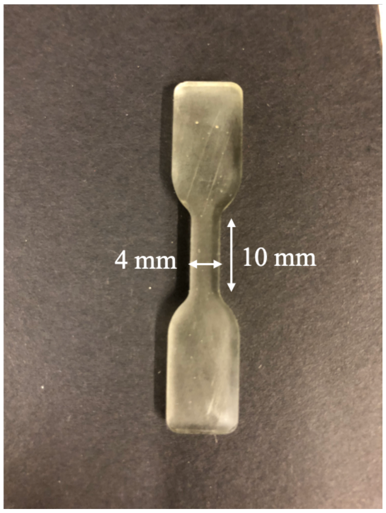

(a) epoxy

(b) Al 6061-fiber reinforced epoxy

Figure 7.8. Tensile test samples of (a) pure epoxy showing the dimensions (b) a fractured composite sample.

7.6.2 Test results and failure analysis

Tensile tests were performed for three samples of neat epoxy and FRP. The engineering stress-strain plot for one of the samples of epoxy and FRP each is shown in figure 7.9. The average modulus measured was 1.04 GPa for epoxy and 1.43 GPa for FRP. Significant grip slippage occurred during the testing of neat epoxy leading to the extremely high strain to fracture. Although the ductility of epoxy resins has a wide range from 2% to 20 % [74]–[76] due to the variation in curing conditions, samples in our experiments failed at strains of around 35% indicating grip slippage to be present.

Incorporation of aluminum fillers in epoxy led to a 40% increase in the rigidity of the polymer. Addition of Ti-6-4 fibers produced a 90% increase in the modulus (average modulus of FRP was 1.98 GPa). Therefore, production of fillers for reinforcing polymers can be a promising application for short fibers made from modulation-assisted machining.

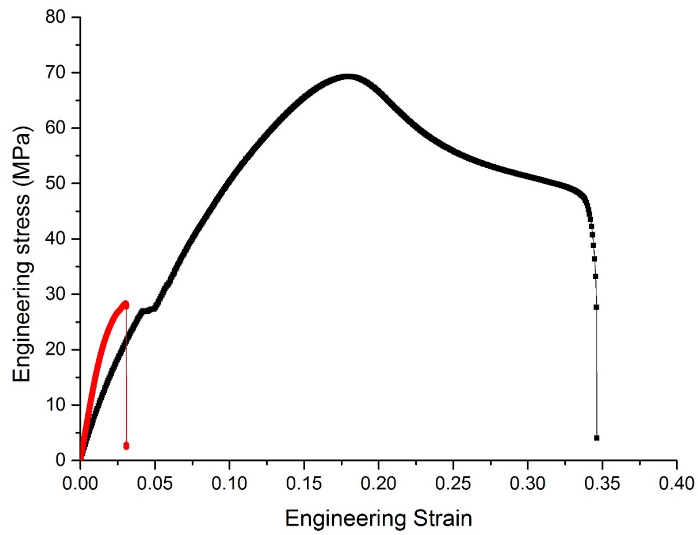

Figure 7.9. Engineering stress-strain plot for epoxy and epoxy filled with aluminium fibers. An improvement in the modulus is observed by the use of particle reinforcement.

The fracture surface of the tensile test specimens was examined to understand the failure modes. In a previous study by Cantwell and Roulin-Moloney [77], three distinct zones were identified on the fracture surfaces of epoxy that failed in tension. Near the crack initiation point, a semi-circular, smooth, featureless zone was formed, called the "mirror zone", which corresponds to the region of sub-critical crack growth [78]. It was followed by a region with geometrical surface features caused by the interaction of the primary crack and the secondary cracks that originated in the regions of high stress near the primary crack [79]. The third zone was formed due to the overlap of these parabolic features leading to three-dimensional features and thus, a rough surface. These features can also be observed on the fracture surface of epoxy specimens tested in this study. Figure 7.10a shows a crack that originated from an air bubble surrounded by a smooth, flat surface region akin to the mirror zone (figure 7.10b).

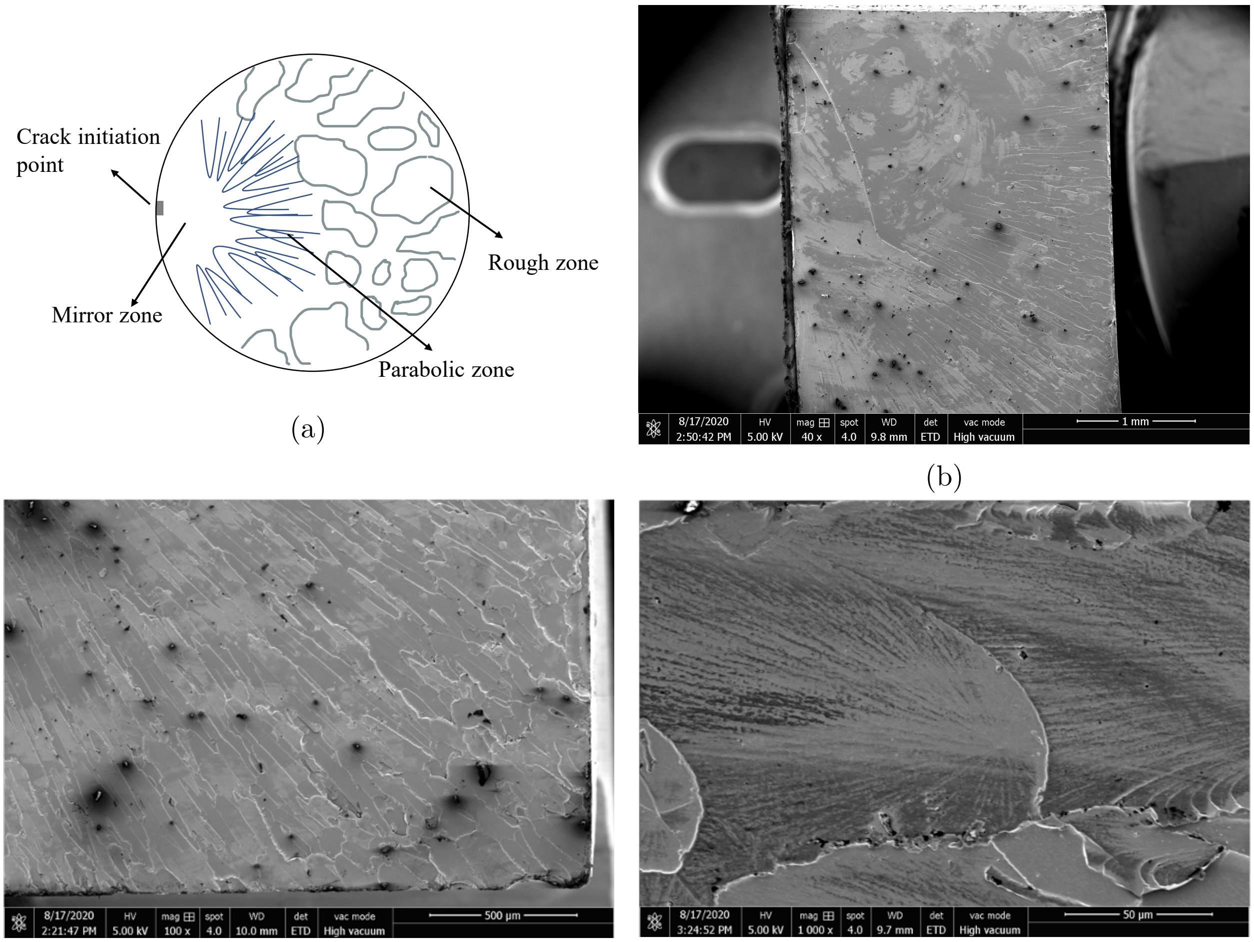

(c) (d)

Figure 7.10. (a) Schematic of fracture modes in epoxy showing the smooth mirror zone, the parabolic zone and the rough zone, adapted from [77] (b) Fracture surface of a neat epoxy sample showing the initiation of a crack at an air bubble (c) parabolic surface features on the fracture surface (c) and (d) higher magnification of the parabolic features.

Parabolic crack fronts are also observed farther from the crack initiation point, indicating the intersection of two crack fronts. Secondary cracks are formed in the vicinity of the primary crack and micro-cracks can be observed throughout the area of the sample (figure 7.11.) The parabolic shape arises from the difference in the velocities of the primary and secondary cracks. A higher primary crack velocity leads to the parabolic crack front while similar velocities lead to an elliptical crack front [79]–[81].

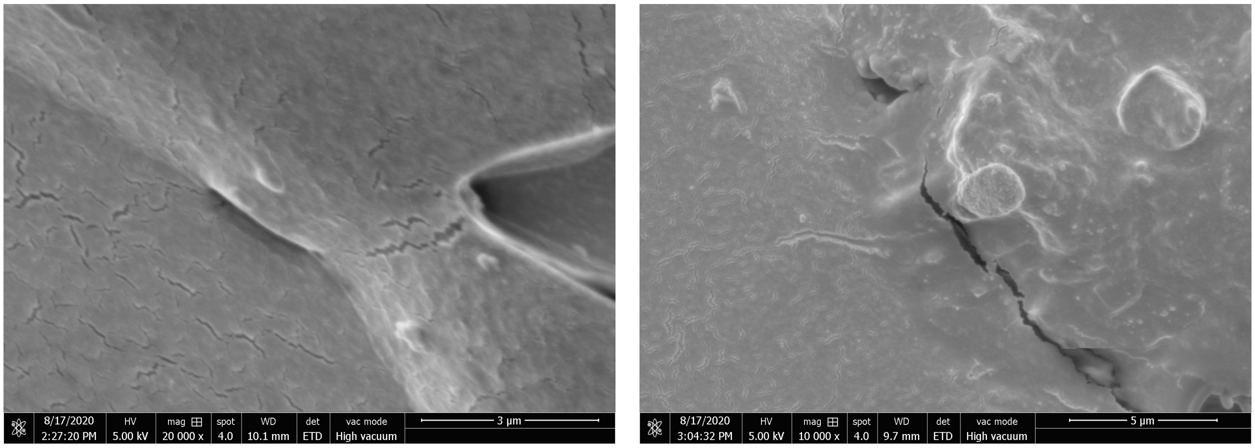

(a)

(b)

Figure 7.11. Fracture surface of an epoxy specimen showing (a) secondary crack growth near a primary crack (b) microcracks in the sample volume.

The fracture surface of FRP specimens shown in figure 7.12a illustrates that fiber debonding was the primary mode of failure. Fiber pull-out is one of the most commonly observed mechanisms of fracture observed in fiber-reinforced composites and occurs when the interface between the fibers and the matrix is weaker than the matrix and the fiber material [82]–[85]. The fibers that were pulled out from the matrix, leave behind a hole as shown in figure 7.12b. Notice the difference in surface texture on both sides of the hole corresponding to the rake face and the back face of the chip. It has been found that fibers with greater surface roughness carry greater loads due to better frictional transfer of load from the matrix [86]–[88]. The higher surface roughness of the machined back surface should ideally provide significant load sharing. However, in the current experiments, due to the sample preparation method, a few air bubbles were trapped between the matrix and the fibers (figure 7.12c). This can potentially serve as a point of stress concentration leading to premature crack initiation and consequent fracture. The presence of river marks (as seen in figure 7.12d) originating at the fiber-matrix interface supports the hypothesis that the crack initiated from the interface [89]–[91].

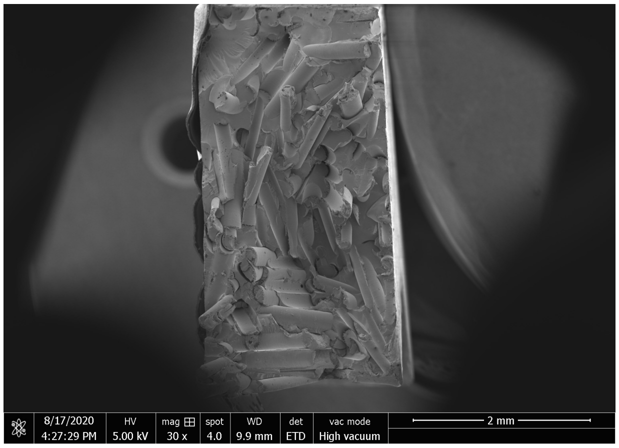

(a)

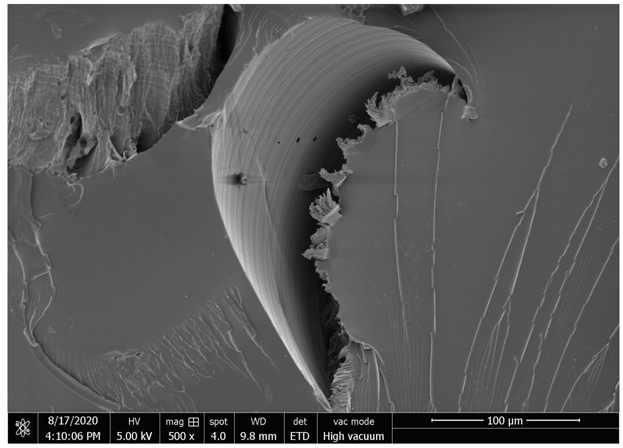

(b)

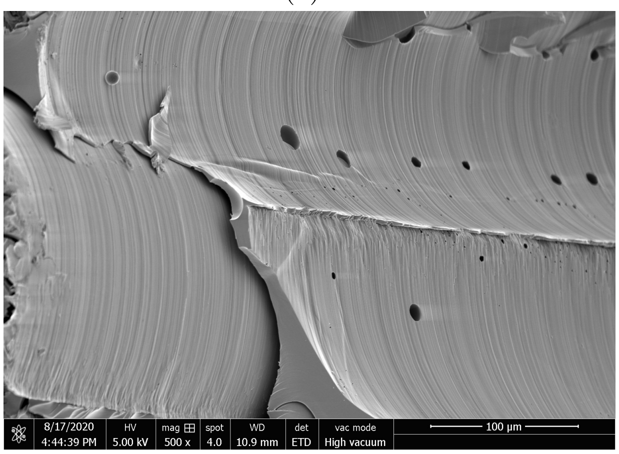

(c)

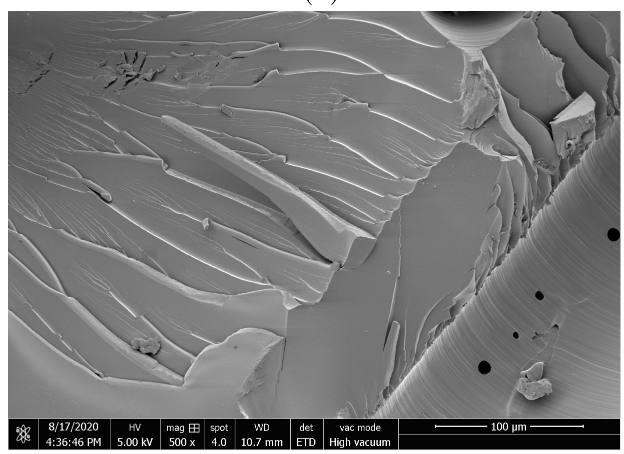

(d)

Figure 7.12. Fracture surface of a composite made with Al 6061 fibers showing (a) fiber debonding as the primary cause of fracture (b) holes left behind by pulled out fibers, showing a smooth surface at the boundary between matrix and fiber rake face, and a rough surface at the interface with the fiber back face (c) showing the air bubbles that were trapped between a fiber and epoxy (d) orientation of river marks suggest that the cracks initiated from the fiber-matrix interface.

Studies of fracture in the composites helped in the understanding of the viability of using metal fibers as a filler material for reinforcing polymers.

7.7 Summary

Modulation-assisted machining has already shown capabilities in improving the machinability of alloys by enabling efficient lubrication and reduced tool wear [92] and in improving chip evacuation in drilling applications [93], [94]. This study advises on the plausibility of using MAM as a particle production technique. It was found that the particle size distribution is narrow (within $50 - 100\mu m$). Particle sizes from $10\mu m$ to around $500\mu m$ can be produced in the lab-based setup. The lowest rotational speed that could produce discrete chips was 40 RPM. At speeds lower than that, minor instabilities in RPM caused the cutting to shift from discrete to continuous, thereby, producing a mixture of continuous and discrete chips. Optimization of process control to eliminate instantaneous variations in the rotational speed at low RPM ($<$ 40 RPM) can help achieve lower particle sizes.

The rate of particle production is low due to the cutting of one particle at a time. Furthermore, the production rate is a function of particle size. Incorporation of multiple cutting edges can be beneficial for improving the rates.

MAM can be a useful tool to produce metal fibers to reinforce polymers. Chopped fiber composites made of aluminum and titanium fibers produce a 30% and 100 % improvement in the modulus of epoxy. The primary fracture mode for the composites was found to fiber-pull out. Air bubbles present at the interface of the matrix and the fibers are suggested to be the initiator of cracks. Vacuum degassing of the liquid epoxy mixture before curing can help in reducing the probability of crack formation and improve the ductility of the composite. It will be interesting to measure the electrical conductivity of the composite and is a matter of further study.

8. SUMMARY

Modulation Assisted Machining has been used as a tool to study transient or non-steady deformation mechanisms that occur in manufacturing processes such as drilling and milling of materials. The optimum modulation condition for periodic detachment of the tool from the workpiece is achieved when the peak-to-peak amplitude, 2A $> s_o$ and $f_m/f_w = \frac{2n+1}{2}$. Discrete chips are produced in each modulation cycle, that are identical to each other and have the same composition as that of the workpiece. Therefore, MAM can be utilized as a deformation-based technique of producing metal particles of controlled morphology. The particle dimensions depend on the undeformed geometry of the material volume that is removed as an individual chip, which in turn can be predicted by a set of kinematic equations involving the process parameters, and the deformation during cutting. The thesis mainly studies the properties of short fibers made with MAM, as this morphology ensured plane strain deformation conditions and restricted the change in dimensions in only two directions. For these conditions, incorporation of the cutting ratio, r, (the ratio of deformed and undeformed chip dimensions, generally a material parameter) into the kinematic equations, takes into account the change in the dimensions due to deformation.

Experimentally measured lengths of MAM fibers (length is defined along the cutting direction) show a slight variation from the predicted length. This is a result of the assumption of a constant r for the entire range of modulation frequencies and optical measurement errors. Cutting ratio is a function of the amount of strain imparted during the deformation of cutting. In continuous cutting, since the process occurs under steady-state (constant rake angle, undeformed chip thickness), the strain imposed is uniform, making r a material-dependent parameter. In modulation-assisted machining, the sinusoidal nature of the tool path causes the effective rake angle to vary from a positive to a negative value. Therefore, the strain imposed is no longer constant, but, varies along the length of the cut, making the cutting ratio also a variable dependent on the position of the tool in the cutting cycle.

Mathematical simulation of the modulation function superimposed with an offset corresponding to the tool feed can model the tool paths, and the area overlapped by two consecutive paths can predict the 2-D undeformed chip shape. For ideal MAM conditions, the predicted fiber shape was uniform with a constant thickness while experimentally observed cross-sections of particles produced by MAM have a non-uniform thickness, as exhibited by a reduced deformed chip thickness at the start of particle formation followed by a region of constant thickness. At the beginning of the cut, deformation during cutting is similar to that in the case of indentation. Strain imposed under incipient conditions is lower than the steady-state which is characterized by a very small increase in thickness at the onset of deformation. After a critical length of cut, it transitions to a steady state indicated by the nearly constant chip thickness in the middle. Both these factors, the varying rake angle along the length of the cut, and the change in deformation mode impart a variable and inhomogeneous strain in a single MAM chip. This was shown previously, through a simulation of cutting strain in MAM with finite-element modeling. In this study, micro-indentation was performed on the chips along its length, which confirmed that the beginning of the chip (corresponding to initial deformation) has a lower hardness than its center. The varying hardness and thickness of a chip provided experimental validation of the theory of ”incipient” chip formation in periodic cutting systems such as MAM.

Many authors have reported a gradual increase in the cutting forces after the first moment of workpiece-tool engagement and the presence of a critical length of cut necessary to attain a steady value. The short distance of workpiece-tool engagement in each modulation cycle is often insufficient to reach this steady state, implying that the chips made by interrupted cutting techniques such as MAM are subjected to varying deformation modes for most of the cutting period. Since the length of cut (distance) depends on the modulation frequency, as frequency increases, the fibers are formed under increasingly incipient conditions. The plastic strain is reduced. The decreasing hardness of fibers with increasing modulation frequency observed is a direct consequence of the reduced strain. The hardness of the fibers made with a very low modulation frequency is also lower than those made with continuous cutting suggesting that imposing even a low-frequency modulation changes the overall deformation mode, and is manifested by decreased strain hardening, reduced chip hardness, and non-uniform thickening.

At the end of each cutting cycle, there are two possible mechanisms of fiber detachment with the workpiece. Firstly, cutting continues to the end of the tool locus where the tool disengages with the material. The other possibility is when the material shears before the cutting is completed. This results in a straight edge at the detachment end of the fiber cross-section. This has been shown via fractography on the width-thickness plane of the fibers. While some fibers show that cutting continued to the very end (characterized by the small thickness), others displayed a flat thick plane indicative of a shear fracture. In the event of fracture, little to no strain would be imposed on the chip volume toward the end of the cutting. This is observed as the slight drop in the local hardness measured by micro-indentation in the region between the chip center and the end.

MAM can be implemented to produce particles from alloys such as Ti-6-4 and Inconel 718 that are traditionally known to have poor machinability. Periodic disruption into the tool-workpiece contact allows better cutting fluid action and therefore, reduced cutting temperatures, tool wear and cutting forces. Systematic studies of chip shape and hardness showed that the change in dimensions due to deformation was lower and the cutting ratio was smaller for harder materials. Furthermore, the cutting ratio decreased with increasing modulation frequency (because of the decreasing shear strain). High strength alloys frequently displayed the presence of a flat edge toward the end of the cut suggesting that shear fracture commonly occurred in the chips before a cutting cycle was completed. The shear fracture end was also common for aluminum chips made at high frequencies.

In this study, f_w was set at 2 Hz, thus any odd number value of f_m produced the ideal modulation condition. The surface profile of the workpiece machined with modulation is periodic (consisting of a repeating group of peaks) and the nature of the periodicity depends on the phase difference between two consecutive tool paths or the nature of the modulation condition. Simulation of workpiece surface for f_m= 101 to 102 Hz showed that a different offset frequency produced a different periodicity. Experimentally observed profiles matched largely with the mathematical profile barring a few regions which showed a variation in the frequency and height of the surface asperities. This suggested that instantaneous variations in process parameters (mainly the workpiece rotational frequency) may be occurring in MAM that can affect the uncut geometry making the study of shape change due to deformation alone difficult in a system like MAM.

Linear orthogonal cutting was performed on a rectangular sample with machined grooves to simulate interrupted cutting with a pillar-like fixed uncut geometry. In-situ observation of the cutting process showed that the deformation in each pillar starts with the compression of the material ahead of the tool face followed by bending. However, due to the presence of a free surface or the lack of a constraint from the bulk material, the pillars fractured before the tool completed its course of travel across its length. The uncut volume of material that is removed as a chip in MAM is similar to the free-standing pillar in the linear machining experiments. Therefore, similar deformation modes of compression-bending-fracture are likely to be occurring in the chips exhibiting the flat edge at the end of the cut. Observation of interrupted 2-D machining of Ti-6-4 showed minimal bending as opposed to aluminum, consistent with the lack of curling in MAM chips made of Ti-6-4 in contrast with Al 6061. The strain field in a Ti-6-4 pillar was measured with PIV analysis which showed that the strain concentrated at the tool tip, resulting in the initiation of a crack. The remaining volume was largely strain-free. This explains the lower shear strain as exhibited by a lower hardness and shape change in the fibers produced in MAM at high frequencies and for high strength metals such Inconel 718, which almost always featured a flat fracture surface at the end of cutting, in the fiber cross-section.

MAM can be a valuable tool for particle manufacturing because of its lower size distribution and wide applicability. However, the production rate for a single cutting edge tool is significantly lower compared to conventional metal powder production processes, especially when producing smaller particles. The process can be particularly helpful in producing powders from materials such as titanium aluminide, which is hard to produce via atomization owing to its high affinity for oxygen and chemical reaction with the furnace crucibles [95]. MAM can act as a supplementary technique for producing special alloy powders. It can also be useful to produce metal fibers with applications such as fiber-reinforced polymers and conductive polymer composites.

9. FUTURE WORK

The observation of changing particle morphology with process parameters will help in predicting and controlling the particle shape in MAM. Measurement of shear strain for various modulation frequencies will aid in more accurate estimation of the cutting ratio and thereby, predict the particle dimensions better. Although this thesis explored a wide range of processing conditions, it will be worthwhile to study the identify the current system limitations and determine the limits of the particle sizes that can be produced through MAM. The condition which yielded the smallest particle length ($\sim 20m$) was 40 RPM and $f_m = 999.67$. For RPM lower than 40, the chips produced were connected and not discrete. Experiments may be designed to find out the system modifications required to eliminate this limitation (better lubrication conditions or using chip breakers), such that smaller particle sizes can be achieved. Use of large feeds and higher RPM can also be explored to assess the largest particle size that can be produced through the current set up.

TEM microstructures of the chips produced in continuous cutting showed prominent elongated grain structure (in the direction of material flow) representing the severe plastic deformation during cutting. However, the MAM chips was observed to contain mostly diffuse dislocation substructures which is a characteristic of the initial stages of grain refinement during plastic deformation. The absence of secondary shear zone was a mark of transient deformation mechanisms that prevail during the short period of cutting. Although this information is very important in distinguishing the deformation levels in the two processes (cutting with and without modulation), systematic studies of microstructural variation with the MAM process parameters have not been done so far. It will also be very interesting to observe the gradual transition in the microstructure, for transient state to that of the steady state. It will also be valuable to characterize the changing microstructure along the length of a fiber. Further analysis of cell misorientation, dislocation density and preferred orientation of the grains will also provide a quantitative description of the effect of transient deformation modes on the chip microstructure.

MAM fibers were shown to have two distinct types of edges. In some cases, a flat end was observed at the end of cutting (in the fiber cross-section) that was indicative of shear fracture before the completion of the cut, while in other cases, the edge was narrow suggesting that cutting continued till the very end of the tool path. The fracture was more prominent at higher frequencies and for high strength materials. For Al 6061, chip fracture (flat edge at the end of the cut) was also observed in the case of 101 Hz for certain batches of fibers while others predominantly narrowed down to a point. Systematic investigation of the process and material conditions leading to this fracture behaviour will be helpful in controlling the particle morphology in MAM.

Metal fibers can be used to reinforce a polymer and improve its electrical and thermal conductivity. Mechanical testing of composites made with epoxy, reinforced with Al 6061 fibers and Ti-6-4 fibers showed a 35 % and 100 % increase in rigidity respectively. The composite samples were prepared by free settling of fibers in the epoxy, which led to a volume fraction of 20 %. It will be interesting to vary the volume percentage of these metal fiber fillers through polymer extrusion-based sample preparation methods and measure the corresponding mechanical properties. It will also be valuable to measure the electrical conductivity of these metal fiber reinforced epoxy samples and explore the possible applications of MAM fibers for conductive polymer composites.

REFERENCES

[1] E. M. Trent and P. K. Wright, *Metal cutting*. Butterworth-Heinemann, 2000.

[2] M. C. Shaw and J. Cookson, *Metal cutting principles*. Oxford university press New York, 2005, vol. 2.

[3] L. De Chiffre, "Mechanics of metal cutting and cutting fluid action," *International Journal of Machine Tool Design and Research*, vol. 17, no. 4, pp. 225–234, 1977.

[4] V. Madhavan, S. Chandrasekar, and T. Farris, "Direct observations of the chip-tool interface in the low speed cutting of pure metals," *J. Trib.*, vol. 124, no. 3, pp. 617–626, 2002.

[5] E. Doyle, J. Horne, and D. Tabor, "Frictional interactions between chip and rake face in continuous chip formation," *Proceedings of the Royal Society of London. A. Mathematical and Physical Sciences*, vol. 366, no. 1725, pp. 173–183, 1979.

[6] J. Williams and D. Tabor, "The role of lubricants in machining," *Wear*, vol. 43, no. 3, pp. 275–292, 1977.

[7] Y. Zhang and J. Peklenik, "Chip curl, chip breaking and chip control of the difficult-to-cut materials," *CIRP Annals*, vol. 29, no. 1, pp. 79–83, 1980.

[8] S. Ghosh, P. V. Rao, *et al.*, "Application of sustainable techniques in metal cutting for enhanced machinability: A review," *Journal of Cleaner Production*, vol. 100, pp. 17–34, 2015.

[9] H. J. Findley, *Method and apparatus for cutting material*, US Patent 3,174,404, Mar. 1965.

[10] D. Brehl and T. Dow, "Review of vibration-assisted machining," *Precision engineering*, vol. 32, no. 3, pp. 153–172, 2008.

[11] B. Sencer and M. Maulimov, "A new turning system assisted by chip-pulling," *Journal of Manufacturing Processes*, vol. 34, pp. 734–739, 2018.

[12] N. K. Maroju, K. P. Vamsi, and J. Xiaoliang, "Investigations on feasibility of low-frequency vibration-assisted turning," *The International Journal of Advanced Manufacturing Technology*, vol. 91, no. 9, pp. 3775–3788, 2017.

[13] T. Sugihara and T. Enomoto, "Ultra-low-frequency vibration assisted machining of ti-6al-4v alloy," *International Journal of Automation Technology*, vol. 10, no. 4, pp. 647–653, 2016.

[14] M. Merchant and N. Zlatin, “Nomographs for analysis of metal-cutting processes,” *Mech. Eng*, vol. 67, no. 11, pp. 737–742, 1945.

[15] H. Yeung, N. K. Sundaram, J. B. Mann, W. D. Compton, and S. Chandrasekar, “Energy dissipation in modulation assisted machining,” *International Journal of Machine Tools and Manufacture*, vol. 74, pp. 41–49, 2013.

[16] H. Yeung, Y. Guo, J. B. Mann, W. Dale Compton, and S. Chandrasekar, “Effect of low-frequency modulation on deformation and material flow in cutting of metals,” *Journal of Tribology*, vol. 138, no. 1, 2016.

[17] P. Rosa, O. Kolednik, P. Martins, and A. Atkins, “The transient beginning to machining and the transition to steady-state cutting,” *International Journal of Machine Tools and Manufacture*, vol. 47, no. 12-13, pp. 1904–1915, 2007.

[18] W.-S. Yun, J. H. Ko, H. U. Lee, D.-W. Cho, and K. F. Ehmann, “Development of a virtual machining system, part 3: Cutting process simulation in transient cuts,” *International Journal of Machine Tools and Manufacture*, vol. 42, no. 15, pp. 1617–1626, 2002.

[19] J. Clayton, “Optimising metal powders for additive manufacturing,” *Metal Powder Report*, vol. 69, no. 5, pp. 14–17, 2014.

[20] J. A. Slotwinski, E. J. Garboczi, P. E. Stutzman, C. F. Ferraris, S. S. Watson, and M. A. Peltz, “Characterization of metal powders used for additive manufacturing,” *Journal of research of the National Institute of Standards and Technology*, vol. 119, p. 460, 2014.

[21] A. Ünal, “Effect of processing variables on particle size in gas atomization of rapidly solidified aluminium powders,” *Materials Science and Technology*, vol. 3, no. 12, pp. 1029–1039, 1987.

[22] M. R. Shankar, S. Chandrasekar, W. D. Compton, and A. H. King, “Characteristics of aluminum 6061-t6 deformed to large plastic strains by machining,” *Materials Science and Engineering: A*, vol. 410, pp. 364–368, 2005.

[23] G. Townend, “Direction of maximum crystal elongation during metal cutting,” *Journal of Applied Physics*, vol. 18, no. 5, pp. 489–490, 1947.

[24] H. Ernst and M. Merchant, “Eugene: Chip fomation, friotion, and high qu, alit; y machined surfaces. surface treatment at metals,” *Am. Soc. Metals (Cleveland)*, pp. 299–335, 1941.

[25] J. Mann, C. Saldana, W. Compton, T. Farris, K. Trumble, and S. Chandrasekar, "Effect of controlled modulation on chip formation and interface tribology in machining," in *International Manufacturing Science and Engineering Conference*, vol. 43611, 2009, pp. 187–191.

[26] W. Moscoso, E. Olgun, W. D. Compton, and S. Chandrasekar, "Effect of low-frequency modulation on lubrication of chip-tool interface in machining," *J. Trib.*, vol. 127, no. 1, pp. 238–244, 2005.

[27] J. Mann, C. Saldana, S. Chandrasekar, W. Compton, and K. Trumble, "Metal particulate production by modulation-assisted machining," *Scripta Materialia*, vol. 57, no. 10, pp. 909–912, 2007.

[28] J. Mann, Y. Guo, C. Saldana, W. Compton, and S. Chandrasekar, "Enhancing material removal processes using modulation-assisted machining," *Tribology International*, vol. 44, no. 10, pp. 1225–1235, 2011.

[29] B. Eren and B. Sencer, "Mechanistic cutting force model and specific cutting energy prediction for modulation assisted machining," *Procedia Manufacturing*, vol. 48, pp. 474–484, 2020.

[30] K. J. Weinmann and B. Von Turkovich, "Mechanics of tool-workpiece engagement and incipient deformation in machining of 70/30 brass," 1971.

[31] Y. Li and S. Y. Liang, "Cutting force analysis in transient state milling processes," *The International Journal of Advanced Manufacturing Technology*, vol. 15, no. 11, pp. 785–790, 1999.

[32] J. B. Mann, S. Chandrasekar, and W. D. Compton, *Tool holder assembly and method for modulation-assisted machining*, US Patent 7,587,965, Sep. 2009.

[33] J. Hirsch, B. Skrotzki, and G. Gottstein, *Aluminium alloys: the physical and mechanical properties*. John Wiley & Sons, 2008, vol. 1.

[34] I. Polmear, D. StJohn, J.-F. Nie, and M. Qian, *Light alloys: metallurgy of the light metals*. Butterworth-Heinemann, 2017.

[35] N. Maruyama, R. Uemori, N. Hashimoto, M. Saga, and M. Kikuchi, "Effect of silicon addition on the composition and structure of fine-scale precipitates in al-mg-si alloys," *Scripta materialia*, vol. 36, no. 1, 1997.

[36] R. Escalera-Lozan, M. Pech-Canul, M. Pech-Canul, M. Montoya-Dávila, and A. Uribe-Salas, "The role of mg2si in the corrosion behavior of al-si-mg alloys for pressureless infiltration," *The Open Corrosion Journal*, vol. 3, no. 1, 2010.

[37] *Aluminium / aluminum 6061 alloy (uns a96061)*, (Accessed on 04/07/2021), Sep. 27, 2012. [Online]. Available: https://www.azom.com/article.aspx?ArticleID=6636.

[38] F. Armao, *Aluminum workshop: Achieving t6 designation for 6061*, (Accessed on 04/07/2021), Mar. 14, 2011. [Online]. Available: https://www.thefabricator.com/thewelder/article/aluminumwelding/achieving-t6-designation-for-6061.

[39] *Heat treating aluminum 6061 - quenching and aging aluminum 6061*, (Accessed on 04/07/2021), May 16, 2018. [Online]. Available: https://www.jmpforming.com/blog/aluminum-heat-treating/quenching-and-aging-aluminum-6061.htm.

[40] M. J. Couper, "Selecting the optimum mg and si content for 6xxx series extrusion alloys," in *Proceedings of the 12th International Conference on Aluminium Alloys*, 2010, pp. 5–6.

[41] M. Rahman, W. Seah, and T. Teo, "The machinability of inconel 718," *Journal of Materials Processing Technology*, vol. 63, no. 1-3, pp. 199–204, 1997.

[42] D. Dudzinski, A. Devillez, A. Moufki, D. Larrouquere, V. Zerrouki, and J. Vigneau, "A review of developments towards dry and high speed machining of inconel 718 alloy," *International journal of machine tools and manufacture*, vol. 44, no. 4, pp. 439–456, 2004.

[43] A. Devillez, G. Le Coz, S. Dominiak, and D. Dudzinski, "Dry machining of inconel 718, workpiece surface integrity," *Journal of Materials Processing Technology*, vol. 211, no. 10, pp. 1590–1598, 2011.

[44] A. Del Prete, L. Filice, and D. Umbrello, "Numerical simulation of machining nickel-based alloys," *Procedia Cirp*, vol. 8, pp. 540–545, 2013.

[45] H. Yeung, K. Viswanathan, A. Udupa, A. Mahato, and S. Chandrasekar, "Sinuous flow in cutting of metals," *Physical Review Applied*, vol. 8, no. 5, p. 054 044, 2017.

[46] M. E. Merchant, "Mechanics of the metal cutting process. i. orthogonal cutting and a type 2 chip," *Journal of applied physics*, vol. 16, no. 5, pp. 267–275, 1945.

[47] M. R. Shankar, S. Chandrasekar, A. H. King, and W. D. Compton, "Microstructure and stability of nanocrystalline aluminum 6061 created by large strain machining," *Acta Materialia*, vol. 53, no. 18, pp. 4781–4793, 2005.

[48] V. Mazet, *Background correction - file exchange - matlab central*, (Accessed on 01/07/2021), Feb. 20, 2013. [Online]. Available: https://www.mathworks.com/matlabcentral/fileexchange/27429-background-correction.

[49] J. T. Black, "Shear front-lamella structure in large strain plastic deformation processes," 1972.

[50] B. Von Turkovich and J. T. Black, "Micro-machining of copper and aluminum crystals," 1970.

[51] B. Von Turkovich, "Shear stress in metal cutting," 1970.

[52] J. T. Black, "On the fundamental mechanism of large strain plastic deformation: Electron microscopy of metal cutting chips," 1971.

[53] K. Nakayama, "On the formation of" saw-toothed chip" in metal cutting," *J Japan Soc Prec Eng*, vol. 43, pp. 117–122, 1977.

[54] K. Herrmann *et al.*, *Hardness testing: principles and applications*. ASM international, 2011.

[55] L. Adrian, R. J. Adrian, and J. Westerweel, *Particle image velocimetry*, 30. Cambridge university press, 2011.

[56] S. Gogineni, L. Goss, D. Pestian, and R. Rivir, "Two-color digital piv employing a single ccd camera," *Experiments in Fluids*, vol. 25, no. 4, pp. 320–328, 1998.

[57] S. Lee, "Direct measurements of severe plastic deformation in machining and equal channel angular pressing," 2006.

[58] S. Lee, J. Hwang, M. R. Shankar, S. Chandrasekar, and W. D. Compton, "Large strain deformation field in machining," *Metallurgical and Materials Transactions A*, vol. 37, no. 5, pp. 1633–1643, 2006.

[59] O. Molnárová, P. Málek, F. Lukáč, and T. Chráska, "Spark plasma sintering of a gas atomized al7075 alloy: Microstructure and properties," *Materials*, vol. 9, no. 12, p. 1004, 2016.

[60] I. E. Anderson, E. M. White, and R. Dehoff, "Feedstock powder processing research needs for additive manufacturing development," *Current Opinion in Solid State and Materials Science*, vol. 22, no. 1, pp. 8–15, 2018.

[61] N. Etxebarria, G. Arana, R. Antolin, G. Borge, T. Posada, and J. Raposo, "Selenium in electrolytic manganese as a reference material for the quality control of aluminium melts," *Accreditation and quality assurance*, vol. 12, no. 11, pp. 575–580, 2007.

[62] L. Avramović, M. Bugarin, D. Milanović, V. Conić, M. M. Pavlović, M. Vuković, and N. D. Nikolić, "The particle size distribution (psd) as criteria for comparison of silver powders obtained by different methods of synthesis and by conditions of electrolysis," *Journal of Mining and Metallurgy B: Metallurgy*, vol. 54, no. 3, pp. 291–300, 2018.

[63] J. A. Slotwinski and E. J. Garboczi, "Metrology needs for metal additive manufacturing powders," *Jom*, vol. 67, no. 3, pp. 538–543, 2015.

[64] S. K. Bhattacharya, *Metal filled polymers*. CRC Press, 1986, vol. 11.

[65] A. K. McBride, S. L. Turek, A. E. Zaghi, and K. A. Burke, "Mechanical behavior of hybrid glass/steel fiber reinforced epoxy composites," *Polymers*, vol. 9, no. 4, p. 151, 2017.

[66] D. M. Bigg, "Mechanical, thermal, and electrical properties of metal fiber-filled polymer composites," *Polymer Engineering & Science*, vol. 19, no. 16, pp. 1188–1192, 1979.

[67] D. Bigg, "Mechanical properties of particulate filled polymers," *Polymer Composites*, vol. 8, no. 2, pp. 115–122, 1987.

[68] V. Srivastava and A. Verma, "Mechanical behaviour of copper and aluminium particles reinforced epoxy resin composites," *American Journal of Materials Science*, vol. 5, no. 4, pp. 84–89, 2015.

[69] V. E. Gul, *Structure and properties of conducting polymer composites*. VSP, 1996, vol. 8.

[70] J. Delmonte, *Metal/polymer composites*. Springer, 2013.

[71] Q. Xue, "The influence of particle shape and size on electric conductivity of metal–polymer composites," *European Polymer Journal*, vol. 40, no. 2, pp. 323–327, 2004.

[72] M. Megahed, A. Fathy, D. Morsy, and F. Shehata, "Mechanical performance of glass/epoxy composites enhanced by micro-and nanosized aluminum particles," *Journal of Industrial Textiles*, p. 1 528 083 719 874 479, 2019.

[73] P. Sarkar, N. Modak, and P. Sahoo, "Effect of aluminum filler on friction and wear characteristics of glass epoxy composites," *Silicon*, vol. 10, no. 3, pp. 715–723, 2018.

[74] Z. Wang, H. A. Colorad, Z.-H. Guo, H. Kim, C.-L. Park, H. T. Hahn, S.-G. Lee, K.-H. Lee, and Y.-Q. Shang, "Effective functionalization of carbon nanotubes for bisphenol f epoxy matrix composites," *Materials Research*, vol. 15, no. 4, pp. 510–516, 2012.

[75] A. Allaoui, S. Bai, H.-M. Cheng, and J. Bai, “Mechanical and electrical properties of a mwnt/epoxy composite,” *Composites science and technology*, vol. 62, no. 15, pp. 1993–1998, 2002.

[76] N. Domun, H. Hadavinia, T. Zhang, T. Sainsbury, G. Liaghat, and S. Vahid, “Improving the fracture toughness and the strength of epoxy using nanomaterials–a review of the current status,” *Nanoscale*, vol. 7, no. 23, pp. 10 294–10 329, 2015.

[77] W. Cantwell, A. Roulin-Moloney, and T. Kaiser, “Fractography of unfilled and particulate-filled epoxy resins,” *Journal of materials science*, vol. 23, no. 5, pp. 1615–1631, 1988.

[78] B. Rosen, *Fracture processes in polymeric solids: phenomena and theory*. Interscience Publishers, 1964.

[79] B. Cherry and K. Thomson, “The fracture of highly crosslinked polymers,” *Journal of Materials Science*, vol. 16, no. 7, pp. 1913–1924, 1981.

[80] T. Shioya, Y. Koga, K. Fujimoto, and R. Ishida, “Micro-mechanism of dynamic crack propagation in brittle materials,” *Le Journal de Physique Colloques*, vol. 49, no. C3, pp. C3–253, 1988.

[81] L. Wenbo and Y. Tingqing, “Computer simulation of conic-shaped patterns on fracture surfaces of polymers,” *Journal of applied polymer science*, vol. 89, no. 6, pp. 1722–1725, 2003.

[82] K. O. Reddy, C. U. Maheswari, K. R. Reddy, M. Shukla, E. Muzenda, and A. V. Rajulu, “Effect of chemical treatment and fiber loading on mechanical properties of borassus (toddy palm) fiber/epoxy composites,” *International Journal of Polymer Analysis and Characterization*, vol. 20, no. 7, pp. 612–626, 2015.

[83] S. Sethi and B. C. Ray, “An assessment of mechanical behavior and fractography study of glass/epoxy composites at different temperatures and loading speeds,” *Materials & Design*, vol. 64, pp. 160–165, 2014.

[84] G. Chen, J. Zhang, G. Liu, P. Chen, and M. Guo, “Controlling the crack propagation path of the veil interleaved composite by fusion-bonded dots,” *Polymers*, vol. 11, no. 8, p. 1260, 2019.

[85] K. G. Dassios, “A review of the pull-out mechanism in the fracture of brittle-matrix fibre-reinforced composites,” *Advanced Composites Letters*, vol. 16, no. 1, 2007.

[86] Y. Yao and S. Chen, “The effects of fiber’s surface roughness on the mechanical properties of fiber-reinforced polymer composites,” *Journal of composite materials*, vol. 47, no. 23, pp. 2909–2923, 2013.

[87] A. Valadez-Gonzalez, J. Cervantes-Uc, R. Olayo, and P. Herrera-Franco, “Effect of fiber surface treatment on the fiber–matrix bond strength of natural fiber reinforced composites,” *Composites Part B: Engineering*, vol. 30, no. 3, pp. 309–320, 1999.

[88] W. Song, A. Gu, G. Liang, and L. Yuan, “Effect of the surface roughness on interfacial properties of carbon fibers reinforced epoxy resin composites,” *Applied surface science*, vol. 257, no. 9, pp. 4069–4074, 2011.

[89] Y. Zhu, J. Valdez, I. Beyerlein, S. Zhou, C. Liu, M. Stout, D. Butt, and T. Lowe, “Mechanical properties of bone-shaped-short-fiber reinforced composites,” *Acta materialia*, vol. 47, no. 6, pp. 1767–1781, 1999.

[90] O. Okoli and G. Smith, “Failure modes of fibre reinforced composites: The effects of strain rate and fibre content,” *Journal of Materials Science*, vol. 33, no. 22, pp. 5415–5422, 1998.

[91] G. A. Pantazopoulos, “A short review on fracture mechanisms of mechanical components operated under industrial process conditions: Fractographic analysis and selected prevention strategies,” *Metals*, vol. 9, no. 2, p. 148, 2019.

[92] Y. Guo, J. Mann, H. Yeung, and S. Chandrasekar, “Enhancing tool life in high-speed machining of compacted graphite iron (cgi) using controlled modulation,” *Tribology Letters*, vol. 47, no. 1, pp. 103–111, 2012.

[93] Y. Guo, S. E. Lee, and J. B. Mann, “Piezo-actuated modulation-assisted drilling system with integrated force sensing,” *Journal of Manufacturing Science and Engineering*, vol. 139, no. 1, 2017.

[94] Y. Guo and J. B. Mann, “Control of chip formation and improved chip ejection in drilling with modulation-assisted machining,” *Journal of Manufacturing Science and Engineering*, vol. 142, no. 7, 2020.

[95] R. Gerling, H. Clemens, and F. Schimansky, “Powder metallurgical processing of intermetallic gamma titanium aluminides,” *Advanced Engineering Materials*, vol. 6, no. 1-2, pp. 23–38, 2004.

VITA

Indrani Biswas was born on September 13th 1991 in Sodepur, a suburb of Kolkata city in West Bengal, India. She completed high school from St. Xaviers Institutation, Panihati in 2010. After high school graduation, she attended Jadavpur University, Kolkata and received an undergraduate degree in metallurgical engineering in 2014. She was awarded with a gold medal for receiving the top grade in her class. She continued her education and pursued a masters degree in Materials Engineering from Indian Institute of Science, Bangalore. She graduated from IISc in 2016 before joining Purdue University, West Lafayette, Indiana for doctorate studies in the school of Materials Engineering. During PhD, she was a member of TMS-The Minerals, Metals and Materials Society and ASM international-The Materials Information Society. She had participated and presented talks in four conferences and has authored a conference proceeding.